VALIDATION OF MODELING METHODOLOGY AND INVESTIGATION OF MASS ADDITION EFFECTS ON EVOLUTION OF TRACE SPECIES IN POST-COMBUSTOR FLOW PATH

by

Chi Kin Yam

MASSACHUSETTS INSTITUTE
OF TECHNOLOGY
SEP 1 0 2003
LIBRARIES

B.S.E. Aerospace Engineering
University of Michigan, Ann Arbor, 2001

Submitted to the Department of Aeronautics and Astronautics
in partial fulfillment of the requirements for the degree of

Master of Science in Aeronautics and Astronautics

at the

Massachusetts Institute of Technology

June 2003

© 2003 Massachusetts Institute of Technology. All rights reserved.

Author: ____________________
Chi Kin Yam
Department of Aeronautics and Astronautics
May 23, 2003

Certified by: ____________________
Professor Ian A. Waitz
Professor and Deputy Head
Department of Aeronautics and Astronautics
Thesis Supervisor

Accepted by: ____________________
Professor Edward M. Greitzer
H. N. Slater Professor of Aeronautics and Astronautics
Chair, Committee on Graduate Students

AERO

VALIDATION OF MODELING METHODOLOGY AND INVESTIGATION OF MASS ADDITION EFFECTS ON EVOLUTION OF TRACE SPECIES IN POST-COMBUSTOR FLOW PATH

by

CHI KIN YAM

Submitted to the Department of Aeronautics and Astronautics
on May 23, 2003 in Partial Fulfillment of the
Requirement for the Degree of Master of Science in
Aeronautics and Astronautics

Abstract

The impact of aircraft emissions on the atmosphere has been a growing concern over the last decade. Due to direct deposition of emissions at altitude, aircraft are currently expected to have about double the climate change impact of terrestrial sources per unit of fuel burned. With the continual increase in air traffic, a more thorough understanding of the evolution of trace chemical species (emissions) inside gas turbine engines is important for better estimating these climate effects and the potential role for technology in mitigating them. Due to difficulties conducting detailed tests and measurements inside engines, development of effective computer modeling tools is critical.

The existing modeling methodology used to investigate the evolution of trace species in the post-combustor flow path of gas turbine engines has been improved and validated with engine measurements made by NASA/QinetiQ. A circumferentially varying inlet profile is now included in the model. Circumferentially non-uniform and unsteady wakes are also used as input to rotor calculations. Assessment with experimental data shows that the model is able to capture the species changes within an order of magnitude. Most discrepancies come from insufficient combustor exit data which is necessary to specify a complete and accurate initial condition for the modeling calculation.

Mass addition capability was implemented to model transpiration cooling and was used to study the effect of cooling air injection on species evolution. Addition of cooling air produces both pure dilution effects and effects associated with modified chemical reactions. Investigations with a square duct geometry at a free-stream temperature of ~1150 K showed that the effects of dilution dominate other chemical changes due to film cooling. Chemical effects may be come more important at a higher temperature (>1800 K). Compared to cooling with no mass injection (e.g. a cold wall), less production of the important species, e.g. SO_3, HONO, is expected.

Thesis Supervisor: Professor Ian A. Waitz

Title: Professor and Deputy Department Head of Aeronautics and Astronautics

Acknowledgements

I would like to take this opportunity to thank the following people for contributing both directly and indirectly to the completion of this thesis, and making this research experience an enjoyable one. I would first thank my thesis advisor Prof. Ian Waitz for his leadership and guidance over this research project. His timely insights and encouragements keep my research from stalling. Thanks to Stephen Lukachko for his thorough knowledge and understanding to the modeling methodology and atmospheric effects of aircraft emissions. I would also like to thank Dr. Richard Miake-Lye of Aerodyne Research, Inc. for his expertise and suggestions throughout the course of the project.

Thanks to all my friends, regardless of location, for all the support and laughter. Special thanks to Vai-Man and CJ for all the great times we have together here.

Finally, I would like to thank my parents, for letting me walk my own path, for letting me not stay home with you guys, and for the endless support, love, and care.

The *Validation of Modeling Methodology and Investigation of Mass Addition Effects on Evolution of Trace Species in Post-Combustor Flow Path* work was supported by NASA Glen Research Center under contract NAS3-01153 and was a joint project between MIT Gas Turbine Lab and Aerodyne Research, Inc.

Table of Contents

ACKNOWLEDGEMENTS 5

TABLE OF CONTENTS 7

LIST OF FIGURES 9

LIST OF TABLES 13

I. INTRODUCTION 15

1.1. Chemical Composition of Aircraft Engine Emissions 15

1.2. Atmospheric Effects 17

1.3. Modeling of Engine Emissions 18

II. CURRENT MODELING METHODOLOGY 21

2.1. Modeling Tools Available 21

2.2. Choice of Tool to Use 22

2.2.1. Time Scale Analysis 23
2.2.2. Choice of Tools 25

2.3. Calculation Across HPT1 25

2.3.1. HPT1 Inlet Condition 27
2.3.2. Non-uniform Inlet Condition 28
2.3.3. NGV Calculation 31
2.3.4. Rotor Calculation 32

2.4. Calculation from HPT1 Exit to Nozzle Exit 32

III. MODELING ASSESSMENT WITH NASA/QINETIQ ENGINE TEST 35

3.1. Measurement Program 35

3.1.1. Combustor Test Program 35
3.1.2. Engine Test Program 36

3.2. Modeling of the NASA/QinetiQ Test Engine 37

3.2.1. Initial Conditions 38
I. HPT Inlet Temperature Profile 38
II. HPT1 Inlet Equivalence Ratio Profile 39

III. Trace Species Concentrations Profile 39
3.2.2. Run Matrix 42
3.2.3. Modeling Results 43
I. Temperature and Pressure 44
II. Sulfur Species – SO_3, H_2SO_4 46
III. Nitrogen Species – NO_2, HONO 50
IV. Carbon Monoxide (CO) 54
V. Assessment Summary 55

IV. INCORPORATION OF MASS ADDITION CAPABILITY INTO CNEWT 59

4.1. Mass Addition Methods 59

4.2. Boundary Conditions on Solid Surfaces in CNEWT 62

4.3. Effects of Wall Function on Surface Boundary Condition 65

4.4. Creation of Transpiration Surface Boundary Condition 67

4.5. Summary of Code Modification 71

V. MASS ADDITION ASSESSMENT WITH SQUARE DUCT GEOMETRY 73

5.1. Square Duct Geometry 73

5.1.1. Loss of Mass Flow 75
5.1.2. Non-uniform Distribution of the Flow 76
5.1.3. Flow Property Oscillations Near the End of the Duct 77

5.1. Investigation of Mass Addition Effect on Evolution of Trace Species 80

5.2.1. Static Temperature 82
5.2.2. Static Pressure 84
5.2.3. Oxygen (O_2) 86
5.2.4. Nitrogen (N_2) 88
5.2.5. Nitrogen Dioxide (NO_2) 89
5.2.6. Nitrous Acid (HONO) 91
5.2.7. Sulfur Trioxide (SO_3) 93
5.2.8. Sulfuric Acid (H_2SO_4) 94
5.2.9. Case Comparisons and Summary 96

VI. SUMMARY AND FUTURE WORK 103

APPENDIX A – ADDITIONAL PLOTS WITH NASA/QINETIQ VALIDATION 107

APPENDIX B – EFFECTS OF WALL FUNCTION ON TRANSPIRATION SURFACE 117

REFERENCES 119

List of Figures

Figure 1.1.1. Schematic of ideal combustion products (top), and all existing combustion products, showing scale of each [1] 16

Figure 2.2.1. Severity parameter plot for SO_3 at combustor exit condition (from Lukachko) 24
Figure 2.3.1. Grids for the NGV (left) and rotor (right) for CFD calculation 26
Figure 2.3.2. QinetiQ TRACE engine showing instrumentation points [8] 27
Figure 2.3.3. QinetiQ TRACE engine combustion system [8] 29
Figure 2.3.4. Temperature distribution (left), and NO_x distribution (right), looking upstream of combustor exit [9] 30
Figure 2.3.5. Static temperature profiles across HPT1, with NGV and rotor calculations 31
Figure 2.4.1. Points along the rotor exit temperature profile chosen for 1-D calculations 33

Figure 3.2.1. Temperature (K) distribution at combustor exit [8], [12] 38
Figure 3.2.2. NO_2 results across NGV with incorrect inlet specification 40
Figure 3.2.3. Equilibrium and averaged measured levels of NO/NO_y at NGV inlet 41
Figure 3.2.4. Static temperature profile for high sulfur run 44
Figure 3.2.5. Static pressure profile for high sulfur run 45
Figure 3.2.6. Mean temperature, pressure, and velocity profiles from second stage of HPT to nozzle exit 46
Figure 3.2.7. SO_3 profile for high sulfur run 48
Figure 3.2.8. H_2SO_4 profile for high sulfur run 48
Figure 3.2.9. NO_2 profile for high sulfur run 51
Figure 3.2.10. HONO profile for high sulfur run 53
Figure 3.2.11. CO profile for high sulfur run 55
Figure 3.2.12. Comparison between results of simulations (no air dilution) and experiments 56

Figure 4.1.1. Illustration of cooling schemes in a typical turbine stage [17] 60
Figure 4.1.2. Sketch of mass addition through cooling holes and slots on a blade surface (left), side view of mass injection on a flat surface (right) 61
Figure 4.1.3. Sketch of mass addition through transpiration on a blade surface (left), side view of transpiration cooling on a flat surface (right) 62

Figure 4.1.4. Regions of a turbulent boundary layer [18] 64
Figure 4.1.5. Configuration of the injection 68

Figure 5.1.1. Duct geometry 74
Figure 5.1.2. Grid 94b (left), Grid 95 (right) 74
Figure 5.1.3. Code development and testing stages 75
Figure 5.1.4. Mass flow along axial locations of the duct 76
Figure 5.1.5. Radial velocity (shown in color) along with streamlines of the duct (left), velocity vectors at axial location x = 0.49 m (right) 77
Figure 5.1.6. Velocity vectors with tangential velocity (color) (left), the grid at that location (right) 77
Figure 5.1.7. Temperature (left), and pressure (right) oscillations observe in the duct 78
Figure 5.1.8. Temperature plot with Grid 95 along with streamlines coming out from injection surface (left), temperature plot with Grid 94b (right) 79
Figure 5.2.1. Axial locations for the duct profile 82
Figure 5.2.2. Temperature distribution for Case 1 and Case 2 82
Figure 5.2.3. Temperature distribution for Case 3 and Case 4 83
Figure 5.2.4. Pressure distribution for Case 1 and Case 2 85
Figure 5.2.5. Pressure distribution for Case 3 and Case 4 85
Figure 5.2.6. Axial velocity profiles comparing no-slip case (left) and wall function case (right) 86
Figure 5.2.7. O_2 distribution for Case 1 and Case 2 87
Figure 5.2.8. O_2 distribution for Case 3 and Case 4 87
Figure 5.2.9. N_2 distribution for Case 1 and Case 2 88
Figure 5.2.10. N_2 distribution for Case 3 and Case 4 88
Figure 5.2.11. NO_2 distribution for Case 1 and Case 2 90
Figure 5.2.12. NO_2 distribution for Case 3 and Case 4 90
Figure 5.2.13. HONO distribution for Case 1 and Case 2 92
Figure 5.2.14. HONO distribution for Case 3 and Case 4 92
Figure 5.2.15. SO_3 distribution for Case 1 and Case 2 93
Figure 5.2.16. SO_3 distribution for Case 3 and Case 4 94
Figure 5.2.17. H_2SO_4 distribution for Case 1 and Case 2 95
Figure 5.2.18. H_2SO_4 distribution for Case 3 and Case 4 95
Figure 5.2.19. Temperature changes between inlet and exit of the duct 97
Figure 5.2.20. Pressure changes between inlet and exit of the duct 97

Figure 5.2.21. Oxygen and Nitrogen changes between inlet and exit of the duct 98
Figure 5.2.22. NO_2 changes between inlet and exit of the duct 99
Figure 5.2.23. SO_3 and HONO changes between inlet and exit of the duct 100
Figure 5.2.24. H_2SO_4 changes between inlet and exit of the duct 100

Figure 6.1.1. Calculation on NGV with original grid density using the modified code without injection, grid shown (left), static temperature with streamlines (right) 104
Figure 6.1.2. Calculation on NGV with increased grid density using the modified code without injection, grid shown (left), grid enlarged (center), static temperature with streamlines (right) 105

Figure A.1. Comparisons between results of simulations and experiments, no air dilution (top), with air dilution (bottom) 107
Figure A.2. Static temperature profiles for high sulfur (left) and low sulfur (right) runs 108
Figure A.3. Static pressure profiles for high sulfur (left) and low sulfur (right) runs 109
Figure A.4. Average 1-D temperature, pressure, and velocity profiles through second stage HPT, LPT, and exhaust nozzle, low Sulfur case (top), high sulfur case (bottom) 110
Figure A.5. SO_3 profiles for high sulfur (left) and low sulfur (right) runs 111
Figure A.6. NO_2 profiles for high sulfur (left) and low sulfur (right) runs 112
Figure A.7. HONO profiles for high sulfur (left) and low sulfur (right) runs 113
Figure A.8. CO profiles for high sulfur (left) and low sulfur (right) runs 114

Figure B.1. Various situations in resolving the boundary layer 118

List of Tables

Table 2.3.1. Input information required to generate combustor exit condition 28

Table 3.1.1. Two power conditions for combustor test 36
Table 3.1.2. Engine test run conditions 37
Table 3.2.1. Summary of run conditions 43
Table 3.2.2. SO_3 and H_2SO_4 evolution through the post-combustor flow path 49
Table 3.2.3. NO_2 and HONO evolution through the post-combustor flow path 52
Table 3.2.4. CO evolution through the post-combustor flow path 54

Table 5.1.1. Grid specifications 73
Table 5.2.1. Test matrix for mass addition investigation on evolution of trace species 80
Table 5.2.2. Changes of the species between inlet and exit of the duct 96

Table A.1. Complete results obtained for NASA/QinetiQ simulations 115

I. Introduction

Increased effort is being put into investigating aircraft emissions due to their unique and growing impact on the environment. Unlike ground-based emissions, pollutants from aircraft engines are emitted directly into upper atmosphere. For subsonic flights, emissions occur in the upper troposphere and lower stratosphere; while for supersonic flights, the altitude of deposition may extend well into the stratosphere. Because of different background concentrations of various species at altitude, as well as different physical and chemical effects, aircraft emissions can have a more significant impact on the atmosphere than those from ground-based sources.

According to the Intergovernmental Panel on Climate Change (IPCC) report [1], aircraft emissions contribute ~3.5% (1992) of total radiative forcing by all anthropogenic activities. Radiative forcing represents a change in average net radiation (in Wm^{-2}) at the top of the troposphere resulting from a change in either solar or infrared radiation due to a change in atmospheric greenhouse gases concentrations; a perturbation in the balance between incoming solar radiation and out-going infrared radiation [1]. A net positive radiative forcing will lead to global warming, and a net negative radiative forcing will lead to global cooling. With expectations for continued increase in air traffic, if the emissions rates are kept at the current level, the radiative forcing will continue to increase. The recent Royal Commission on Environmental Pollution (RCEP) report [19] suggests that the climate impact of aircraft may grow up to 6-10% of that of all anthropogenic activities by 2050. Thus there is a need to investigate the amount and composition of species emitted from aircraft engines.

1.1. Chemical Composition of Aircraft Engine Emissions

Although the combustion processes in gas turbine engines are highly efficient (above 99%), some unwanted products of combustion are still formed. Further, even the primary products of combustion can have a negative effect on the environment. For complete combustion of a hydrocarbon fuel with air, the combustion products are carbon dioxide (CO_2), nitrogen (N_2) and water vapor (H_2O). With incomplete combustion, the combustion products represent a more complex mixture with the presence of carbon species: C(s), CO, CO_2, nitrogen species due to involvement of nitrogen in air: NO, NO_2, HONO, HNO_3, water vapor: H_2O, sulfur species due to presence of sulfur in fuel: SO_2, SO_3, H_2SO_4, radicals: H, O, OH, and others. The above are briefly summarized in *Figure 1.1.1.*

Species formed directly from the combustion process, continue to evolve downstream of the combustor, both within and outside the engine. For an aircraft gas turbine engine, the mass flow from the combustor will go through the turbine stages and the nozzle, and perhaps an afterburner for some supersonic engines. The flow will continue to experience significant unsteady fluid mechanical changes as well as thermodynamic changes from the combustor exit to the exit of the engine. Both changes are major driving forces of shifts in local chemical composition of the mass flow. Further, addition of cooling flow for turbine blades and mixing of bypass air will produce more changes to the chemistry. Therefore, the emission levels coming from the engine are different from that of the combustor.

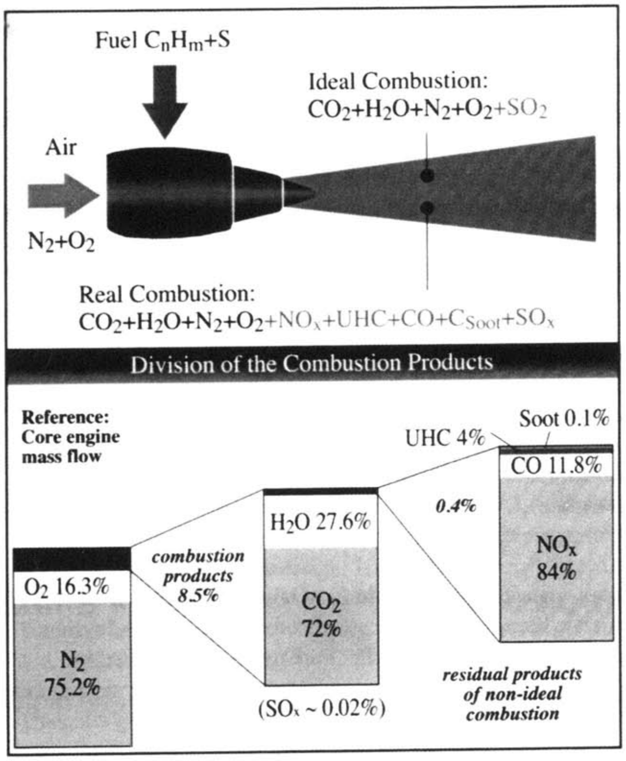
Fuel C_nH_m+S
Ideal Combustion:
$CO_2+H_2O+N_2+O_2+SO_2$
Air
N_2+O_2
Real Combustion:
$CO_2+H_2O+N_2+O_2+NO_x+UHC+CO+C_{Soot}+SO_x$
Division of the Combustion Products
Reference:
Core engine
mass flow
O_2 16.3%
N_2 75.2%
combustion products 8.5%
H_2O 27.6%
CO_2 72%
(SO_x ~ 0.02%)
0.4%
UHC 4%
Soot 0.1%
CO 11.8%
NO_x 84%
residual products of non-ideal combustion

Figure 1.1.1. Schematic of ideal combustion products (top), and all existing combustion products, showing scale of each [1]

1.2. Atmospheric Effects

The effects of aircraft emissions on the atmosphere can be divided into three categories: direct radiative forcing, indirect radiative forcing, and changes in ozone chemistry. These are described below.

1. Direct radiative forcing: Some species directly absorb radiation emitted by the Earth's surface and by clouds thereby tending to warm the planetary surface. Water vapor (H_2O), carbon dioxide (CO_2), nitrous oxide (N_2O), methane (CH_4), and ozone (O_3) are the primary greenhouse gases in the Earth's atmosphere [1]. As mentioned above, H_2O and CO_2 are major combustion products. Thus they will play a role in direct radiative forcing.

2. Indirect radiative forcing: There are some species that do not play a large direct role in changing the radiative balance, but lead to the formation of other species and/or physical phenomena that will have radiative forcing effect. Aerosols are typically included in this category. Aerosols are airborne suspensions of small particles. Aerosol particles emitted from aircraft engines include soot (carbon particles), metals, and H_2SO_4/H_2O; their precursors include sulfuric acid (H_2SO_4), water vapor, and possibly nitric acid (HNO_3, HNO_2) and unburned hydrocarbons. One of the major influences of aerosols is they provide more sites for nucleation and formation of ice particles, which may in turn lead to contrail formation – the white lined-clouds often visible behind aircraft engines. Contrails have positive radiative forcing that leads to global warming. Also, contrails may lead to increased cirrus cloud cover, which also produces positive radiative forcing.

3. Changes in ozone (O_3) chemistry: Ozone chemistry is affected by the NO_x species emitted by aircraft engines. NO_x emissions lead to formation of ozone in the upper troposphere but to destruction of ozone in the stratosphere. Since ozone itself is a greenhouse gas, production of ozone will lead to global warming. However, stratospheric ozone also provides a shield against solar ultraviolet radiation, which can promote formation of human skin cancers. Thus it would be desired to maintain a certain level of stratospheric ozone for protection, while not producing any ozone in the troposphere that will lead to positive radiative forcing.

1.3. Modeling of Engine Emissions

To minimize the impact of aircraft emissions on the environment, it is necessary to control emission levels of certain species that produce negative impacts. Before an effective method of control can be defined, a thorough understanding of how the species of concern evolve through the combustor and the rest of the engine must be obtained. With the adverse conditions (high temperature, high pressure, etc) and complex structure inside an aircraft engine, measurement of chemical species is very difficult at many locations. Plus, some of the species are challenging to measure due to their highly reactive nature. To address these difficulties, there is a need for modeling of the evolution of chemical composition of the flow going through an aircraft gas turbine engine. Details of the modeling methodology will be discussed in Chapter II.

The research effort being carried out at the MIT Gas Turbine Lab (GTL) concentrates on modeling of the chemical change from combustor exit to engine nozzle exit. The model being developed is applicable to any generic subsonic gas turbine engine with homogenous gas-phase chemistry. Continuous developments and changes to the model have been accomplished by Lukachko [2], Chobot [3], Han [4], as well as colleagues from Aerodyne Research, Inc. Please refer to the corresponding references for more details.

Currently, the modeling methodology incorporates 3-D computational fluid dynamics (CFD) calculations and 1-D kinetics calculations. The CFD tool being used is capable of calculating passively reacting flow, i.e. no feedback of heat release due to chemical reactions on changes in local temperature. A set of truncated gas-phase homogeneous chemical mechanisms involving 29 species and 73 reactions by Mueller *et al.* [5] is used in the calculations. This modeling methodology has been recently validated through comparison to measurements obtained from a NASA/QinetiQ (formerly DERA) collaborative effort to measure emissions both at combustor exit and nozzle exit of an aircraft gas turbine engine. More details about the validation, carried out as part of this thesis effort, will be covered in Chapter III.

This thesis also details the inclusion of a mass addition capability in the CFD code as a refinement to the modeling methods. To protect nozzle guide vanes (NGV) and rotor blades from failing in the very high temperature environment in the turbine stage of the engine, blade cooling is used extensively. For film cooling, cooler air bled from the compressor stage is injected onto the blade surfaces to act as a cool protective layer. Previously, this effect was simulated by setting a blade wall temperature that is equivalent to the temperature of the cooling air. With that, the "blade cooling" only reproduced the effects of temperature changes on local composition of species, not the additional effects associated with the introduction of air near the walls. It has been expected that when air is injected, it would provide more nitrogen and oxygen that will enhance NO_x formation and possibly SO_x formation due to extra O (atomic oxygen) that may be present from reaction of oxygen with other radicals. Therefore, mass addition capability was added to the CFD code to investigate the effects of blade cooling on the production of emissions. Chapter IV will provide more information on how the capability was added while Chapter V will discuss the impacts present when mass addition is included in the simulation.

With a complete methodology to model emissions coming from an engine, emissions from different engines with different engine cycles can be simulated with a relatively short period of time. This will allow investigation of how engine design changes affect emissions. Furthermore, effects of internal non-uniformities, e.g. non-uniform temperature profiles from combustor exit, local temperature non-uniformities due to blade cooling injection, etc., can also be investigated. Eventually, this will help to guide designs of future engine cycles as well as counter-measures to minimize engine emissions.

The objectives of this thesis are: 1. to assess the agreement of current modeling methodology with actual engine measurements, to determine the causes for any discrepancies, and to recommend changes to improve the model; and 2. to estimate the effects of mass addition in species evolution. The ultimate goal is to have an accurate and comprehensive model that captures the impacts of various parameters, e.g. temperature non-uniformity, engine cycle, mass addition, etc., on evolution of trace species. Such a model can then help in the design of future engines to minimize and control emissions.

II. Current Modeling Methodology

In this thesis, numerical simulations are used to estimate emissions from aircraft gas turbine engines. As mentioned previously, modeling has the advantage of having a shorter turnaround time as well as much lower cost when compared to experimental engine measurements. Furthermore, even for the same engine, the composition of species may differ drastically depending on the operating conditions, e.g. power level (cruise, take-off, etc.), altitude (different temperature, pressure, etc.). Therefore, it would require significant resources to obtain complete emissions characteristics of a particular engine. In addition, for in-flight measurements, it is very difficult to measure what is coming out of the engine since the species will react and mix with the local atmosphere once they leave the engine. By the time the measurement sample is obtained from the measurement probe of the chasing aircraft, the composition will have changed somewhat already. For these reasons, modeling is a valuable means to investigate the evolution of engine trace species emissions. One important caveat is that it is difficult to assess the computational models due to the scarce amount of detailed measurements available. One assessment carried out through the NASA/QinetiQ collaborative effort will be discussed in Chapter III.

The modeling methodology described in this thesis is an extension of methodologies developed and refined by Lukachko [2], and Chobot [3]. The model includes the flow path from combustor exit to engine nozzle exit. It aims to investigate the dependence of emissions production on engine parameters. Instead of going on to investigate how the species evolve after exhausted into the atmosphere, the model provides the engine exit condition as an input condition for other global atmospheric and wake/plume models for researchers working in those areas.

2.1. Modeling Tools Available

Before discussing the results of modeling calculations, it is necessary to first describe the modeling tools that are available. Two tools were used: 3-D computation fluid dynamics (CFD) calculations and 1-D kinetics calculations.

The 3-D CFD tool is called CNEWT. It is built on the NEWT turbomachinery CFD code [6], [7], which employs a vertex-centered, finite-volume method with a 4-step Runge-Kutta time discretization scheme to solve full Reynolds-averaged Navier-Stokes equations for three-dimensional geometries. Unstructured grids with tetrahedron cells are used. NEWT itself calculates the flow properties, i.e. temperature, pressure, density, velocities, etc., but it does not have the capability to calculate the chemical reactions present in the flow path that are of interest.

Thus, Lukachko [2] incorporated CHEMKIN into NEWT to form CNEWT. CHEMKIN calculates gas phase homogeneous chemical kinetics when the flow properties and the desired chemical mechanism are provided. CNEWT is an integration of the two programs above to calculate passively reacting internal flows. It is named "passive" because there is no feedback of any heat released from reactions to change the flow properties. Multiple inlet/exit and parallel computing capabilities were added to CNEWT by Chobot [3] and John Zhang from Aerodyne Research, Inc. They are aimed to allow higher versatility on geometries being calculated and to allow faster computing time, respectively.

The 1-D tool available is called CALCHEM. It allows computation of changes of chemical species on a single streamline. Temperature, pressure, and velocity profiles of that streamline must be provided as an input. They can be estimated from actual engine data and/or with engine cycle analysis. The advantage of the 1-D calculation is that it takes a much shorter time to calculate (several minutes versus ~1 week for the 3-D CFD calculation). Hence it is very useful when local non-uniformites (2-D/3-D effects) are not important, as well as when changes of the chemistry are known to be slow.

2.2. Choice of Tool to Use

With the above two tools available, it is necessary to decide which tool to utilize. A full 3-D CFD calculation from combustor exit to nozzle exit has the potential for fully replicating the effects of evolution of trace species. However, the calculation would require computational resources in excess of those available, and detailed geometries inside the engine, which are proprietary in most cases. On the other hand, there are no such problems with the 1-D calculations, but it is hard to capture local non-uniformities since the calculation is only representative of a single streamline. To decide which tool to use and for which locations in the engine, a time scale analysis is utilized.

2.2.1. Time Scale Analysis

Any given chemical reaction will tend towards an equilibrium value that is a function of the temperature, pressure, and local species composition provided that sufficient time is provided. However, different chemical reactions take different amounts of time – chemical time scales, to achieve equilibrium. From combustor exit to nozzle exit, the flow undergoes continual changes in temperature and pressure due to work extraction and changes of velocity, i.e. flow time scale. Therefore, the species may not have enough time to reach the equilibrium at a particular location before moving to another point with another temperature and pressure hence another equilibrium speciation. The ratio of the flow time scale to the chemical time scale is known as the Damköhler number (Da):

$$Da = \frac{\tau_{flow}}{\tau_{chem}} \tag{2.2.1}$$

With a Damköhler number larger than 1, equilibrium is achieved. Conversely, if it is less than 1, equilibrium is not achieved. With that in mind, a severity parameter, developed by Lukachko [2], can be calculated for the species of interest, with SO_3 as an example:

$$\Delta SO_3 = Da_{SO_3}\left(\left[\frac{SO_3}{SO_x}\right]_{equil} - \left[\frac{SO_3}{SO_x}\right]_{current}\right) \tag{2.2.2}$$

The above equation allows a severity parameter plot to be generated for the species of interest at different temperature and pressure regions.

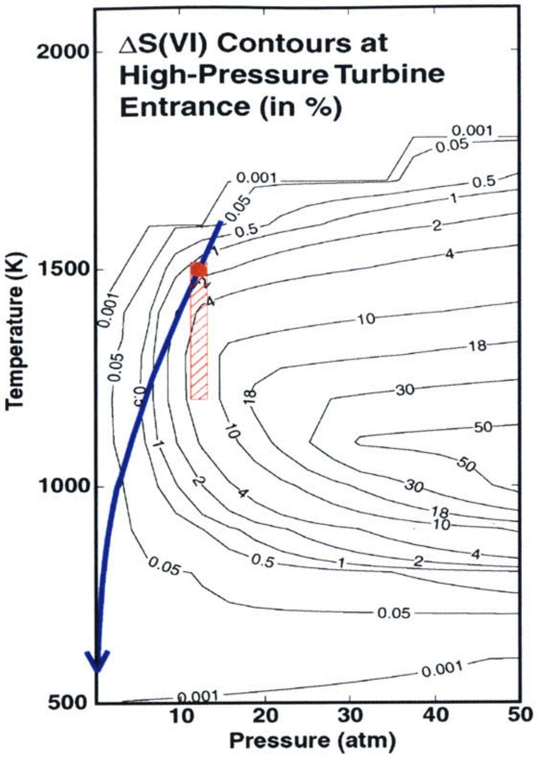

Figure 2.2.1. Severity parameter plot for SO_3 at combustor exit condition (from Lukachko)

Figure 2.2.1 contains contour lines that correspond to the potential of formation of SO_3 at different temperatures and pressures. The higher the contour, the more SO_3 will tend to be formed. The blue line on the figure corresponds the changes of temperature and pressure along the flow path from combustor exit to nozzle exit of an example engine. The red point corresponds to the combustor exit condition. It can be seen that when temperature is dropped locally from the red point (red cross-hatched area), due to the effect of blade cooling, it can lead to higher formation of SO_3. This implies a CFD calculation may be necessary for calculation of the high pressure turbine in order to capture the effects of local temperature non-uniformities. Although *Figure 2.2.1* is only for SO_3 for a particular engine condition, it has been found that the species of interest: SO_3 and NO_2, have similar severity parameter plot contours and that local blade cooling may have a significant effect on species formation. HONO shows slightly different behavior that seems to be very dependent on the engine cycle. In some cases, more HONO will be produced due to blade cooling while in other cases HONO depletion occur. More details on the time scale analysis are discussed in Lukachko [2] and Han [4].

2.2.2. Choice of Tools

With the above considerations, a CFD calculation is used for the first stage of the high pressure turbine (HPT1) with a nozzle guide vane (NGV) followed by a rotor. Local non-uniformities present such as blade cooling and unsteadiness of the rotor stage can thus be captured. From the exit of the HPT1 to the nozzle exit, a 1-D calculation is used since the flow should be more uniform after going through the HPT1 and the species should be less reactive due to the lower temperature present in that region. With this combination, this methodology is expected to capture most of the major effects on the species while keeping the computational time reasonable.

2.3. Calculation Across HPT1

As mentioned above, CFD is used to calculate the species evolution across the HPT1. The HPT1 is separated into the stationary NGV stage and a rotating rotor stage. To carry out the calculations, geometry of the stages must be provided. Profiles of the blades were obtained from NASA/QinetiQ TRACE engine data. To further reduce the computational time, only a thin radial section (2 cells thick) at the mid-span location was gridded using PRE, the NEWT-associated grid generation tool, by Chobot [3]. Thus the calculation is more "2-D" rather than "3-D" as any radial effects or variations will not be captured. In an actual scenario, the blades themselves are not radially-uniform, nor is the flow due to secondary flow phenomena, blade-endwall interactions, etc. However, to reduce computational requirements this was necessary. It is expected that the primary effects, e.g. temperature, pressure, residence time, on species evolution will be effectively represented.

For the geometry, it is also necessary to decide how many blades to include. Including the exact number of blades as in the actual engine is not necessary if the inlet condition is uniform or somewhat periodic. Therefore, the grid contains three blades such that effects of circumferential non-uniformities can be investigated as Chobot [3] found that the circumferential distance of three blades is approximately the same as one full period of the inlet non-uniform profile due to placements of the cannular combustors in the test engine. The exact NGV blade profiles were obtained from NASA/QinetiQ (Chapter III) data and implemented by Chobot [3]. The NGV grid is shown at *Figure 2.3.1.*

Similar treatment is used for the rotor blade row. Instead of having 3 blades in the grid, there are 5 blades for the rotor to capture the correct rotor-stator blade ratio of the engine. The rotor grid is shown at *Figure 2.3.1.* Since the rotor is rotating, unsteady calculations were required to capture the effect. This was achieved by setting a rotating inlet condition for the rotor calculation in CNEWT.

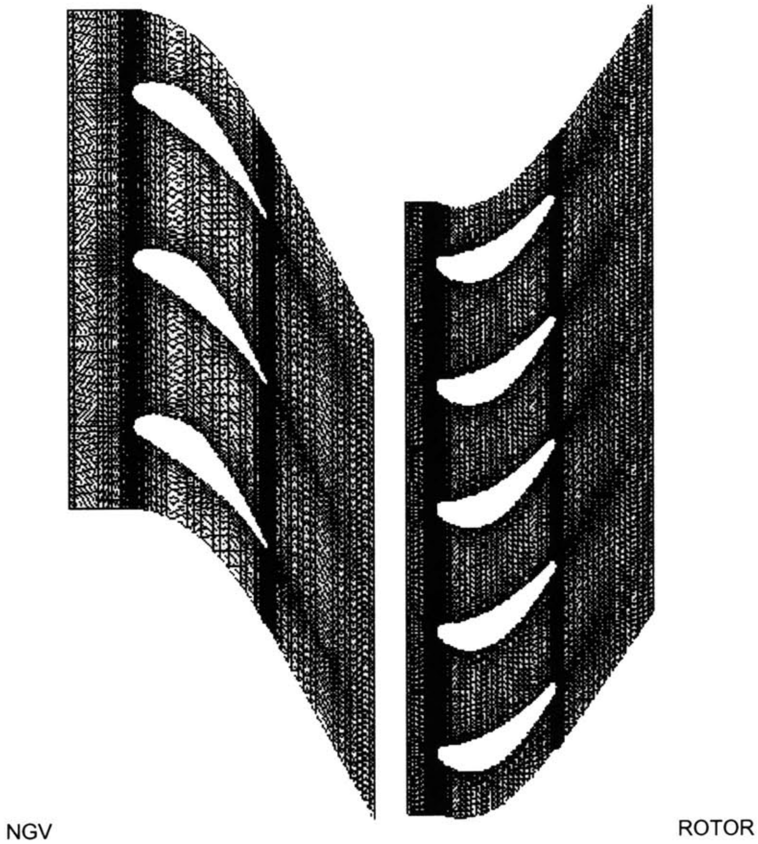

BLADE ROW CHARACTERISTICS	HPT 1 NGV	HPT 1 ROTOR
Actual Blade Count	60	100
Chord	31.44 mm	19.18 mm
Axial Chord	23.09 mm	16.79 mm

Figure 2.3.1. Grids for the NGV (left) and rotor (right) for CFD calculation

2.3.1. HPT1 Inlet Condition

To start the modeling calculation, the HPT1 inlet condition (station 4 in *Figure 2.3.2*), the same as combustor exit condition, is required. The condition depends on the engine operating condition and the corresponding engine cycle. *Figure 2.3.2* shows the cross-section of the QinetiQ TRACE engine (Chapter III) that was used to develop the modeling methodology.

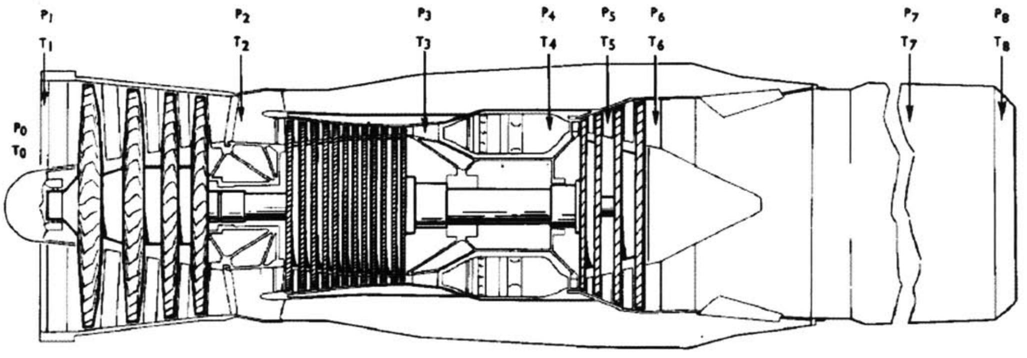

Figure 2.3.2. QinetiQ TRACE engine showing instrumentation points [8]

From the engine cycle for a particular operational mode, the condition at the combustor inlet (station 3) can be calculated. To obtain the species composition at the combustor exit, the combustion process must be simulated. Ideally, a case-specific combustor simulation should be carried out to obtain an accurate composition at the exit since the composition strongly affects the calculations from combustor exit to nozzle exit. However, such a calculation would be very challenging. So, Lukachko [2] devloped a method to approximate the combustor exit condition based on the following information in *Table 2.3.1*.

The combustor exit temperature is approximated using an adiabatic flame temperature calculation based on the fuel type being used. Pressure is assumed to be the same as that at combustor inlet. Equivalence ratio, which is the ratio of fuel-air ratio to stoichiometric fuel-air ratio, determines how rich/lean the combustion is carried out. Currently, almost all aircraft engines operated fuel-lean to minimize emissions and to keep the combustor exit temperature reasonably low. Although higher combustor exit temperatures will increase the efficiency of the thermal cycle, exceedingly high temperatures will also damage or melt the turbine blades that are under extreme stress, even with blade cooling. Combustion efficiency denotes how complete the combustion is. Whereas the $CO/H_2/HC$ ratio determines what species are responsible for the incomplete combustion. EI NO_x, NO/NO_x ratio, EI S, SO_3/SO_x ratio, and EI CO determine the composition of NO_x, SO_x, and CO_x at the combustor exit. With all the above information, the combustor exit condition can then be approximated.

Input to generate combustor exit condition
Temperature (K)
Pressure (atm)
ϕ Equivalence Ratio
η Combustion Efficiency
CO/H2/HC ratio
EI NOx
NO/NOx ratio
EI S
SO3/SOx ratio
EI CO

Table 2.3.1. Input information required to generate combustor exit condition

2.3.2. Non-uniform Inlet Condition

The previous section described how to create the inlet condition for NGV. However, the above inlet condition specification will only allow for uniform inlet conditions since only one temperature, pressure, and equivalence ratio is used. However, the combustor exit condition is typically non-uniform. One of the reasons is the distribution of discrete fuel injectors and also tailoring of the radial temperature profile to reduce turbine blade temperatures near the tip and the hub. Further, while most current engines use full annular combustors, many older engines, such as the one used for assessment of the methods (shown in *Figure 2.3.3*), employ separate combustor cans which lead to additional circumferential and radial non-uniformity at the combustor exit.

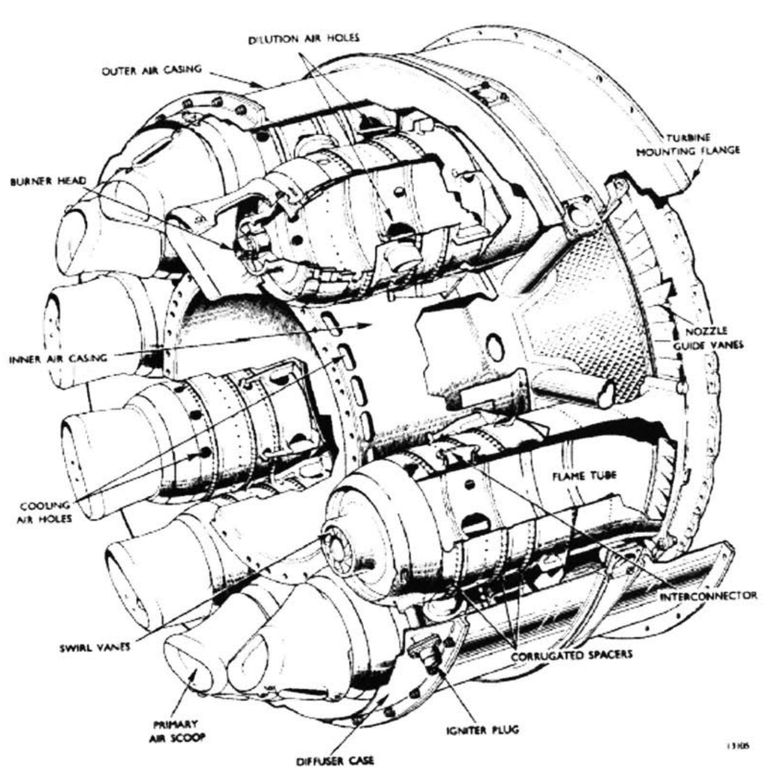
DILUTION AIR HOLES
OUTER AIR CASING
TURBINE MOUNTING FLANGE
BURNER HEAD
NOZZLE GUIDE VANES
INNER AIR CASING
FLAME TUBE
COOLING AIR HOLES
INTERCONNECTOR
SWIRL VANES
CORRUGATED SPACERS
PRIMARY AIR SCOOP
IGNITER PLUG
DIFFUSER CASE

Figure 2.3.3. QinetiQ TRACE engine combustion system [8]

As shown in *Figure 2.3.3*, the combustion system of the engine is composed of a number of "can" type combustors. Each of those combustors has their own fuel injection system, mixing zones, dilution air cooling, etc. Due to the cooling of the combustor walls, the temperature distribution at the combustor exit, will be hotter at the center and cooler near the wall (*Figure 2.3.4*). Also with the injection of dilution air on the wall, the equivalence ratio will be lower near the wall as well. Therefore, the species composition will not be uniform at the combustor exit (*Figure 2.3.4*).

Chobot [3] simulated the effect of temperature non-uniformities by setting a sinusoidal profile with the wavelength corresponding to a circumferential distance of three blades. However, this method does not provide a full non-uniform representation since the equivalence ratio and species initial conditions were assumed to be uniform. To further refine this specification method, a full non-uniform inlet condition generation methodology was developed.

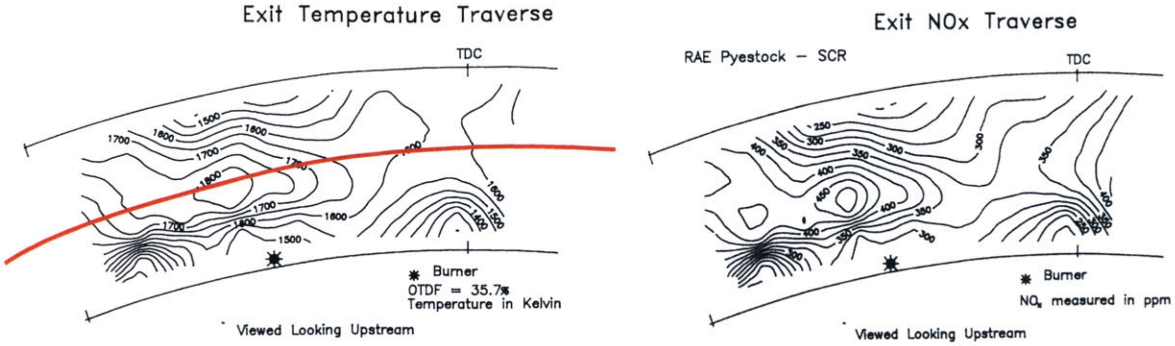

Figure 2.3.4. Temperature distribution (left), and NO$_x$ distribution (right), looking upstream of combustor exit [9]

To specify a full non-uniform inlet condition, the mean temperature and the desired temperature range must be known. The temperature range can be expressed as "pattern factor". The larger the pattern factor, the bigger the temperature range at combustor exit.

$$PatternFactor = \frac{T_{\max} - T_4}{T_4 - T_3} \tag{2.3.1}$$

By choosing a pattern factor, along with a known combustor inlet temperature as well as mean combustor exit temperature, the maximum temperature, and the minimum temperature, can be calculated. The known temperature range is then fitted into a sinusoidal profile to replicate the change in temperature when moving across the combustor exit circumferentially (red line in *Figure 2.3.4*). With the sinusoidal temperature profile, 22 evenly spaced points are then picked from the profile. For each point, with the same combustor inlet temperature but different combustor exit temperature, an adiabatic flame temperature calculation is then carried out to determine the corresponding equivalence ratio for that point. With the temperature, pressure, and equivalence ratio for each point, the process described in section 2.3.1 can then be carried out for each individual point to obtain the resulting species composition. After repeating this process for the 22 points, the data are then interpolated to produce a full non-uniform inlet condition profile. 22 points are found to be sufficient to represent the sinusoidal profile.

2.3.3. NGV Calculation

Several inputs are required to carry out the CFD calculation on the NGV. One needs to specify the inlet total pressure, inlet total temperature, inlet flow angle, exit static pressure, and blade temperature. The exit static pressure is obtained by doing a velocity triangle analysis on the NGV (more details on velocity triangle analysis are provided in [10], [11]). With CNEWT, the blade cooling effect is simulated by setting a non-adiabatic wall boundary condition, i.e. a wall temperature, usually cooler than free-stream, on the blade surfaces. Chapter IV will discuss improvements to enable cooling air injection to be modeled. In addition to the above information, the circumferential profile for temperature and species obtained from the full non-uniform inlet condition are also required. A typical result would look like *Figure 2.3.5* where the static temperature is presented.

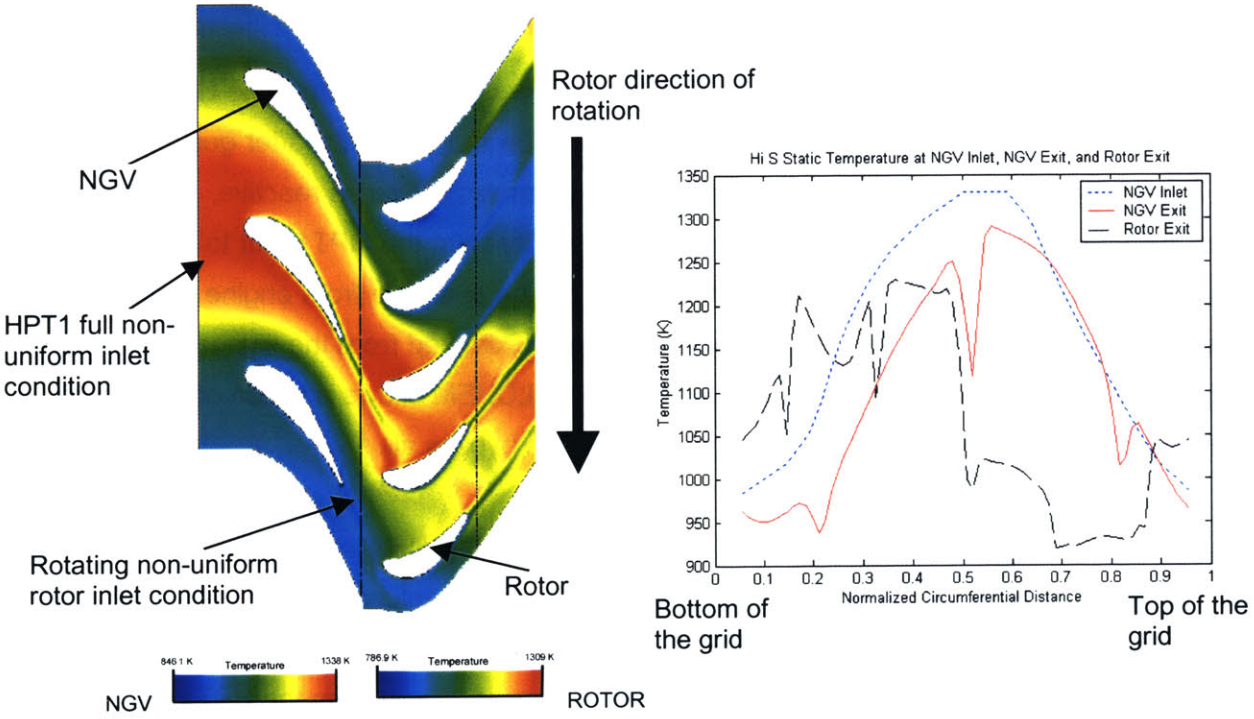

Figure 2.3.5. Static temperature profiles across HPT1, with NGV and rotor calculations

2.3.4. Rotor Calculation

After the calculation across the NGV, the flow condition and species composition obtained from the NGV exit are then used as the inlet condition for the rotor calculation. In the past, a mixed-out assumption was used for simplicity. With the mixed-out assumption, the NGV exit profile obtained would be mass-averaged to obtain a uniform rotor inlet condition. This is not as accurate as the current methodology that uses the non-uniform profile from NGV exit. Since the rotor calculation is separate from the NGV calculation, the NGV exit condition cannot go directly into the rotor inlet condition. Therefore, a number of points are then picked from the NGV exit profile from the CFD post-processing program Visual 3 and are interpolated to produce the inlet condition for the rotor calculation. A sample rotor result is also shown in *Figure 2.3.5.*

2.4. Calculation from HPT1 Exit to Nozzle Exit

As mentioned above, the 1-D tool (CALCHEM) was used for calculations from the HPT1 exit to the nozzle exit because it is assumed that the flow would be more uniform after going through the HPT1 and the temperature is lowered so that the species will not be as reactive. To use the 1-D tool, axial profiles of temperature, pressure, and velocity from the HPT1 exit to nozzle exit must be provided. In most cases, detailed profiles will not be available from engine companies for proprietary reasons. Thus, the profiles are usually approximated from the limited amount of data points available for each engine being simulated. CALCHEM allows addition of dilution air along the flow path to simulate the effects of mixing with the bypass air.

Previously, the flow conditions and species compositions at the HPT1 rotor exit were mass-averaged circumferentially to obtain the mean values. The mean values were then used as the input condition for the 1-D calculation. With this method, only the averaged, mixed-out composition would be obtained at the nozzle exit. However, as shown from the HPT1 results at *Figure 2.3.5,* some non-uniformities from combustor exit persist through the HPT1. Therefore, if the non-uniformities indeed proceed through the rest of the engine from the HPT1 exit to the nozzle exit, there would be some sort of profile, or ranges in terms of species concentrations, existing at the nozzle exit. In order to capture this effect, 1-D calculations were carried out on multiple streamtubes from the HPT1 exit profile, assuming that the mixing between individual streamtubes is negligible.

The points were chosen based on the temperature difference between the consecutive points. This allowed more points to be sampled at locations where the temperature change is relatively larger. Points chosen from one sample case are shown in *Figure 2.4.1.* These points not only possess different temperatures, they are also of different pressure and different velocities due to the effects from upstream rotor blade rows. The composition of the species will be different as well.

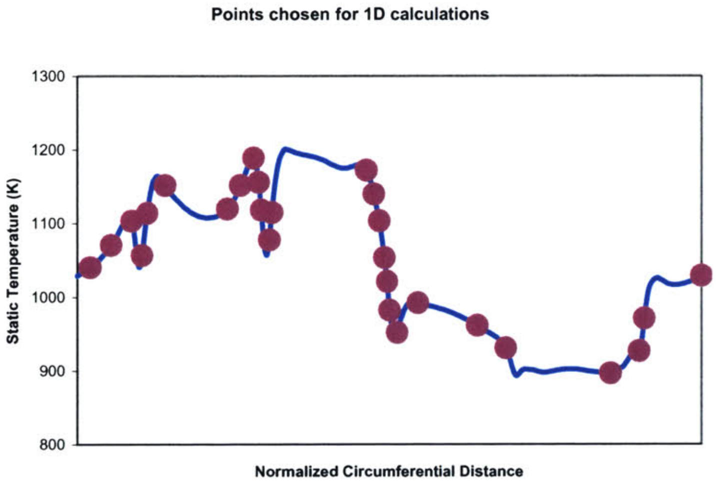

Figure 2.4.1. Points along the rotor exit temperature profile chosen for 1-D calculations

III. Modeling Assessment with NASA/QinetiQ Engine Test

This chapter describes an assessment of the accuracy of the modeling methodology that was described in Chapter II. To perform such an assessment, it is necessary to have detailed engine emissions measurements, especially measurements of aerosol precursors such as SO_3, HONO, etc., at both the combustor exit and the engine exit. However, measurements such as these are not common since they are very difficult to make with some techniques still in development.

In response to increasing concerns about the effects of sulfate aerosols and their precursors on physical and chemical processes in the upper atmosphere including persistent contrail formation and ozone depletion (discussed in chapter I), NASA and QinetiQ (formerly DERA) joined together in an experimental effort to obtain such measurements. This provided an opportunity to assess the modeling methodology. The model results were also used during the development of the experiments to help guide the test plan.

3.1. Measurement Program

The engine involved in the NASA/QinetiQ program is the QinetiQ TRACE engine. It is a generic engine with technology typical of some of the older aircraft still flying. The engine contains two stages of high pressure turbine (HPT) and two stages of low pressure turbine (LPT), followed by a forced mixer and a nozzle (*Figure 2.3.2*). To obtain measurements at both combustor exit and nozzle exit, two separate measurement programs have been carried out: a combustor test program, and an engine test program. The tests represent the first time that measurements of trace species have been collected from both the combustor exit plane and the engine exit plane on similar hardware and test conditions.

3.1.1. Combustor Test Program

The combustor test program was performed in August/September 2000 at QinetiQ Pyestock. The testing was performed on the QinetiQ TRACE engine combustor. The TRACE engine is fitted with 10 cannular combustors (*Figure 2.3.3*) which are representative of a CAEP (Committee on Aviation Environmental Protection) 4 compliant engine. Instead of testing the whole combustor, a single "can" (flame tube) of the combustor was tested on the Sector Combustor Rig (SCR) at QinetiQ Pyestock. The rig allows separate control over temperature (up to 900 K), mass flow (up to 5 kg/s), and pressure (up to 10 atm). Two power conditions (*Table 3.1.1*) along with fuel sulfur level ranging from 8 ppmm to 11650 ppmm were tested. Data including CO, NO_x, NO, NO_2, CO_2, O_2, smoke number, particulate number density and size distribution, SO_2, SO_3, and HONO, were collected at the exit plane of the combustor. Please refer to [12] for more information about the combustor test.

Combustor Inlet Conditions

	Uprated Cruise	Standard Cruise
Temperature	588 K	566 K
AFR	56	66
Pressure	7.99 atm	7.05 atm
Mass Flow	2.29 kg/s	2.12 kg/s

Table 3.1.1. Two power conditions for combustor test

3.1.2. Engine Test Program

The engine test was carried out in July 2001 at QinetiQ Pyestock in the Glen Test House (GTH), U.K. Measurements were performed at the nozzle exit of the QinetiQ TRACE engine. There are a number of independent controls on engine parameters available, such as air bleeds and inlet blade angles. These allowed the engine to be operated at a configuration different from the normal running schedule. Four tests were performed in total, including a commissioning run, and three tests with different fuel sulfur levels. For each sulfur level, two power levels, both uprated cruise and standard cruise were run. The run conditions are summarized at *Table 3.1.2.*

The engine was configured to match the combustor test conditions as closely as possible although there are still some discrepancies especially in pressure. The same set of species measured in the combustor test was also measured in the engine test. Spatial variations (radially) of the species were obtained with a traversing probe. Additional details of the engine tests are discussed in [8].

		Uprated Cruise			Cruise		
	*	*Low Sulfur*	*Medium Sulfur*	*High Sulfur*	*Low Sulfur*	*Medium Sulfur*	*High Sulfur*
Fuel Sulfur Level (ppmm)	M	< 10	460	2060	< 10	460	2060
Combustor Inlet Temperature (K)	C	535	554	554	548	577	577
Combustor AFR	M	68	59	57	64	65	64
Combustor Air Flow (kg/s per combustor)	C	1.7	1.9	1.9	2	2.3	2.3
Combustor Exit Temperature (K)	C	1083	1175	1194	1125	1142	1150
Combustor Exit Pressure (atm)	C	5.7	6.5	6.5	6.5	7.7	7.7
Low Pressure Turbine Exit Temperature (K)	M	808	805	805	771	768	781
Low Pressure Turbine Exit Pressure (atm)	M	1.3	1.3	1.4	1.4	1.4	1.5

** M = measured, C = calculated*

Table 3.1.2. Engine test run conditions

3.2. *Modeling of the NASA/QinetiQ Test Engine*

As a component of the NASA/QinetiQ emissions testing effort, MIT and Aerodyne Research, Inc. (ARI) carried out calculations of the evolution of trace species using the model discussed in Chapter II. As described in Chapter II, the model requires combustor exit measurements to specify the initial conditions at the HPT1 inlet. Given the initial conditions, the model can then be used to obtain the changes of the species in the post-combustor flow path to the nozzle exit. However, the combustor measurements were not complete enough to fully specify the initial conditions because: 1. The emission indices between combustor measurements and full engine measurements did not match. 2. Several species important to trace chemistry in the turbine, such as OH or O, could not be measured in the hot environment. 3. There were insufficient data to set up a spatially non-uniform inlet profile for the modeling calculation.

To address these difficulties, several approximations were required. First, instead of running all 6 cases carried out in the engine test, only two post-combustor simulations, differing in fuel sulfur level – low sulfur (<10 ppmm), and high sulfur (2060 ppmm) – but similar in operating conditions (cruise), were conducted. Second, the emission indices required for initial condition specification were obtained from the engine exit measurements instead of combustor exit measurements assuming the emissions indices remain constant through the post-combustor flow path. The sections below discuss these approximations in more depth.

3.2.1. Initial Conditions

As described in Chapter II, the modeling methodology can be separated into three parts. The first part is the CFD calculation of the HPT1 NGV stage. Species and flow initial conditions for the NGV at HPT1 inlet were generated using engine test data supplemented by approximations where necessary. The second part is the CFD calculation of the HPT1 rotor stage. Results from the NGV exit are used as the inlet condition for the rotor simulation. The last part is a series of 1-D calculations along various streamlines from the rotor exit to the exhaust nozzle. Similarly, results from the rotor exit were used to specify the inlet conditions for the 1-D calculations.

I. HPT Inlet Temperature Profile

Chapter II mentioned that a non-uniform temperature profile exists at the combustor exit due to the cannular combustor placements. Along with the temperature non-uniformity are species non-uniformities. Subsequent combustor measurements conducted in the NASA/QinetiQ combustor test displayed a combustor exit temperature which varies mostly in the radial direction (*Figure 3.2.1*).

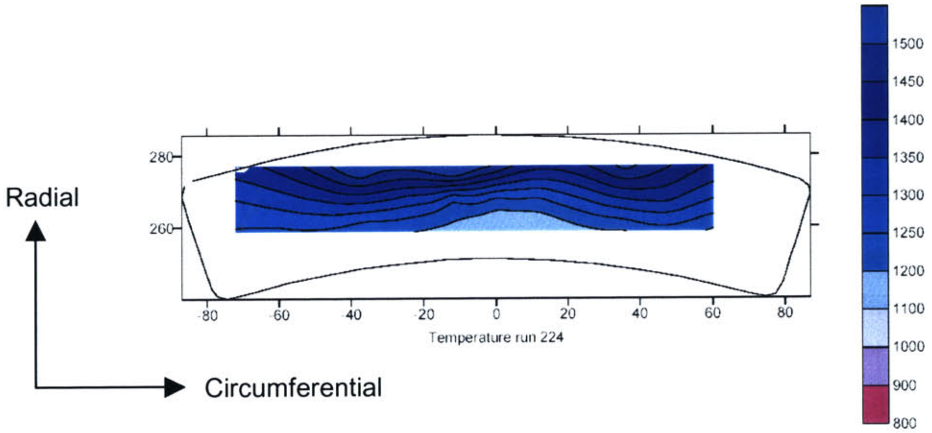

Figure 3.2.1. Temperature (K) distribution at combustor exit [8], [12]

Therefore, if a similar mid-span slice were to be taken from the temperature map above, it would give an almost constant temperature profile and would not reflect the impact of temperature non-uniformity at the combustor exit. To represent the impact of radial non-uniformity, there are two options: 1. Generate a new NGV grid that has radial span in the CFD calculation. 2. Simulate the radial non-uniformity as a circumferential temperature/species non-uniformity. For the first option, the grid would become fully 3-D and require a much longer computation. For the second option, the calculation would not capture exactly the effects due to radial non-uniformity, but would approximate the effects of a temperature non-uniformity. The upper and lower NGV blades in the grid shown at *Figure 2.3.1* can be treated as slices of the same blade at different radial positions experiencing different temperature. The second option was employed largely due to computational constraints.

In the NGV calculation, a circumferential temperature profile was specified based on the shape of profile used in [3]. The mean temperature and the pattern factor of approximately 30% were taken from NASA/QinetiQ results. This allowed for a simulation that reflects the effects of a temperature non-uniformity on trace species chemistry. The combustor exit temperature profiles used for the two calculations are shown as the blue dotted line in *Figure 2.3.5.*

II. HPT1 Inlet Equivalence Ratio Profile

Since the TRACE combustor exhibits very high combustion efficiency (almost complete combustion) and heat loss is assumed to be minimal, i.e. adiabatic, the varying temperature profile discussed in the section above would be solely due to a variation of fuel-air ratio at the combustor inlet and mixing with cooling and dilution flows within the combustor. To calculate the fuel-air ratio profile, adiabatic flame temperature calculations were performed to find the fuel-air ratio associated with the temperature at each point on the combustor exit profile. A combustion efficiency of 99.9% was used, which is similar to the results from both the combustor and engine tests (~ 99.83% - 99.93%).

III. Trace Species Concentrations Profile

With the temperature and fuel-air ratio profiles determined, the associated concentrations of trace species were then specified. Note that for constant emission indices, the amount of a particular species will vary across the combustor exit along with the temperature and fuel-air ratio profile. For the species specification, measured emissions data were used whenever possible to specify the combustor exhaust levels. The emission indices of NO_x and CO were obtained based on averages of measurements taken at the engine nozzle exit plane. EI S was obtained from fuel analysis.

In the results to be covered later in the chapter, it will be seen that oxidation within the SO_x and NO_y families may be significant. However, the emission indices of the species family considered together are basically invariant through the engine. For other species, such as H, O, and OH, they are set to their equilibrium values at the respective temperature, pressure, and equivalence ratio within the combustor exit profile.

Although it can be assumed that the EI S and EI NO_y remain approximately constant from combustor exit to engine exit, the extent of oxidation within SO_x and NO_y is not known at the combustor exit. As described in Chapter II, along with the emission indices, it is also necessary to specify the NO/NO_x and SO_3/SO_x ratio for the initial conditions for the HPT1 NGV calculation. In the NASA/QinetiQ assessment calculation, the NO/NO_x ratio was set to 1 while SO_3/SO_x ratio was set to 0. This implies that at the combustor exit, all the NO_x is in the form of NO, and all the SO_x is in the form of SO_2. This approximation was used instead of using the averaged data obtained from the combustor test measurements since these data did not provide enough information to set up a non-uniform species profile. When the averaged data from the tests was used, several problems were encountered as described below (*Figure 3.2.2).*

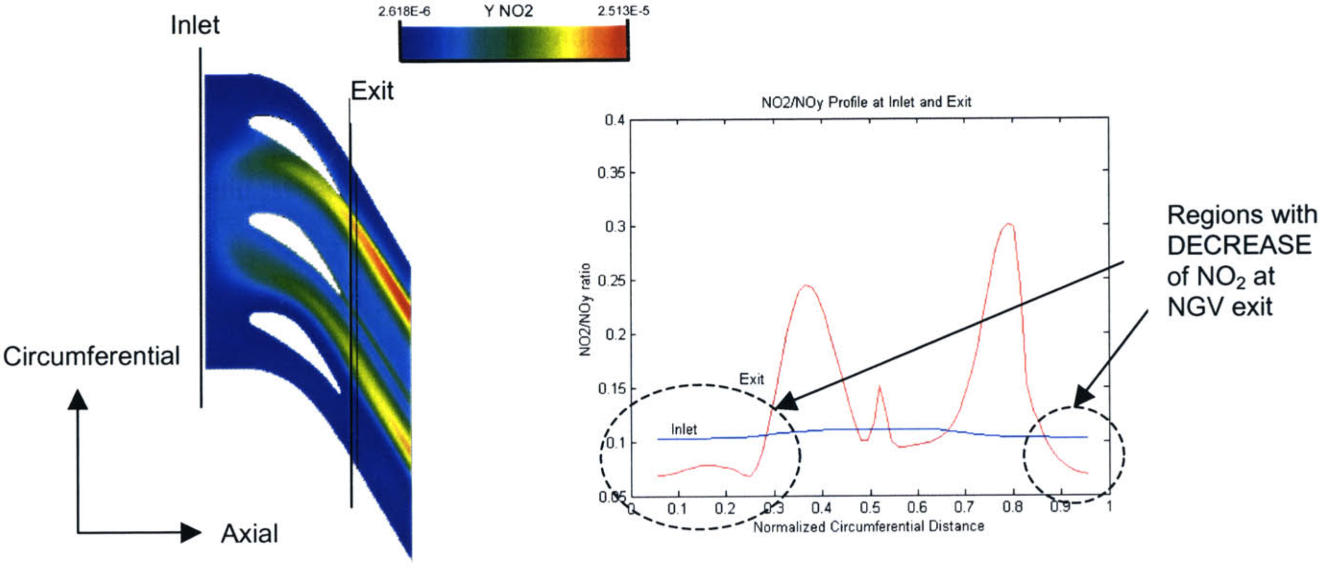

Figure 3.2.2. NO_2 results across NGV with incorrect inlet specification

In *Figure 3.2.2*, the plot on the left shows the evolution of NO_2 across the NGV stage, and the plot on the right shows the circumferential profile of NO_2 cut at the inlet plane and at the exit plane (as shown in the figure). For both NO_x and SO_x, monotonic oxidation from combustor exit to nozzle exit is expected with NO_2 and SO_3 concentrations increasing through the engine. However, the NO_2 profile plot in *Figure 3.2.2*, reveals several circumferential locations where there are decreases of NO_2 from inlet to exit. This occurs because of incorrect specification of the initial conditions. *Figure 3.2.3* shows the NO/NO_y ratio at the inlet of the NGV, with the solid curve showing the equilibrium levels and the dotted curve showing the averaged level from measurements.

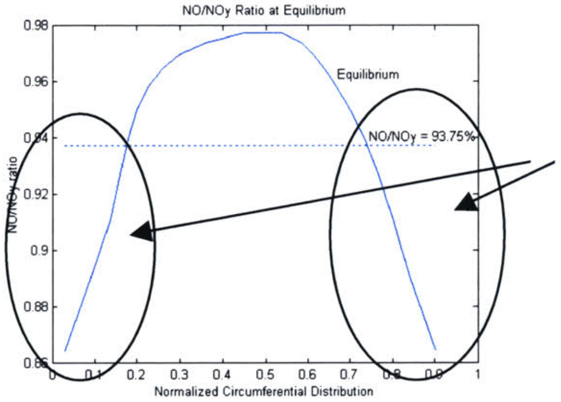

Regions with equilibrium level lower than averaged measurement

Figure 3.2.3. Equilibrium and averaged measured levels of NO/NO_y at NGV inlet

Note from *Figure 3.2.3* that there are regions, noticeably near low and high circumferential locations where the equilibrium level is lower than the averaged measurement, while near the center the equilibrium level is higher. Therefore, as the flow and species move downstream from the NGV inlet to NGV exit, the species approach the local equilibrium. The equilibrium level is changing moving downstream because of the continual change in temperature and pressure. If the level of NO_2 is set too high above the local equilibrium at the inlet (i.e. NO level set too low), the level of NO_2 will *decrease* rather than *increase*, as expected. This situation corresponds to the circled regions in *Figure 3.2.2*. A similar scenario occurs with SO_3 as well. Therefore, it can be concluded that it is not accurate for us to utilize the averaged measurement data in the calculation when inlet non-uniformity is involved. Instead, the NO/NO_x ratio was set to 1 and SO_3/SO_x ratio to zero to ensure monotonic changes. One problem associated with this assumption is the final NO_2 and SO_3 levels calculated will be lower than that expected by measurement.

The specification of trace species generated through the process described in Chapter II results in a set of concentrations that is elementally balanced, but not in quasi-equilibrium at the NGV inlet. In order to allow the species to achieve such a state, a 1-D constant temperature and pressure kinetics calculation is performed to remove any non-physical sudden readjustments of concentrations in the mixture [3]. Without achieving quasi-equilibrium, the sudden readjustments have been found to cause problems in the CFD calculation. Currently, the species concentrations at a point 0.02 ms (approximately 10% of the HPT1 stage flow through time) downstream of the plane of initial condition specification are used as input.

3.2.2. Run Matrix

As part of the planning effort for the NASA/QinetiQ combustor test and engine test, several pre-test runs were carried out based on the estimated combustor and engine test conditions. They were performed at two power settings – cruise and max power, with similar fuel sulfur levels. This is in contrast to the post-test simulations, which were conducted at the cruise power condition, but with different fuel sulfur levels.

From the QinetiQ engine test, a total of six different run conditions were measured at two power settings – cruise and uprated cruise, and three fuel sulfur levels for each power setting – low (<10 ppmm), medium (460 ppmm), and high (2060 ppmm). It is more desirable to carry out the numerical simulations with different power levels rather than different sulfur levels because it has been shown from time scale analysis [3] that the oxidation within NO_y and SO_y families is very dependent on the temperature. Unfortunately, due to limitations of the test facility, the cruise and uprated cruise power levels were very close to each other (*Table 3.1.2*) such that differences in modeling results would be minimal. Thus, two runs with different fuel sulfur levels were simulated instead.

Table 3.2.1 provides a summary of the pre-test run conditions compared with the post-test simulations reported in the following section. Most conditions were specified by actual test conditions or measurements. Parameters in italic were calculated from engine test data. Parameters in gray were assumed, as discussed above. The combustion efficiency and EI CO (not shown) are consistent with each other.

Parameter	Pre-Test Cruise	Post-Test High-S	Post-Test Low S
Combustor exit temperature (K)	1123 (constant)	978 - 1322	952 – 1298
Pattern factor (profile shape from data)	—	30%	30%
Combustor exit pressure (atm)	6.8	7.7	6.5
Blade surface temperature (K)	825	825	825
Equivalence ratio	0.35 (constant)	*0.152 - 0.299*	*0.152 - 0.300*
Combustion efficiency	0.999	0.999	0.999
$EINO_x$	21.00	6.44	5.58
NO/NO_x	0.99	1.00	1.00
EIS	0.50	2.06	0.01
SO_3/SOx	0.06	0	0

Table 3.2.1. Summary of run conditions

1-D calculations were carried out after the CFD calculations of the NGV and rotor stages of the HPT1. Multiple streamlines were used to capture the non-uniformity at the rotor exit (Chapter II). For each sulfur level, two sets of calculations were performed – with air dilution and without air dilution. The air dilution here corresponds to the mixing of the core air with the bypass air. In the QinetiQ TRACE engine, there is a forced mixer aft of the turbine stage so there will be some air dilution. However, it is not known the extent of dilution and mixing at the location of the measurement probes. Thus, two cases were run to establish upper and lower bounds for the possible outcomes of species concentrations.

3.2.3. Modeling Results

For the pre-test runs discussed in [3], it has been observed that both SO_3 and HONO generally increase from combustor exit to nozzle exit. Increase in power level will increase the conversion to SO_3 and HONO. Combustor exit non-uniformity in temperature, unsteady rotor-NGV interaction, and local non-uniformities such as blade cooling, all have observable impacts on the evolution of trace species. In the sections below, results for temperature, pressure, SO_x, NO_y, and CO_x will be discussed in detail. Since the evolution of the species of interest is very similar between the two sulfur level cases, only the plots obtained for high sulfur cases will be shown below. For plots with both sulfur levels, please refer to Appendix A.

I. Temperature and Pressure

Temperature and pressure are important because they are among the major drivers for species evolution. Static temperature distribution across the NGV and rotor is shown at *Figure 3.2.4.*

At the rotor exit, decreases in temperature due to flow acceleration and work extraction are observed over most circumferential locations, with more significant decreases in the wakes of the blades due to blade cooling. The temperature profile is slightly shifted across the NGV. Across the rotor stage, however, because of the unsteadiness of the rotor, the temperature profile at the NGV exit is significantly modified. In addition, rotor blade cooling further modifies the rotor exit temperature profile. Note that *Figure 3.2.4* shows the temperature distribution across the rotor only at one instant. The temperature distribution across the rotor stage evolves continuously in the simulation due to the rotating rotors. The evolution of temperature is similar for both sulfur cases, a difference of around 20 – 70 K is observed, mainly due to the inlet condition.

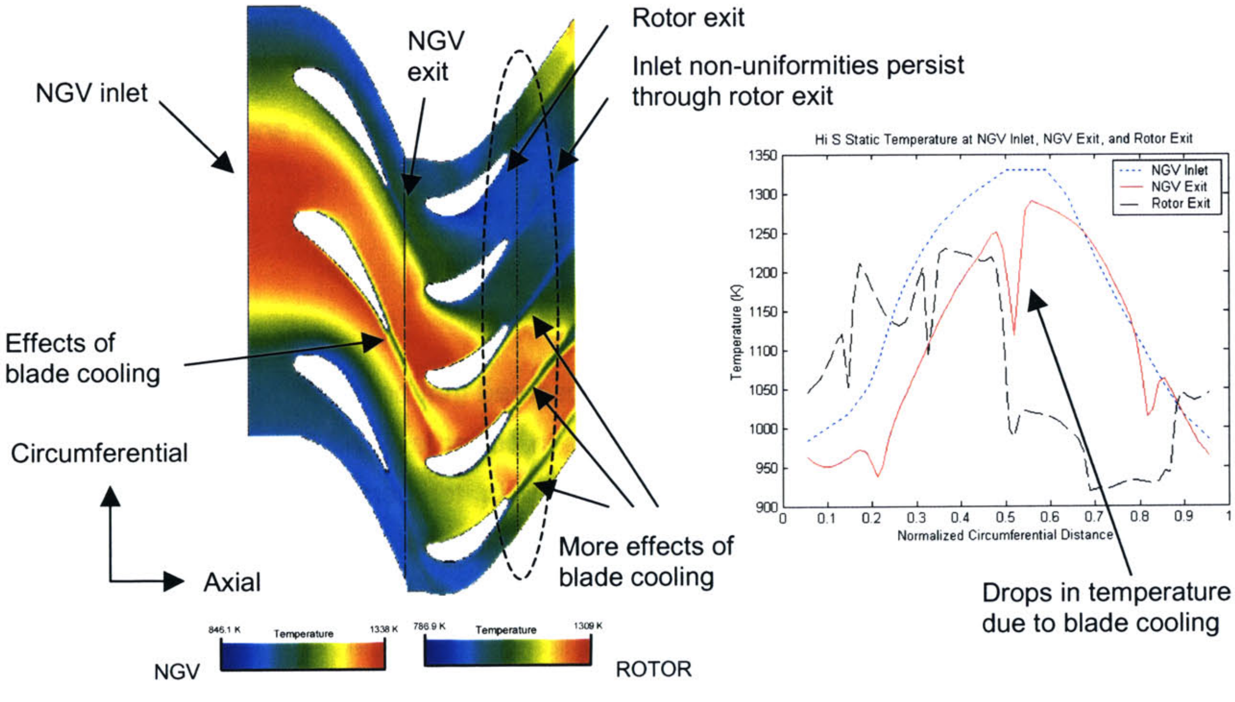

Figure 3.2.4. Static temperature profile for high sulfur run

For SO_3, NO_2, and HONO, temperature is one of the most important influences on species production. In the wakes (immediately downstream of the blades), the species exhibit higher productions mainly because of two reasons:

- Local blade cooling in high temperature and high pressure regions (please refer to the severity parameter plot in *Figure 2.1.1*).
- Lower velocity in the wake allows longer residence time for reactions.

As the species move downstream, the production rates for SO_3 and NO_2 decrease because of reductions in temperature through the post-combustor flow path. CO production is minimal throughout the rest of the engine. Conversely, HONO continues to react from the HPT1 through the LPT and nozzle, reflecting the greatest change of any oxidation product. This is due to the lower sensitivity to temperature and pressure for HONO over the operational space. However, this does not call for a CFD simulation from HPT1 to engine exit since local non-uniformities are less significant after the HPT1.

Pressure also has important effect for species reactions. However, unlike temperature, it does not have a non-uniform profile at the NGV inlet. The pressure profile for high sulfur case is shown at *Figure 3.2.5*.

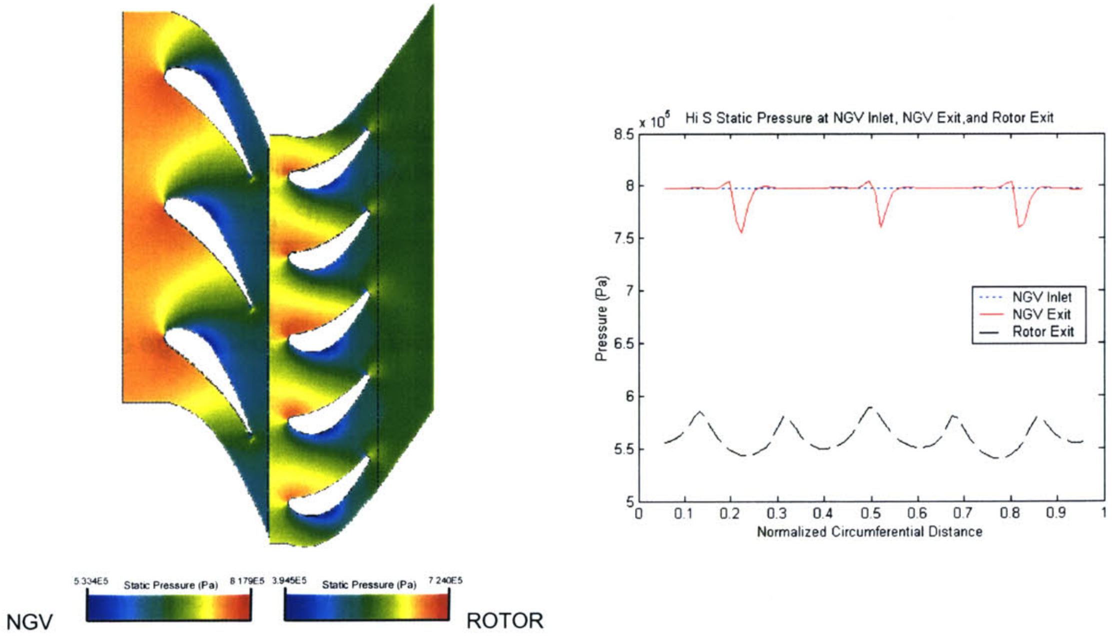

Figure 3.2.5. Static pressure profile for high sulfur run

The colors in the figure do not exactly match between NGV and rotor because both cases are run separately and they are scaled slightly differently. From the profile plot on the right, it can be seen that the only pressure drop across the NGV stage is because of the wake from the blades. While going from NGV exit to rotor exit, there is a more significant overall pressure drop because of extraction of work. The effect on pressure is slightly different from that across the NGV, the influence from the wakes is not as significant as before, but the pressure variation moving from pressure side to suction side of the blades is observed.

The 1-D variation of temperature and pressure from combustor exit to nozzle exit is shown in *Figure 3.2.6.* Continuous drop in temperature and pressure are observed through-out the flow path with the most significant drop in the turbine stage.

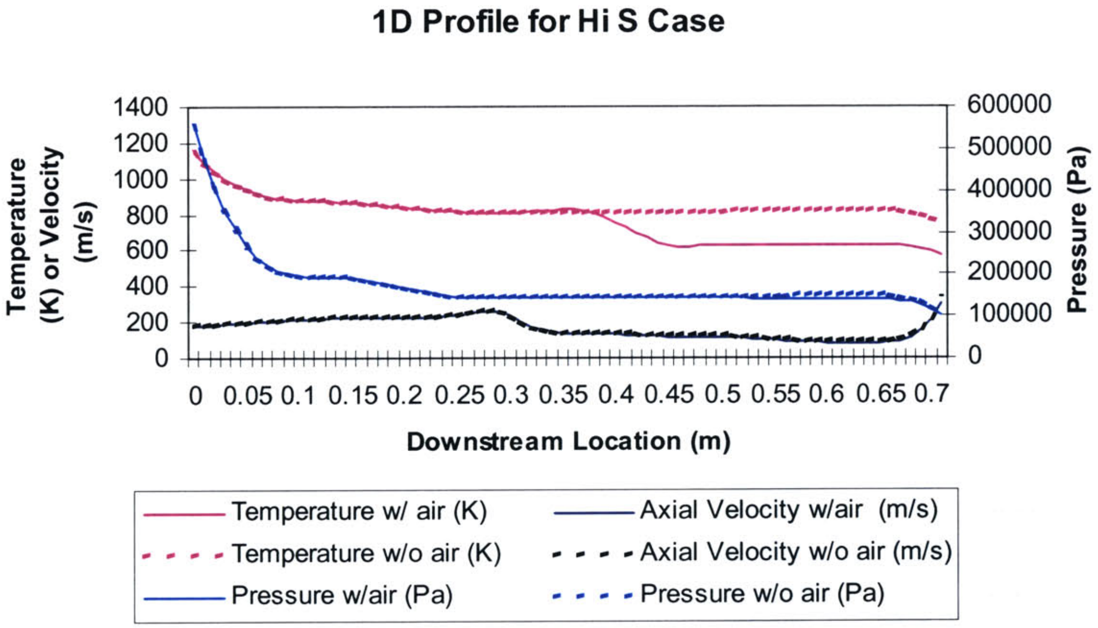

Figure 3.2.6. Mean temperature, pressure, and velocity profiles from second stage of HPT to nozzle exit

II. Sulfur Species – SO_3, H_2SO_4

SO_3 and H_2SO_4 are of special interest in our investigation because SO_3 is a precursor of H_2SO_4 and H_2SO_4 is a key component leading to formation of volatile particles which may affect contrails and cirrus cloud formation. Aviation fuels (kerosene) contain sulfur in trace amounts. In the current world market, the sulfur content – hence EI S – of aviation fuels is near 0.4 g S/kg fuel or 400 ppmm, with an upper limit specification of 3 g S/kg fuel [1]. Inside the combustor, almost all the fuel sulfur is converted to SO_2. As the flow moves further through the engine, SO_2 evolves into SO_3 in a manner that is well-described by the following reduced mechanism [4]:

$$SO_2 + O + M \leftrightarrow SO_3 + M$$
$$SO_3 + O \leftrightarrow SO_2 + O_2$$
$$SO_2 + OH \leftrightarrow SO_3 + H$$
$$SO_2 + OH + M \leftrightarrow HOSO_2 + M$$
$$HOSO_2 + O_2 \leftrightarrow SO_3 + HO_2$$

Once SO_3 is formed, the gas-phase reaction with emitted H_2O (a combustion product) to form H_2SO_4 is fast (< 0.1 s) under engine exhaust conditions [1]. As the exhaust leaves the engine nozzle exit and starts to cool down and mix with the ambient atmosphere, volatile liquid H_2SO_4/H_2O droplets are formed by binary homogeneous nucleation. These particles grow further by condensation and coagulation and become sites to form ice particles. If H_2O saturation is reached, a contrail forms. If the air is ice-saturated, the contrail will persist and may develop into a cirrus cloud [1]. As mentioned in Chapter I, cirrus clouds, which are thin clouds, will lead to global warming. This explains why the formation of SO_3 and H_2SO_4 are of special interest in this investigation.

Figure 3.2.7 shows the distribution of SO_3 across the NGV and rotor for the HPT1. From the circumferential profile, it can be seen that the initial SO_3/SO_x ratio at NGV inlet is up to 0.02%, with less oxidation (~0%) at the higher temperature locations. Although the SO_3/SO_x ratio is set to 0 initially, as discussed in Chapter II, the non-zero values arise as a result of the short-time-period 1-D kinetics calculation conducted to remove inconsistencies in the estimated combustor exit specification. The purpose of the 1-D kinetics calculation is to prevent possible oscillations in the CFD calculation by obtaining quasi-equilibrium of the species in the flow. Note that the maximum SO_3/SO_x ratio of 0.02% at the NGV inlet corresponds to less than 10% of the total oxidation through the post-combustor flow path. Thus, its difference from zero is acceptable. The circumferential profile for H_2SO_4 is shown at *Figure 3.2.8*.

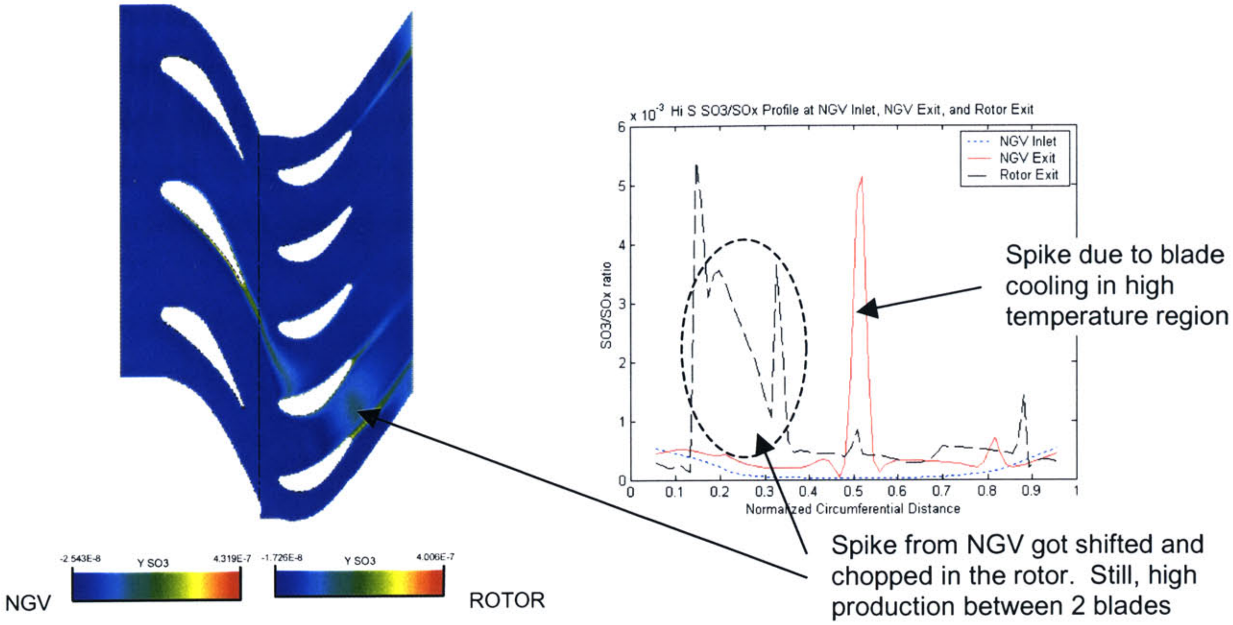

Spike due to blade cooling in high temperature region

Spike from NGV got shifted and chopped in the rotor. Still, high production between 2 blades

Figure 3.2.7. SO_3 profile for high sulfur run

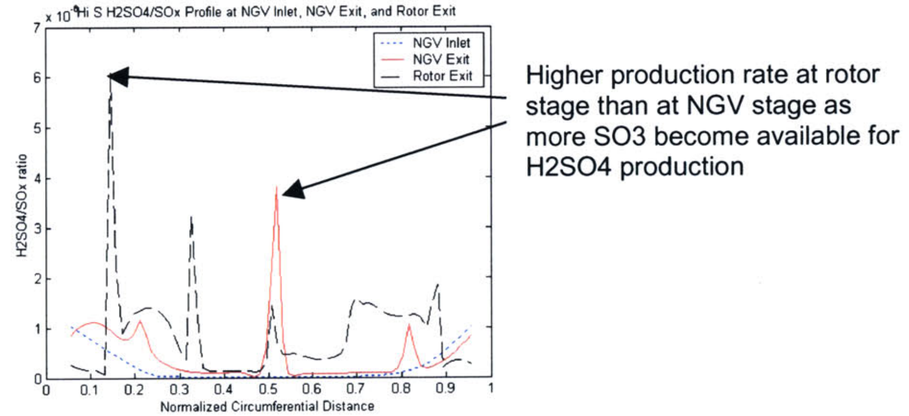

Higher production rate at rotor stage than at NGV stage as more SO3 become available for H2SO4 production

Figure 3.2.8. H_2SO_4 profile for high sulfur run

For both SO_3 and H_2SO_4, blade cooling in high temperature regions is a major production site as can be seen in the middle of the NGV exit. The high local concentration is carried into the unsteady rotor stage and is chopped by a rotor blade. This leads to relatively high production between the two blades in a high temperature region (this effect is not as significant for H_2SO_4). For H_2SO_4, blade cooling is still the dominant effect on production and the rate increases in the rotor stage because more SO_3 becomes available.

After going through the HPT1 stage with CFD calculations, 1-D calculations were carried out from the HPT1 exit to the nozzle exit. *Table 3.2.2* summarizes the results by location over the post combustor flow path for both SO_3, and its hydrolysis product H_2SO_4. Across the HPT1, the low sulfur case shows an approximately factor-of-four increase in SO_3 and a factor-of-two increase in H_2SO_4. Comparatively, for the high sulfur case, SO_3 has an order of magnitude increase across the HPT1 while H_2SO_4 increases by a factor-of-three. It seems to show that for high sulfur case, the production rates of SO_3 and H_2SO_4 are slightly higher, as further confirmed by considering the $(SO_3 + H_2SO_4)/SO_x$ ratio.

After the HPT1, the formation of H_2SO_4 is favored compared to SO_3 as H_2SO_4 increases by two to three orders of magnitude while SO_3 increases by an order of magnitude reaching a maximum at the nozzle exit. This is due to the fact that more and more H_2SO_4 is formed by reaction of SO_3 with water while the rate of transformation of SO_2 to SO_3 is diminishing. The presence of air addition leads to an order of magnitude enhancement in formation of H_2SO_4.

		Combustor Exit	HPT1 NGV Exit	HPT1 Rotor Exit	Nozzle Exit (w/air addition)	Nozzle Exit (no air addition)
Lo S	SO_3 (ppbv)	0.00917	0.0197	0.036	0.226 (0.013 - 0.572)	0.340 (0.045 – 1.21)
	H_2SO_4 (ppbv)	0.000011	0.000016	0.000027	0.0589 (0.0134 - 0.299)	0.00549 (0.00117 - 0.0208)
	$(SO_3 + H_2SO_4)/SOx$	0.016%	0.032%	0.058%	0.85%	0.55%
	OH (ppmv)	1.79	2.34	2.28	0.14 (0.0 - 0.50)	0.26 (0.0 - 0.93)
	O (ppbv)	25.3	47.7	57.5	18.7 (0.075 – 74.4)	19.6 (0.130 – 81.2)
Hi S	SO_3 (ppbv)	1.62	5.38	11.3	53.4 (3.05 – 124)	68.1 (10.6 – 229)
	H_2SO_4 (ppbv)	0.00193	0.0035	0.00676	9.69 (3.03 – 46.3)	0.724 (0.145 – 2.77)
	$(SO_3 + H_2SO_4)/SOx$	0.013%	0.042%	0.088%	0.89%	0.52%
	OH (ppmv)	2.29	3.02	2.98	0.15 (0.0 - 0.56)	0.35 (0.0 – 1.27)
	O (ppbv)	35.3	60.2	72.9	19.4 (0.082 – 74.9)	21.0 (0.156 – 81.2)

Table 3.2.2. SO_3 and H_2SO_4 evolution through the post-combustor flow path

As a modeling assessment exercise, it would be desirable to have measurements of SO_3 and H_2SO_4 at both combustor exit and nozzle exit for comparison. Measurements of SO_3 were attempted but were unsuccessful as briefly described in a previous section. Thus, direct assessment of SO_3 modeling accuracy was not possible but the conversion trends obtained above agree with expectations.

If H_2SO_4 is indeed the specie that we want to minimize for environmental concern, other than minimizing the fuel sulfur content, formation of SO_3 must be reduced. All the SO_3 leaving the engine converts to H_2SO_4 eventually.

III. Nitrogen Species – NO_2, HONO

Nitrogen is a major component in air. As air and fuel mix and burn in the combustor of an aircraft engine, some of the nitrogen forms nitrogen oxides under the high temperature and pressure. Typically, NO will be formed first and then later converted into NO_2, HONO, etc. As described in Chapter I, nitrogen oxides have various effects on ozone destruction and production. Also, HONO may impact the chemical proportions of the exhaust plume aerosol particles that contribute to contrail formation.

It has been found that nitrogen oxides are mostly formed as NO in the combustor. From combustor exit to nozzle exit, the total amount of nitrogen oxides remains fairly constant, only the composition is changed, i.e. %NO vs. %NO_2 vs. %HONO, etc. Therefore, in this investigation, EI NO_x was set to be constant and the focus was on evaluating the changes of NO_x composition. From [4], NO_2 is produced mainly via the following reactions:

$$NO + O + M \leftrightarrow NO_2 + M$$

$$NO_2 + O \leftrightarrow NO + O_2$$

$$NO_2 + H \leftrightarrow NO + OH$$

$$NO + HO_2 \leftrightarrow NO_2 + OH$$

And HONO is produced mainly via the following reactions:

$$HONO + OH \leftrightarrow NO_2 + H_2O$$

$$NO + OH + M \leftrightarrow HONO + M$$

$$HONO + O \leftrightarrow OH + NO_2$$

Note that there are both production and destruction reactions at the same time, and they have a strong dependence on temperature, pressure, and availability of H, O, and OH. Therefore it is hard to determine solely by looking at the reactions whether there will be production or destruction of NO_2 or HONO. This highlights the importance of having detailed modeling calculations.

The distribution of NO_2 across the HPT1 stage for the high sulfur case is shown at *Figure 3.2.9.* As in the case of SO_3, the higher residence times and lower temperatures of the cool wake and boundary layers from the blades have a strong impact on NO_2 production on blade surfaces and downstream of the blades. This effect can be seen as the spikes on the circumferential profile plot. However, in addition to the above effect, there is also a significant amount of conversion of NO to NO_2 beside the center blade of the NGV stage as well. Comparing with the temperature plot in *Figure 3.2.4*, it can be seen that this region corresponds to the high temperature region from the combustor exit. Therefore, for NO_2, in addition to the blade cooling effect under high temperature, high temperature in the free-stream is also a major area for NO_2 production.

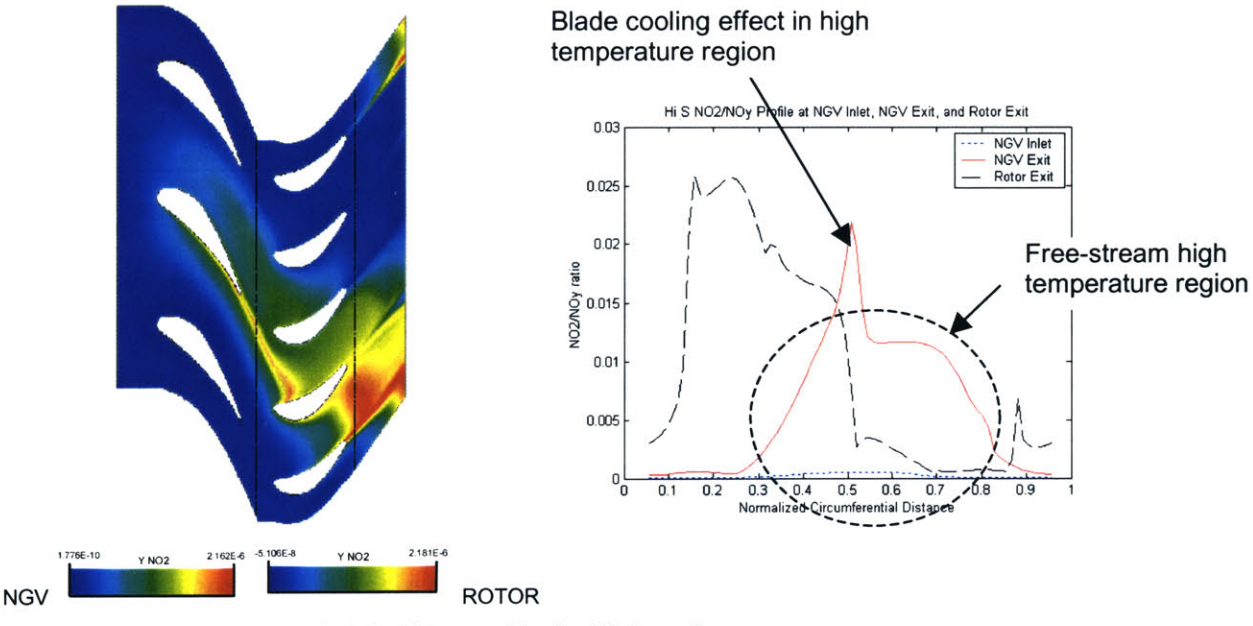
Blade cooling effect in high temperature region

Free-stream high temperature region

Figure 3.2.9. NO_2 profile for high sulfur run

Table 3.2.3 shows the results of NO_2 and HONO by location over the post-combustor flow path, along with measurements of NO_2 from QinetiQ and measurements of HONO from Aerodyne Research, Inc. When comparing the changes in mass-averaged concentrations among the species, NO_2 has the greatest increase in terms of percentage for both high and low sulfur cases with an approximately 100-fold gain through the post-combustor flow path. However, considering the ratio of NO_2 to NO_y, the amount of NO_2 present is still very small relative to NO (NO_2/NO_y ~2.3%, with the rest of NO_y mostly composed of NO).

For the high sulfur case, where EI NO_x, temperature, and pressure are higher, the levels of NO_2 through the HPT1 are expectedly higher. The fuel sulfur level should not be a factor since SO_2 is oxidized primarily through OH while NO_2 is produced primarily through O (as shown in the reduced mechanisms above).

		Combustor Exit	HPT1 NGV Exit	HPT1 Rotor Exit	Nozzle Exit (w/air addition)	Nozzle Exit (no air addition)	Measured (ARI HONO QinetiQ NO_2
Lo S	NO_2 (ppbv)	4.92	170	279	534 (12.9 – 1490)	1080 (25.2 – 2990)	2000
	NO_2/NOy	0.010%	0.33%	0.54%	1.9%	2.1%	
	O (ppbv)	25.3	47.7	57.5	18.7 (0.075 – 74.4)	19.6 (0.130 – 81.2)	
	HONO (ppbv)	8.30	29.6	62.9	540 (28.3 – 1500)	987 (53.0 – 2720)	674 ± 16
	HONO/NOy	0.017%	0.058%	0.12%	1.9%	1.9%	1.4%
	OH (ppmv)	1.79	2.34	2.28	0.14 (0.0 - 0.50)	0.26 (0.0 - 0.93)	
Hi S	NO_2 (ppbv)	7.21	274	433	845 (27.3 – 2030)	1620 (51.6 – 3860)	2670
	NO_2/NOy	0.013%	0.46%	0.73%	2.6%	2.7%	
	O (ppbv)	35.3	60.2	72.9	19.4 (0.082 – 74.9)	21.0 (0.016 – 81.2)	
	HONO (ppbv)	12.2	37.8	78.4	750 (46.7 – 1790)	1310 (85.5 – 3160)	400 ± 80
	HONO/NOy	0.022%	0.064%	0.13%	2.3%	2.1%	1.5%
	OH (ppmv)	2.29	3.02	2.98	0.15 (0.0 - 0.56)	0.35 (0.0 – 1.27)	

Table 3.2.3. NO_2 and HONO evolution through the post-combustor flow path

As part of the assessment exercise, the results obtained from modeling at the nozzle exit were compared with the NO_2 measurements obtained by QinetiQ. The averaged modeling results both with and without air dilution cases are lower than measurement results. The reason for this is because of the initial conditions set for the simulation as summarized in *Table 3.2.1*. For NO_x, the NO/NO_y ratio was set to 1 at the combustor exit, i.e. all the NO_x species coming out from the combustor were NO only. However, this is not the case as measurements taken by QinetiQ indicate an average NO_2/NO_y ratio of 0.03 at the combustor exit. It has been explained previously why the NO/NO_y ratio of 1 was used. Therefore, in the real scenario, some NO_2 would have come out directly from the combustor with a higher equilibrium level. This may help to explain the difference between the measured and calculated level of NO_2 at the engine nozzle exit.

For HONO, its distribution and profile across the NGV and rotor for the HPT1 stage is shown in *Figure 3.2.10*. The production of HONO is dominated by cooled wake in the high temperature region, especially in the rotor stage. Unlike NO_2, there is minimal effect on HONO production due to the high temperature in the free-stream. The results for HONO at different locations downstream of the combustor exit are shown at *Table 3.2.3*. It has been shown in [4] that HONO tends to be produced later in the post-combustor flow path. More HONO will be produced due to the availability of both NO and extra NO_2 produced earlier in the stage.

Comparing the HONO measurements obtained by Aerodyne Research, Inc., with a mass average from the simulations, it is found that the simulations match test data to within about a factor of 3 for absolute HONO concentrations for the high sulfur case and to within ~45% for the low sulfur case. Associated trends in HONO with sulfur level (increasing amount of HONO with higher EI S) do not match measurement data, where the data show a decrease in HONO level with higher sulfur level. However, both the results from the simulation and measurements agree within the ranges from the different streamlines in the simulations and errors from the experiments. It is not possible to conclude at this stage whether either trend observed is generally representative of the engine flow path behavior.

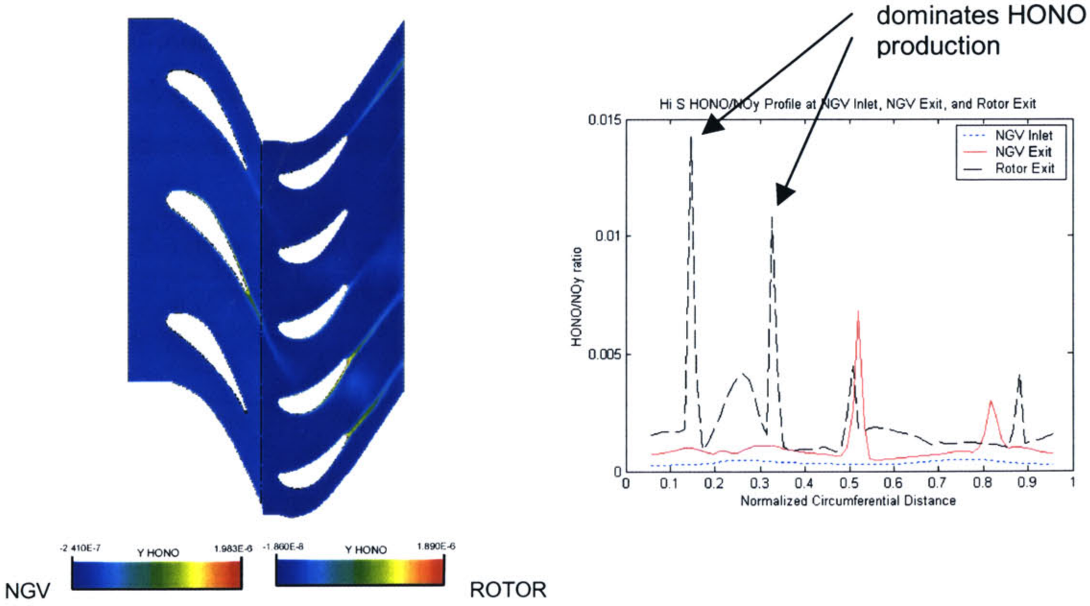

Figure 3.2.10. HONO profile for high sulfur run

IV. Carbon Monoxide (CO)

It has been mentioned in Chapter I that CO_2 as a greenhouse gas creates direct radiative forcing to the atmosphere hence global warming. Since the CO_x family is mainly composed of CO and CO_2, looking at either species will show how they evolve in the post-combustor flow path. CO is produced as part of the inefficient combustion process. In current engines, combustors achieve efficiency of 99% or above. This reduces CO production significantly. However, the amount of CO_x remains as the carbon comes directly from the fuel being burnt. The reduced reaction mechanism for CO is obtained from [4]:

$$CO + OH \leftrightarrow CO_2 + H$$

$$CO + O_2 \leftrightarrow CO_2 + O$$

$$CO + O + M \leftrightarrow CO_2 + M$$

The evolution of CO in the post-combustor flow path is shown at *Figure 3.2.11*. Minimal change is observed. There are slight decreases in CO downstream of cooled wakes. The amounts obtained from both simulations and measurements by QinetiQ are shown at *Table 3.2.4*. From the simulation, a constant amount of 62 – 68 ppmv of CO is obtained from combustor exit to nozzle exit. For the measurement data, only 20 – 30 ppmv is obtained. However, from the QinetiQ/NASA combustor report [12], CO ranges from 20 ppmv to 106 ppmv, with an average of ~ 75 ppmv, which agrees with the simulation. The difference between the simulation and measurement data is likely to be due to the combustion efficiency being assumed in the initial condition as the exact efficiency profile at the combustor exit was not available.

		Combustor Exit	HPT1 NGV Exit	HPT1 Rotor Exit	Nozzle Exit (w/air addition)	Nozzle Exit (no air addition)	Measured (QinetiQ)
Lo S	CO (ppmv)	65.4	67.2	68.1	36.4 (26.5 – 45.5)	67.8 (49.2 – 84.0)	30
	CO/CO_x	0.33%	0.33%	0.33%	0.33%	0.33%	
	OH (ppmv)	1.79	2.34	2.28	0.14 (0.0 - 0.50)	0.26 (0.0 - 0.93)	
Hi S	CO (ppmv)	65.4	67.5	67.5	36.9 (26.7 – 44.7)	68.0 (49.1 – 81.8)	19.16
	CO/CO_x	0.33%	0.33%	0.33%	0.32%	0.32%	
	OH (ppmv)	2.29	3.02	2.98	0.15 (0.0 - 0.56)	0.35 (0.0 – 1.27)	

Table 3.2.4. CO evolution through the post-combustor flow path

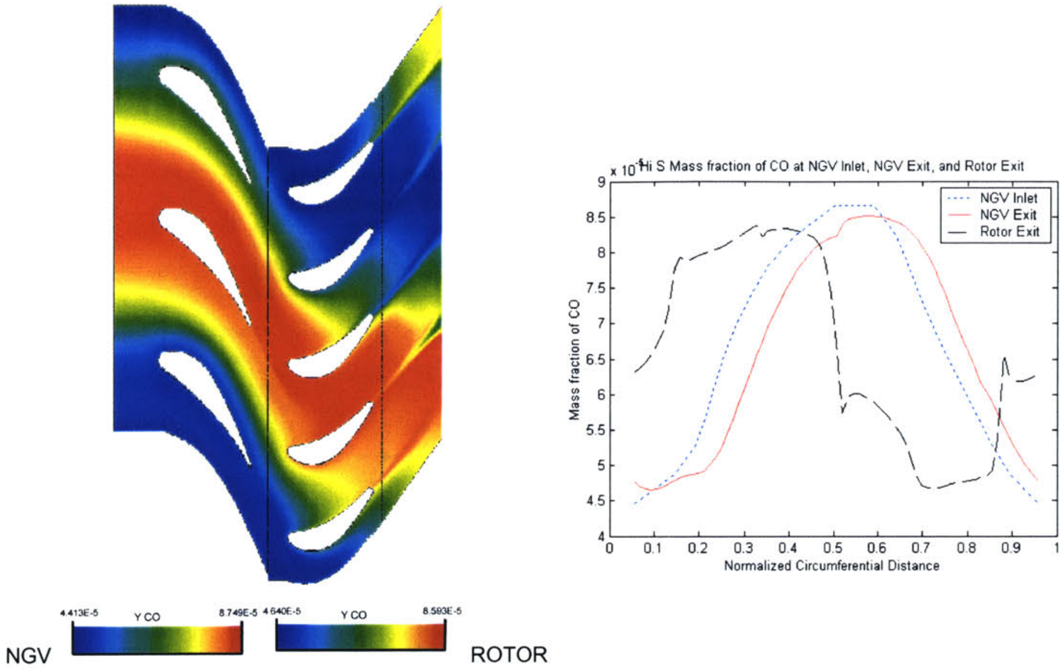

Figure 3.2.11. CO profile for high sulfur run

V. Assessment Summary

The modeling methodology to simulate the evolution of trace species in the post-combustor flow path agrees with the measurement data within an order of magnitude. The agreement is considered reasonable based on the uncertainties, measurement errors, and limited amount of data available to specify a precise initial condition. The comparison is shown at *Figure 3.2.12.* Note that only the case without air dilution is included in the plot. The comparison for the case with air dilution is included in Appendix A, the results are very similar to the one without air dilution.

Since sulfur species were not measured in the engine test, only NO_x species are involved in the comparison. Results of NO_2 are presented implicitly by looking at the difference between NO_x and NO. For both no air dilution and with air dilution, all the averaged measured values lie within the range obtained through simulation except EI NO_x for the high sulfur case. The EI NO_x ranges obtained through simulation do lie within the error range of EI NO_x measurements however. The averaged nozzle exit results for NO_2 are lower than measurement results. This is because simulation initial conditions were set to a concentration of zero for NO_2 whereas some

NO_2 would be expected to be formed in the combustor, as described above. Measurements taken by QinetiQ in the combustor test indicate an average NO_2/NO_y ratio of 3% at combustor exit, which corresponds to a small but finite amount of NO_2 present at the combustor exit.

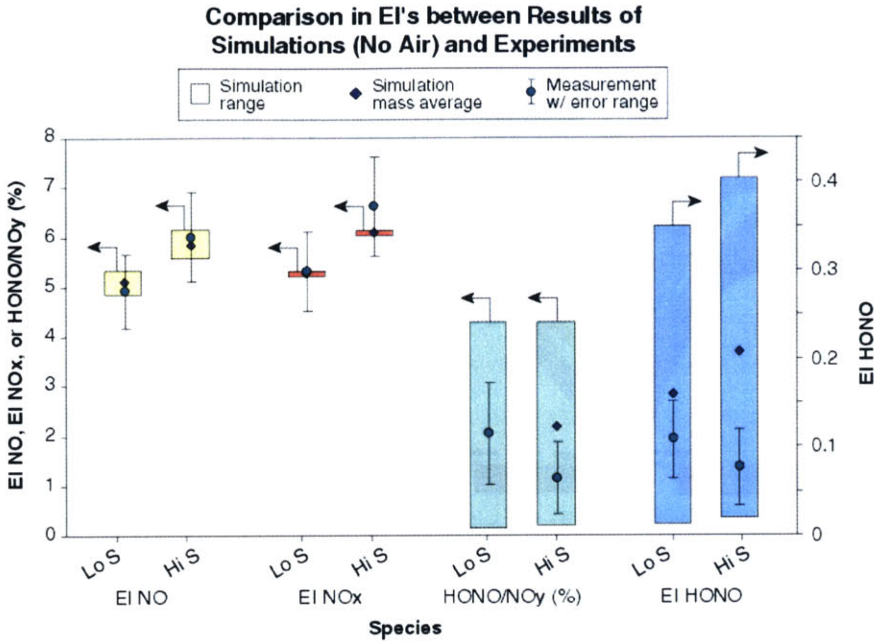

Figure 3.2.12. Comparison between results of simulations (no air dilution) and experiments

For HONO, mass averaged results from simulations conducted match test data to within ~45% for absolute HONO concentrations for the low sulfur case and to within a factor of ~3 for the high sulfur case. The HONO measurements fall well within the range of calculated exit concentrations. Associated trends in HONO with sulfur level (increasing amount of HONO with higher EI S) do not match the trends from measurements. However, it is not feasible to draw a definite conclusion regarding the modeling accuracy because of the uncertainties present in the measured data.

For other species, the simulation showed that both SO_3 and H_2SO_4 production increases with fuel sulfur level. The oxidation of SO_2 to SO_3 and H_2SO_4 as a percentage is approximately the same for both sulfur levels while the total SO_x oxidized is two orders of magnitude higher for the high sulfur case (with EI S for high sulfur case also two orders of magnitude higher, 2060 ppmm vs. < 10 ppmm).

The effect of different power settings was not investigated due to the minimal difference in power setting used in the engine tests. Results obtained were found to be quite sensitive to the initial H_2 setting, and interestingly, seeding the flow with H_2 may reduce SO_3, HONO, and NO_2 formation through the turbine exhaust nozzle. Comparison with the NO_2, HONO, and CO measurements provided an initial, but partial assessment. However, the assessment indicates that the current modeling methodology can accurately estimate these species to within an order of magnitude. To improve the accuracy of the model, a detailed and accurate initial condition profile is desired.

IV. Incorporation of Mass Addition Capability into CNEWT

In all the CFD calculations done using CNEWT in previous chapters, the blade cooling effect was simulated by setting a wall temperature on the blade surface. No cooling air was injected. However, in the actual scenario, cooling air, usually bled from the high pressure compressor stage, is injected in a wide variety of ways to keep the blade below its melting temperature. The injection of cooling air, is believed to have the following effects on the local evolution of trace chemistry:

- Local temperature non-uniformity – a high local temperature gradient between the cooling mass and the ambient while having similar flow time scale provides regions where certain reactions become more favorable.

- Species dilution – the addition of the cooling mass increases the total mass flow producing a dilution effect on the existing species in the flow.

- Extra chemical production – the cooling air is composed of different composition of species than the ambient flow. Addition of these species may lead to different results from the chemical reactions for species production. For example, oxygen (O_2) may produce extra atomic O, which is crucial to many reactions.

The above three effects are considered important when mass is being added in the calculation. More effects may become important when the amount of injection mass is large and depending on the method by which mass is added.

4.1. Mass Addition Methods

In current aircraft gas turbine engines, the blades, both NGV and rotor, in the high pressure turbine stage are cooled. The cooling is done not only on the blade surface, but on the endwalls as well. Regarding how they are cooled, it could be via internal cooling or external cooling. For internal cooling, no mass is injected, the blades are cooled by having cool air running inside the blade such that the heat on the blade surface will be conducted away. For external cooling, cool air is injected through holes or slots on the blade surface (*Figure 4.1.1*). The injected air will then form a cool air layer on the blade shielding the wall surface from the ambient high temperature. Air injected in this manner can account for as much as 25% of the flow through the core of the engine.

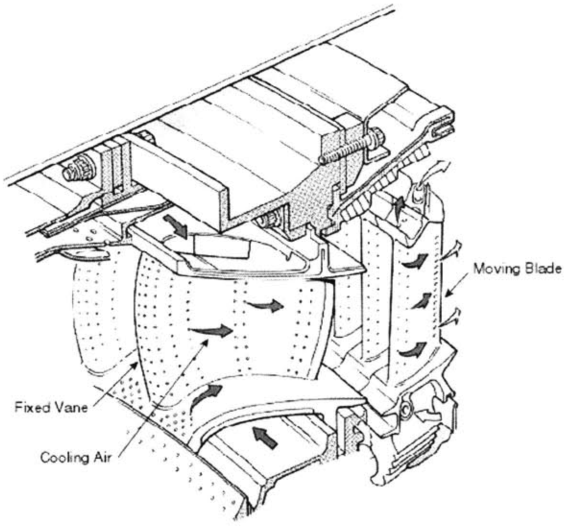

Figure 4.1.1. Illustration of cooling schemes in a typical turbine stage [17]

In the modeling methodology, as described in Chapter III, CFD is used to perform the calculations on the NGV and rotor in the HPT1. Since the goal is to investigate the effects of mass addition on the evolution of chemistry, it was thus necessary to add the capability to simulate mass addition to CNEWT. Two strategies were investigated to incorporate the mass addition capability into the code:

- Changing the grid to include cooling holes or cooling slots (*Figure 4.1.2*) – in this case, the way mass is injected would be simulated in a physically-realistic manner. Furthermore, the existing multiple inlet/exit capability in the code should make this implementation relatively easy. However, the grid generation tool associated with CNEWT is relatively complicated to use. Thus inclusion of cooling holes into the existing grid would be very difficult. Also, the existing grid only consists of a thin slice at mid-span of the blade, which makes it even more unsuitable to use this method. A relatively dense grid may be required to capture accurately the injection jets individually. The other disadvantage related to this method is that all the grids must be made specific for the mass addition purpose.

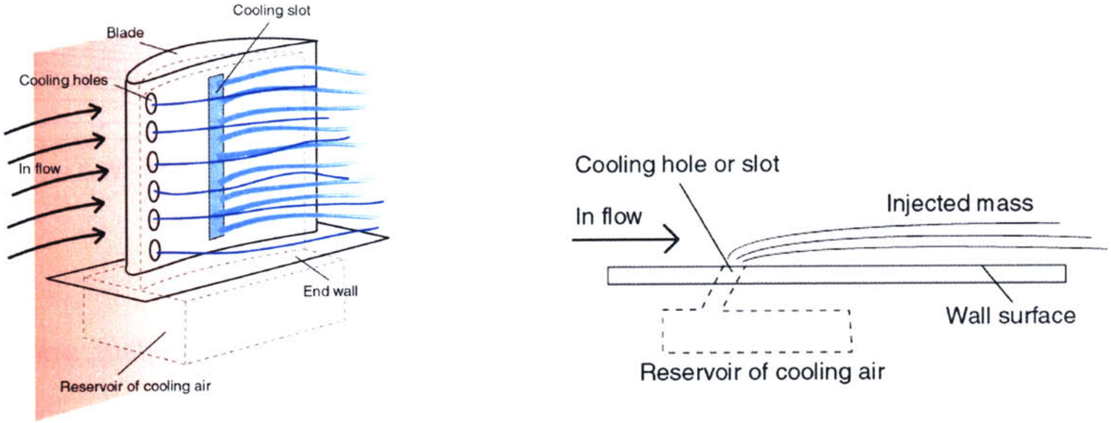
Cooling slot
Blade
Cooling holes
In flow
End wall
Reservoir of cooling air
Cooling hole or slot
In flow
Injected mass
Wall surface
Reservoir of cooling air

Figure 4.1.2. Sketch of mass addition through cooling holes and slots on a blade surface (left), side view of mass injection on a flat surface (right)

- Addition of mass through transpiration (*Figure 4.1.3*) – transpiration allows mass to be added through the whole surface. It is equivalent to having the wall surface made of a mesh-like material with mass being added over the whole surface. Due to a larger surface for mass addition, the mass will be injected at a lower velocity. The advantage of this method is that almost any surface in the existing grid can be used as a transpiration surface, i.e. the grid doesn't need to be specific for the mass addition investigation. With the low injection velocity, it should produce minimal disturbance to the background flow. The only disadvantage would be the fact that it does not capture the method of mass injection typically employed in actual blades. However, transpiration cooling allows a general study of how mass addition affects the species chemistry regardless of injection configuration.

In the modeling methodology, mass addition capability was implemented into CNEWT as transpiration cooling.

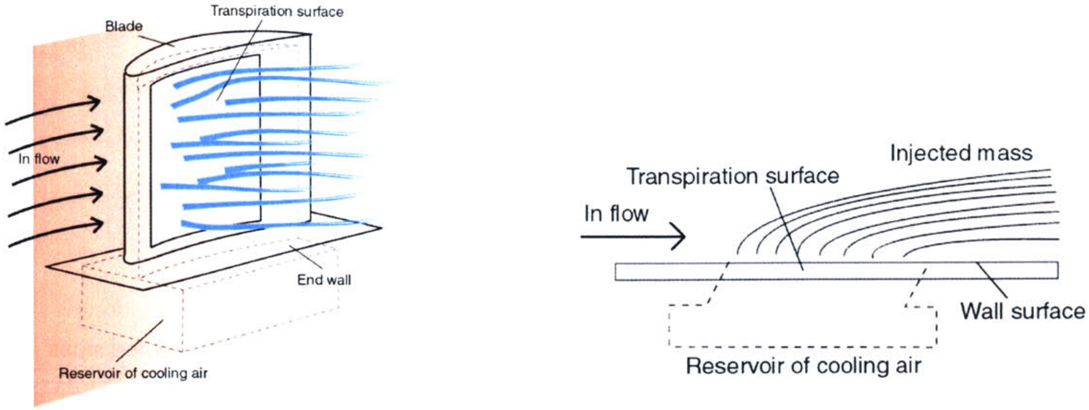

Figure 4.1.3. Sketch of mass addition through transpiration on a blade surface (left), side view of transpiration cooling on a flat surface (right)

4.2. Boundary Conditions on Solid Surfaces in CNEWT

Before discussing the modifications to the CNEWT code, first it is necessary to understand the boundary condition treatment on solid surfaces. There are three major surfaces types that can be specified in CNEWT: inlet, outlet, and solid surface. For the mass addition case, one more surface type – *transpiration surface*, was added. The transpiration surface is a combination of a solid surface and an inlet. When no mass is being added, the transpiration surface has the property of a solid surface. When mass is being added, it acts like a permeable wall to allow mass to be added.

Originally, it was proposed that the mass addition through transpiration could be carried out by adding source terms to the continuity, momentum, and energy equations. However, it was found to be not applicable for this code. In CNEWT, special treatment is utilized on solid surfaces (as described in a subsequent section below). Wall functions are used in the momentum and energy equations as well as in the turbulence model. Their presence complicates the calculation on solid surfaces as the results calculated on the wall surface will be different from some basic assumptions, e.g. no-slip condition is no longer enforced. Therefore, if source terms are added to achieve the mass addition effect, it would be hard to get the exact conditions of the injection mass desired. Thus it was decided that the mass addition would be carried out through settings in boundary conditions.

In the calculation, zero normal fluxes of mass, momentum, and energy are imposed on a wall surface. Also, a no-slip condition (zero velocity on the surface), is usually enforced unless an completely inviscid case is specified. This boundary condition is further complicated by the presence of a boundary layer on wall surface and the presence of turbulence. Inside an aircraft gas turbine engine, the Reynolds number is usually very high such that the flow is turbulent. At the same time, the boundary layer will be very thin as well (length scale of 1 mm or less). Thus in the numerical calculation, many grid points are required near the solid surface to accurately resolve the boundary layer. This increases the computational time significantly. Since it was not an objective to investigate the boundary layer flow, having a shorter computational time is of greater importance.

On solid surface boundaries, it is necessary to calculate the wall shear stress (τ_w) for the momentum equations. When a no-slip condition is enforced, the wall shear stress can be calculated by finding the velocity gradient on the wall with adjacent cells (Eq. 4.1.1).

$$\tau_w = \mu \left. \frac{du}{dy} \right|_w \tag{4.1.1}$$

Without special treatment, the no-slip condition alone can complete the calculation. However, if the grid is not dense enough near the wall surface, the resulting boundary layer obtained from the calculation will be much thicker than the actual boundary layer. In addition to the lack of accuracy regarding the boundary layer, this leads to inaccurate calculation of losses and blockages of the flow, as they are directly related to the boundary layer. To solve this problem without having to increase the density of the grid, the wall function approach is used in NEWT.

In NEWT, usage of a wall function is determined by the distance (y^+) between the wall and the adjacent node. The profile of a turbulent boundary profile is shown at *Figure 4.1.4.*

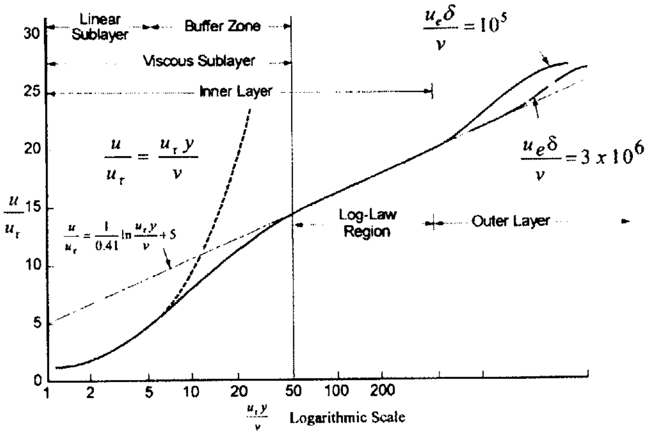

Figure 4.1.4. Regions of a turbulent boundary layer [18]

If y^+ calculated from the wall adjacent node is less than 10, i.e. the grid is dense enough, the wall function will not be used and the code will resolve the flow to the laminar sublayer of the turbulent boundary layer to calculate the wall shear stress. If y^+ is larger than 10, which is most likely to happen for coarser grids, the wall function is used. The basic idea is to make approximations to the flow equations near the wall. In NEWT, the log law is used (Eq. 4.1.2):

$$\frac{U}{u_\tau} = \frac{1}{\kappa}\log(Ey^+)$$
$$u_\tau = \sqrt{\frac{\tau_w}{\rho}}, y^+ = \frac{\rho u_\tau y}{\mu} \tag{4.1.2}$$

where U is the local fluid velocity, κ is the von Karman constant – 0.41, and E is set to force $U/u_\tau = 10$ at $y^+ = 10$ ([7], [14]). Note that when the wall function is used, the no-slip condition is no longer enforced. In other words, the velocity on the wall surface will not be zero. It is because the wall function tries to achieve the actual boundary layer thickness and the associated loss through having a corresponding velocity gradient on the wall surface, thus the velocity is not necessarily zero on the wall.

In addition to the momentum equation, the energy equation is affected by the special wall treatment as well. For the solid surface, it is optional to set it as an adiabatic wall or with a specific wall temperature. And similar to a velocity boundary layer, a thermal boundary layer also exists relating to the temperature gradient from the wall to the free-stream. When the wall is set to be adiabatic, there will be no heat flux (q_w) from the wall to the free-stream as the temperature will be the same. However, when a specific temperature is set on the wall, then there will be heat flux in/out of the wall depending on the wall temperature and the free-stream temperature. The special solid surface boundary treatment is also applied to the thermal boundary layer. When y^+ is less than 10, the heat flux is computed from the wall normal temperature gradient. When y^+ is bigger than 10, the heat flux is calculated from the wall function based on Reynolds analogy (Eq. 4.1.3) [7].

$$q_w = \rho u_\tau c_p (T - T_w) \tag{4.1.3}$$

Similar to the case with the velocity, the wall temperature will not be exactly the same as the one specified when the wall function is being used.

Other than the momentum and the energy equations, special treatment is also applied to the turbulence model. In NEWT, the κ-ε turbulence model is used. The model is valid only for fully turbulent flows (when Re is large). Close to solid walls, there will be regions where the local Reynolds number is so small that viscous effects pre-dominate over turbulent ones (within the boundary layer). To account for these regions in the calculation, a special wall function is also used in the turbulence model. It is used along with the wall function for the momentum equation and the energy equation described above to resolve the turbulent boundary layer. For more information about the κ-ε turbulence model and its wall function, please refer to [15], [16].

4.3. Effects of Wall Function on Surface Boundary Condition

To allow mass addition through transpiration in the code, a new boundary condition must be created. The difficulty is to combine the boundary treatment on an inlet and on a solid surface. Since 7 differential equations (continuity equation, momentum equations for 3 directions, energy equation, and κ, ε equations for the turbulence model) (Eq. 4.1.4, please refer to [7] for definitions of some coefficients) are being solved simultaneously in the code for the flow, 7 boundary conditions would be required for each boundary: density (ρ), velocities multiplied by density (ρV_X, ρV_T, ρV_R), energy multiplied by density (ρE), κ, and ε. In addition to the flow equations, inclusion of species also introduces the corresponding number of differential equations.

$$\frac{\partial}{\partial t}\oint_{VOL}\overline{U}\,dVOL=\oint\overline{H}\cdot dAREA+\oint_{VOL}\rho\overline{S}\,dVOL$$

$$\text{where}$$

$$\overline{U}=\begin{bmatrix}\rho\\ \rho V_X\\ \rho V_T\\ \rho V_R\\ \rho E\\ \rho\kappa\\ \rho\varepsilon\end{bmatrix}\qquad \overline{H}=\begin{bmatrix}\rho\overline{q}\\ \rho V_X\overline{q}+\overline{\overline{\sigma}}\hat{i}_X\\ \rho V_T\overline{q}+\overline{\overline{\sigma}}\hat{i}_T\\ \rho V_R\overline{q}+\overline{\overline{\sigma}}\hat{i}_R\\ \rho I\overline{q}+\overline{q}\cdot\overline{\overline{\sigma}}+\lambda\nabla T\\ \rho\kappa\overline{q}+(c_2\mu/\rho)\nabla\kappa\\ \rho\varepsilon\overline{q}+(c_3\mu/\rho)\nabla\varepsilon\end{bmatrix}\qquad \overline{S}=\begin{bmatrix}0\\ 0\\ T\Omega^2-2\Omega V_R\\ R\Omega^2+2\Omega V_T\\ 0\\ G-\rho\varepsilon\\ f_1\dfrac{c_4\varepsilon G}{\kappa}-f_2\dfrac{c_5\rho\varepsilon^2}{\kappa}\end{bmatrix} \tag{4.1.4}$$

At the inlet, the total temperature, total pressure, the flow angles, and the mass fractions of the species (Y_i) are specified by user. By assuming $\frac{\partial p}{\partial n}$ (where n is the normal to the surface) to be zero at the inlet, the static pressure can be found. Through isentropic relationships, static temperature can be found as well based on the input total temperature (Eq. 4.1.5). From the same relationship, the absolute velocity can be found with some manipulations (Eq. 4.1.6); along with the flow angles, the velocities in all three directions can be calculated. Density can be found from equation of state (Eq. 4.1.7).

$$T_{static}=T_0\left(\frac{P_{static}}{P_0}\right)^{\frac{\gamma-1}{\gamma}} \tag{4.1.5}$$

$$V_{absolute}=\sqrt{2C_p(T_0-T_{static})} \tag{4.1.6}$$

$$\rho=\frac{p_{static}}{C_p\left(\dfrac{\gamma-1}{\gamma}\right)\cdot T_{static}} \tag{4.1.7}$$

From temperature and velocities, the associated energy can be calculated at the boundary. $\frac{\partial \kappa}{\partial n} = 0, \frac{\partial \varepsilon}{\partial n} = 0$ are also utilized at the inlet boundary condition.

On solid walls, not all the 7 variables above are specified when the wall function is being used. When the wall function is not being called, however, a no-slip condition is enforced such that the velocities in all three directions are zero. Also, $\frac{\partial P}{\partial n}, \frac{\partial \varepsilon}{\partial n}, \frac{\partial Y_i}{\partial n}$, and κ are set to 0 on the wall. If the wall is non-adiabatic, a specific wall temperature will be set by user. If the wall is adiabatic, then $\frac{\partial T}{\partial n}$ will be set to 0. Again, density is calculated using the equation of state based on the settings of other variables above.

Before deciding the boundary condition settings for a transpiration surface, it is crucial to determine how the wall function will affect the transpiration surface. Details of this investigation are included in Appendix B. Removing the wall functions completely (in the momentum and energy equations as well as in the turbulence model) was chosen to be the way to include mass addition capability to the code after the investigation. Without refinements to the grid, the boundary layer being resolved will not be accurate. However, as mentioned previously, the focus is not on the absolute accuracy of the boundary layer nor with the associated losses. Thus it is acceptable to remove the wall function while keeping the grid density the same. To prevent any discontinuities mentioned above, the wall function was removed on the regular surface boundary condition as well.

4.4. Creation of Transpiration Surface Boundary Condition

Mass addition through a transpiration surface in the code was implemented by enforcing the necessary variables to the desired values on the transpiration surface boundary conditions. Seven boundary conditions are required for each boundary: density (ρ), velocities multiplied by density (ρV_X, ρV_T, ρV_R), energy multiplied by density (ρE), κ, and ε, plus number of species included in the chemistry subroutine. In this section, the way the variables were set for the transpiration surface will be discussed.

In an engine, cooler air is drawn from the high pressure compressor to the high pressure turbine. The configuration of the injection is sketched at *Figure 4.1.5.*

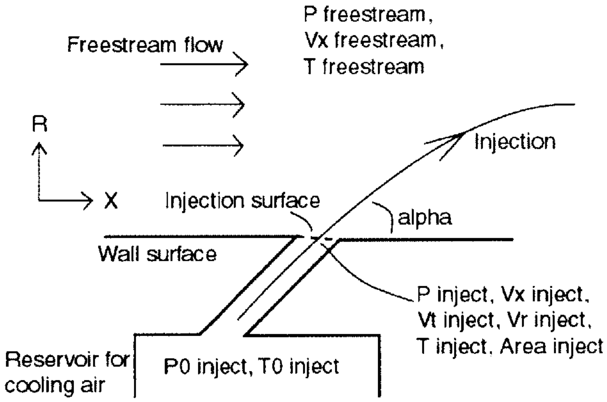
P freestream,
Vx freestream,
T freestream
Freestream flow
R
X
Injection
Injection surface
alpha
Wall surface
P inject, Vx inject,
Vt inject, Vr inject,
T inject, Area inject
Reservoir for
cooling air
P0 inject, T0 inject

Figure 4.1.5. Configuration of the injection

The injection flow path consists of three parts: reservoir, injection surface, and free-stream. The reservoir is where the air from the high pressure compressor is stored. In the reservoir, the air is approximately stagnant and at the same total pressure and total temperature as in the high pressure compressor, neglecting any losses. Then, the mass to be added will go through the injection surface (or transpiration surface) out to the free-stream. One important note is that the static pressure from the injection air at the injection surface, must be equal to the static pressure in the free-stream, since the flow is subsonic. The total mass being added depends on the total pressure in the reservoir, which determines the injection velocity based on the free-stream static pressure, the density of the injection air, and the area of the injection surface.

In this investigation, the amount of mass being added and its temperature were specified. To determine the amount of mass being added, i.e. the mass flow ($\dot{m}$), it is necessary to know the density and the velocity of the mass being injected, and the area of the injection surface. From conservation of mass (Eq. 4.1.8).

$$\dot{m}_{inject} = \rho_{inject} u_{inject} A_{inject} \qquad (4.1.8)$$

A_{inject} is known based on the injection surface. U_{inject}, corresponds to the injection velocity normal to the injection surface to calculate the actual mass flow. It can be found by the isentropic relationship between the static pressure at the injection surface and the total pressure in the reservoir, along with the static temperature (Eq. 4.1.9). Also, C_p and γ are chosen for the properties of air and assumed to be constant.

$$U_{inject} = Ma = M \cdot \sqrt{\gamma \cdot C_p (1 - \frac{1}{\gamma}) \cdot T_{inject}}$$
$$p_{0inject} = p_{inject} \cdot (1 + \frac{\gamma - 1}{2} M^2)^{\frac{\gamma}{\gamma - 1}} \tag{4.1.9}$$

Density of the injection mass is calculated from the equation of state. Referring back to the equation for mass flow at Eq. 4.1.8, to obtain the desired mass flow to be injected, only static temperature of the injection mass, and its normal velocity and the injection angles need be specified. Therefore it is actually not necessary to use Eq. 4.1.9 in this case. However, if the mass addition is determined as a system point of view, injection velocity and temperature will not be known and have to be determined from the total pressure and total temperature from high pressure compressor. In that case, Eq. 4.1.9 will be required.

To specify the amount of mass being added, the blowing ratio (B) is used. It is the ratio of the injection momentum to the free-stream momentum.

$$B = \frac{\rho_{inject} U_{inject}}{\rho_\infty U_\infty} \tag{4.1.10}$$

It is preferred over setting the percentage of mass being injected because the injection may not be uniform over the whole transpiration surface. For example, if the mass addition is done on the blade surface, different pressures on the suction side and the pressure side of the blade will lead to different injection velocities hence different amounts of mass being added on the two surfaces. This makes it difficult to determine the injection velocity required to achieve the desired percentage of mass addition. However, when the blowing ratio is used, the blowing ratio is the same everywhere on the injection surface, which makes it much more straightforward to determine the injection velocity on the transpiration surface. The actual percentage of mass being injected was determined after the calculation was complete. To achieve the desired percentage of mass addition, trial and error of the blowing ratio could be necessary, although a good initial guess can usually be obtained for simple geometries.

In the application of the blowing ratio into the code, inlet momentum is used instead of free-stream momentum. This is because in the code itself, it is difficult to find out which nodes correspond to the free-stream locations. The inlet however, is a boundary where information is readily available.

Again, the goal of the whole process above is to find the normal injection velocity. With the blowing ratio, inlet momentum, and the density of the injection mass, the normal injection velocity can be found. In actual applications, it is not that common to have normal injection. Usually the mass is injected at an angle with the free-stream. The advantage is it will help the injection to stay close to the wall surface to form a cool protective layer from heat damage. Also, the presence of some stream-wise momentum from the injection can prevent the flow from separating. Therefore, in the implementation of the mass addition capability to the code, two angles, which are perpendicular from the surface normal direction, can be set to control the direction and angle of the mass being injected.

The chemical composition of the mass being injected is also set through the boundary conditions on the transpiration surface. As mentioned in Chapter II, the current code utilizes the truncated Mueller mechanism with 29 species and 79 reactions. Thus, the injection mass can be composed of any of the 29 species by setting the mass fractions on the transpiration surface. If the injection mass is air, then the mass fractions of nitrogen and oxygen will be set accordingly with the mass fraction of other species set to zero. Since C_p and γ are assumed to be constant throughout the calculation, R will also be constant. Therefore, changing the composition of the injection mass will not affect its density, which is certainly not true in actual cases, but this approximation is sufficient in our scenario.

4.5. Summary of Code Modification

To include the mass addition capability to the existing CNEWT code, two major changes were carried out: removal of the wall functions completely, and addition of a new transpiration boundary condition. Wall functions were removed mainly because of incompatibility with the no-slip boundary condition, which is the foundation in creating the new transpiration boundary condition. It is possible to keep the wall function, but significant changes and additional investigation may be required. The incorporation of mass addition is carried out mainly through enforcing certain variables to the desired values on the new transpiration boundary surface. The mass addition is determined by the blowing ratio (which relates to the percentage of mass added), the injection angles, the static temperature of the injection mass, and the species composition of the mass added. Assessment of the mass addition capability will be discussed in the following chapter.

V. Mass Addition Assessment with Square Duct Geometry

To implement and assess the addition of mass addition capability to the code as described in previous chapter, a square duct geometry was chosen for simulation. A square duct was chosen because it provides the simplest flow condition possible along with flat surfaces, which makes the code debugging process easier. Also, several square duct geometries have been created and simulated in [2]. Previous simulations provide some level of comparisons in the code changing process. Eventually, the code will be implemented into blade calculations to investigate the effect of blade cooling with mass addition on species evolution in a high turbine stage of an engine. In the following sections, a description of the duct geometry will be given first. This will be followed by the results of calculations carried out without chemistry, mainly to validate the mass addition capability. The results of calculations with chemistry will be described in the end to look at the effects on trace species evolution with mass addition.

5.1. Square Duct Geometry

The square duct used in the calculation has a size of 0.125 m x 0.125 m x 0.5 m (*Figure 5.1.1*). It was created in PRE, the grid-generating code for CNEWT. There are two different grid densities available: Grid 94b, has a total number of 180000 cells with more grid points clustered near the surfaces. Grid 95, with 304200 cells, has grid points evenly distributed across the whole domain. The specifications for both grids are summarized in *Table 5.1.1* and shown in *Figure 5.1.2.*

	Grid 94b	**Grid 95**
No. Cells	180000	304200
No. Grid Points	33516	55404
No. Edges	56810	368775
No. Boundary Nodes	13600	18304

Table 5.1.1. Grid specifications

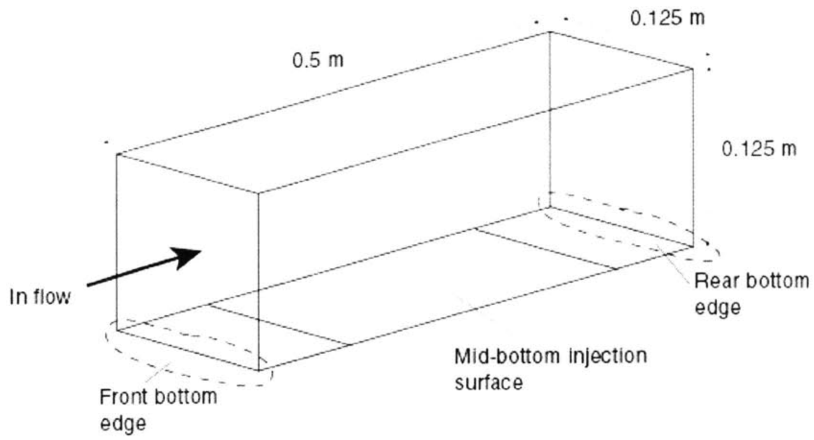

Figure 5.1.1. Duct geometry

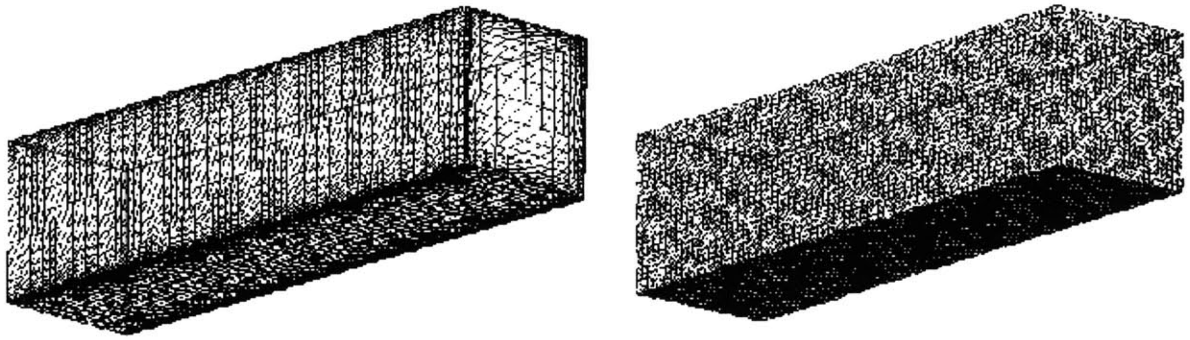

Figure 5.1.2. Grid 94b (left), Grid 95 (right)

For mass addition in the duct geometry, the mid-bottom surface (x = 0.1 m to x = 0.4 m) was chosen to be the injection surface (*Figure 5.1.1*). The existing grids were slightly modified to partition the bottom surface such that different boundary conditions (no injection vs. injection) can be set on the surfaces. Originally, the whole bottom surface was set to be the injection surface. However, there were some conflicts with the boundary condition settings near the front bottom edge and the rear bottom edge (*Figure 5.1.1*). Further, having injection on the mid-bottom surface also has the advantage of allowing observation of the transition from no injection to injection over the bottom surface. The other duct surfaces, which are completely free from injection, provide comparison with the bottom surface.

The code modification process with duct geometry calculations is summarized in stages shown in *Figure 5.1.3.* At the beginning of the code modification process, Grid 94b was utilized because of its fewer grid points, i.e. faster calculation time, and satisfactory results with the original CNEWT code as reported in [2]. However, during the code modification process in stage 1, when testing the no-slip boundary condition with the no injection case, unsatisfactory results were obtained. The three major problems noted were loss of mass flow, non-uniform distribution of the flow, and oscillations. The problems were first thought to be related to the modification made to the code. However, after several runs and comparisons with calculations done using Grid 95, the problems were found to be dependent on the grid itself since the problems were much less severe when Grid 95, a denser grid, was used. Details of the problems are briefly described below. Note that these problems exist only when the modified code is used. Thus these problems are related to the new boundary conditions, i.e. the no-slip condition, being enforced in the modified code.

Stage 1: Remove wall function and enforce no-slip boundary condition
(test with duct geometry)

↓

Stage 2: Include mass addition boundary condition
(test without injection with duct geometry)

↓

Stage 3: Test normal injection on the bottom surface of the duct

↓

Stage 4: Test angled injection on the bottom surface of the duct

↓

Stage 5: Include chemistry specification in mass addition
(test with and without injection with duct geometry)

Figure 5.1.3. Code development and testing stages

5.1.1. Loss of Mass Flow

For the adiabatic duct calculation, without mass addition, the mass flow going into the duct should be the same as the mass exiting the duct, i.e. the mass should be conserved. However, in the calculation with Grid 94b, a ~ 3% mass loss (compared to the inlet mass flow) was observed. The mass-averaged axial mass flux distribution is shown in *Figure 5.1.4.*

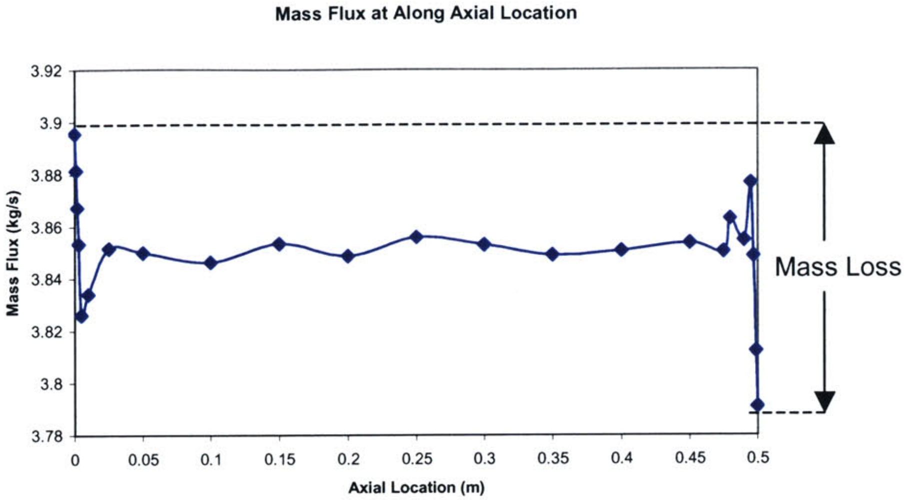

Figure 5.1.4. Mass flow along axial locations of the duct

As shown in the plot, almost all the mass losses occur within the first layer of cells (x = 0 – 0.0065 m) and the last layer of cells (x = 0.4935 – 0.5 m) of the duct. At these locations the inlet and exit boundary conditions of the duct meet with the no-slip wall boundary conditions. It is suspected that the meeting of two different boundary conditions requires a larger number of nodes to resolve the situation accurately and to minimize the errors that may arise. When the same case is run using Grid 95, the mass flow difference decreases to ~ 0.3%, which is much more reasonable.

5.1.2. Non-uniform Distribution of the Flow

Calculations done using the square duct geometry without mass injection are expected to yield uniform and symmetric results. However, this is not the case when Grid 94b was used, especially near the exit of the duct. Velocity vectors and streamlines are shown in *Figure 5.1.5* to demonstrate the problem.

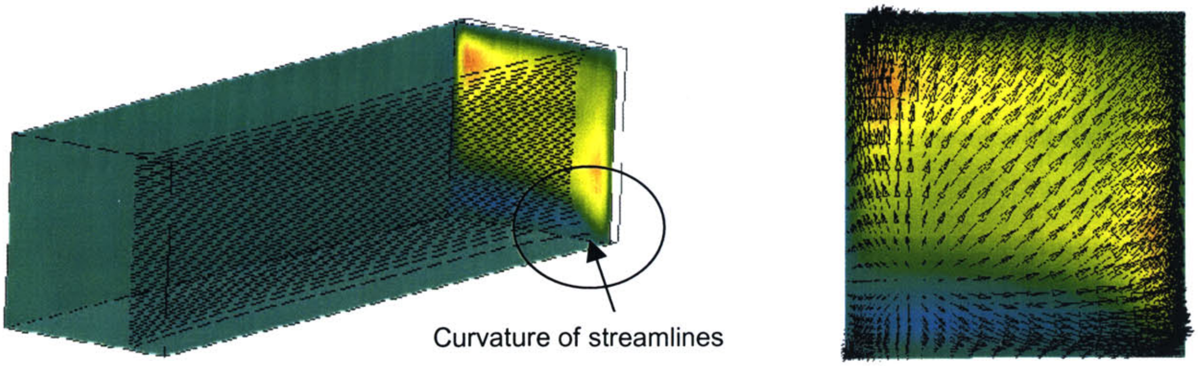

Figure 5.1.5. Radial velocity (shown in color) along with streamlines of the duct (left), velocity vectors at axial location x = 0.49 m (right)

Curvature of the streamlines near the exit is observed. The swirl can be seen more clearly in the plot on the right of *Figure 5.1.5* with velocity vectors. This behavior is related to the grid itself as shown in *Figure 5.1.6.* Similar issues are discussed in [2]. When the same case is run using the denser grid Grid 95, the magnitude of the problem is significantly reduced.

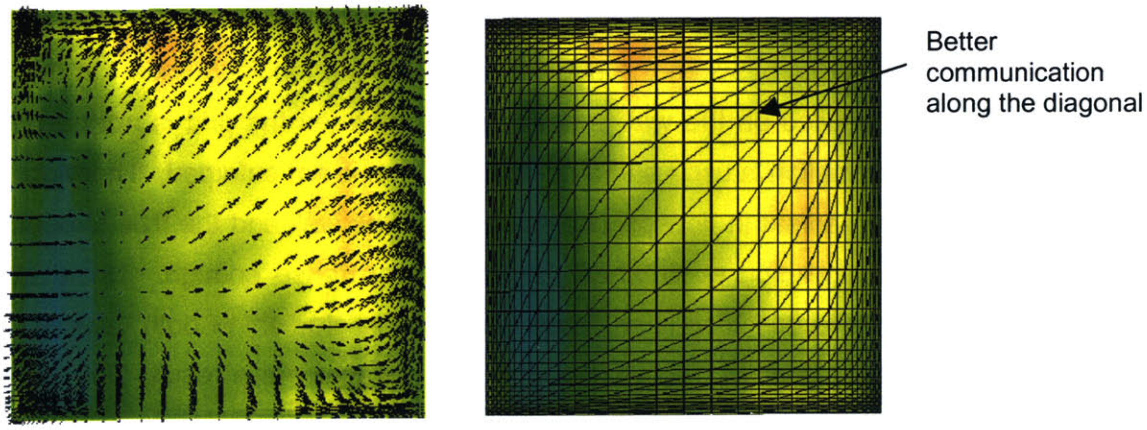

Figure 5.1.6. Velocity vectors with tangential velocity (color) (left), the grid at that location (right)

5.1.3. Flow Property Oscillations Near the End of the Duct

The last problem associated with the grid is related to oscillations observed on the wall surfaces and non-uniform distributions near the exit of the duct (*Figure 5.1.7*).

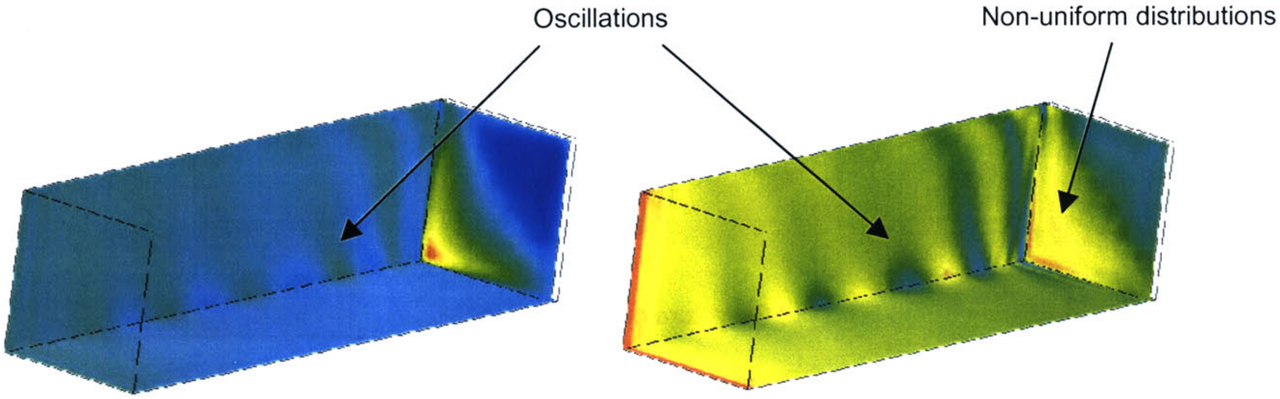

Figure 5.1.7. Temperature (left), and pressure (right) oscillations observe in the duct

The cause for the oscillations is not known but using Grid 95 solved the problem, i.e. the problem is again grid related.

All three problems described above are much alleviated when the denser grid is used. Therefore when the new wall boundary conditions are implemented, higher grid resolution is required. This agrees with the discussion in the previous chapter regarding the change in wall boundary conditions between the original code and the modified code. In the original code, a wall function is used on the wall surface such that when the grid is not dense enough, some level of approximation is used and a no-slip condition is not enforced. Therefore it will result in a much smaller gradient in flow properties between the wall and the free-stream, and it allows a more robust calculation even when the grid is not dense enough. However, in the current situation, a no-slip condition is enforced and a larger gradient of both velocity and temperature (if non-adiabatic) must be resolved on the wall surface. As a result, Grid 95 was used in the following calculations whenever the modified code was used.

One more comparison between Grid 94b and Grid 95 is the case when there is cool mass addition in the mid-bottom surface of the duct (*Figure 5.1.8*). The difference in the result is quite significant and a series of tests with different grid densities is highly recommended when the modified code is used on a new geometry.

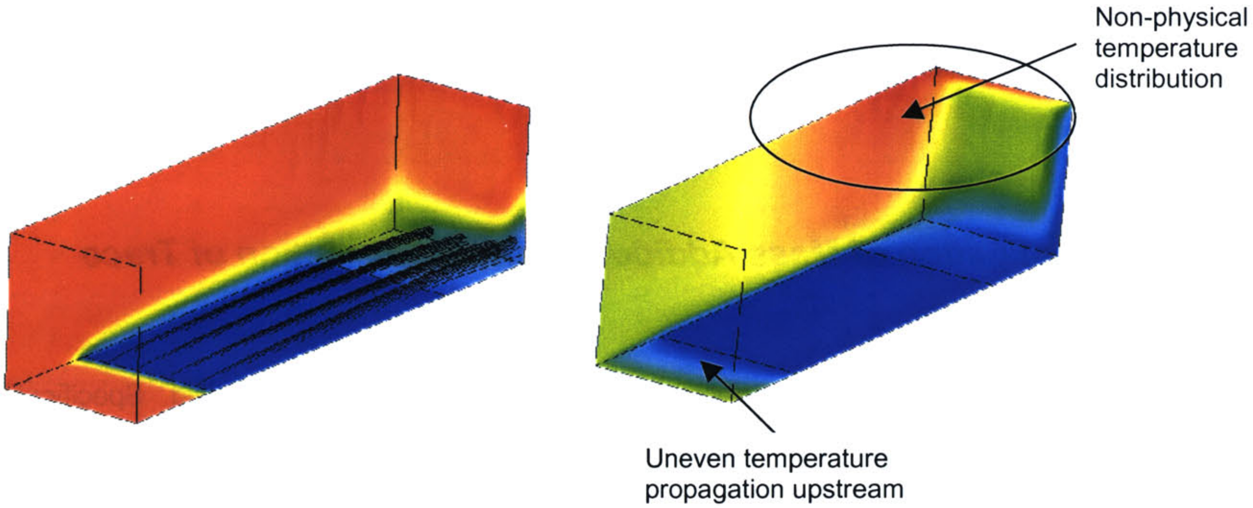
Non-physical temperature distribution
Uneven temperature propagation upstream

Figure 5.1.8. Temperature plot with Grid 95 along with streamlines coming out from injection surface (left), temperature plot with Grid 94b (right)

For the calculation using Grid 94b (*Figure 5.1.8 right*), non-physical temperature distributions are observed. This further stresses the importance of having a dense enough grid to obtain accurate results.

The calculation done using Grid 95 (*Figure 5.1.8 left*) reveals some features of mass addition using the modified code. In the calculation, mass with a blowing ratio of 0.025, which is equivalent to around 3% of inlet mass flow, is being injected from the mid-bottom surface at a temperature 825 K (free-stream temperature ~1150 K). For the other surfaces, an adiabatic wall with a no-slip condition is utilized. Chemical reactions are not included in this calculation. In terms of temperature, the temperature inside the duct should be uniform when there is no mass addition or no non-adiabatic wall setting. Thus, as shown in the figure, the only source for temperature change is due to mass addition from the mid-bottom surface. The cooler temperature from the injection mass is then convected and diffused outward and downstream at the same time forming a thermal boundary layer. The mass is injected at 30 degrees from the surface, which is typical of many turbine blade film-cooling applications. As the streamlines approach the exit of the duct, the non-uniform flow problem described above starts to develop and causes the streamlines to move sideways (tangentially).

A series of tests have been carried out with various conditions on Grid 95 to assess the mass addition capability. Blowing ratio, injection angles, injection temperature, etc. have been varied and yielded satisfactory results. Chemical specification of the injection mass was then included in the code for the investigation of the impact of mass addition on trace species evolution.

5.1. Investigation of Mass Addition Effect on Evolution of Trace Species

After the above calculations without chemistry, chemical reactions were included. Specification of the chemical composition is included for the mass being injected. The inclusion of mass addition to simulate the cooling effect rather than just setting a cool wall temperature is expected to have several effects:

- Provision of more N_2 and O_2 may enhance production of certain species
- Addition of mass will produce a dilution effect
- Production of a special flow environment with injection may favor some chemical pathways

To allow a comprehensive investigation of the above effects, a test matrix with a total of four calculations was developed (*Table 5.2.1*). The temperature and pressure used corresponds to typical turbine stage flow settings with a Mach number of approximately 0.2. A blowing ratio of 0.025 corresponds to a mass injection of ~ 3% relative to the inlet mass flow.

	Case 1 No-slip - Air injection	**Case 2 No-slip - Argon injection**	**Case 3 No-slip - no injection**	**Case 4 Original code - no injection**
Inlet total temperature (K)	1161.17	1161.17	1161.17	1161.17
Inlet total pressure (Pa)	810200.0	810200.0	810200.0	810200.0
Exit static pressure (Pa)	778100.0	778100.0	778100.0	778100.0
Blowing ratio	***0.025***	***0.025***	***0***	***0***
Injection angle (degrees from surface)	***30***	***30***	***N/A***	***N/A***
Injection/non-adiabatic wall temperature (K)	825	825	825	825
Injection mass composition (N2/O2/AR)	***0.767 / 0.233 / 0***	***0 / 0 / 1***	***N/A***	***N/A***

Table 5.2.1. Test matrix for mass addition investigation on evolution of trace species

No-slip cases in the test matrix correspond to cases calculated using the modified code with the mass addition capability. The original code case corresponds to the case calculated using the unmodified CNEWT code with wall functions. Differences in specification between cases are shown in bold italic in *Table 5.2.1.* The following comparisons were carried out to isolate and study various effects from mass addition.

1. Comparison between Cases 1, 2, and Case 3 shows the overall effect of mass addition on trace species evolution. Since the calculations are from the same code with the same inlet flow conditions, the differences observed in the result will be solely due to the addition of mass.

2. Comparison between Case 3 and Case 4 shows the effects from different wall boundary conditions: no-slip vs. wall function. With the no-slip condition, a larger velocity gradient results, i.e. zero velocity on the wall compared to a finite slip-velocity for the wall function case. Thus the no-slip case should provide a longer flow residence time for production of certain species.

3. Comparison between Case 1 and Case 2 investigates the effects of dilution (Case 2) and dilution plus chemistry (Case 1) from mass addition. When air is injected, which is composed of Nitrogen and Oxygen, it has a potential to react with existing species in the free-stream to form atomic oxygen (O), which is highly reactive, and atomic nitrogen (N). Production of atomic nitrogen may perturb the production of NO_y species. At the same time, addition of extra mass in the flow domain may "dilute" the existing species. To determine which of the above two effects is more important in the mass addition process, Case 2, which injects Argon instead of air, was carried out. Since Argon is inert and is not involved in any of the species reactions, injection of Argon will reproduce the dilution effect without any additional chemical effects.

In the following, the variables that are of interest are: temperature, pressure, axial velocity, O_2, N_2, NO_2, HONO, SO_3, and H_2SO_4. Each variable will be presented and compared one by one. For each case, a cross-section at a mid-circumferential location of the duct will be made to show the change of the particular variable in a 2-D manner. At the same time, its radial profile will be obtained at four different axial locations (x = 0.05 m, 0.15 m, 0.35 m, 0.45 m) to show how the profiles change progressing downstream (*Figure 5.2.1*). Note that the first and last axial locations are not on the injection surface. A summary of the comparisons will be given at the end.

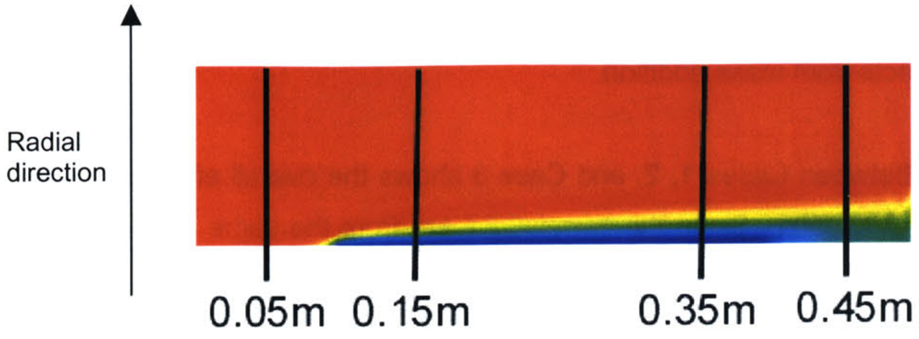

Figure 5.2.1. Axial locations for the duct profile

5.2.1. Static Temperature

Static temperature is of special interest because it is one of the most important drivers in chemical reactions. For the injection case, cooler mass is injected through the mid-bottom surface. For the non-injection case, the cooling effect is simulated via setting a cooler wall temperature. In this investigation, the wall temperature, or the injection mass, is set to have a temperature of 825 K while the free-stream temperature is around 1150 K.

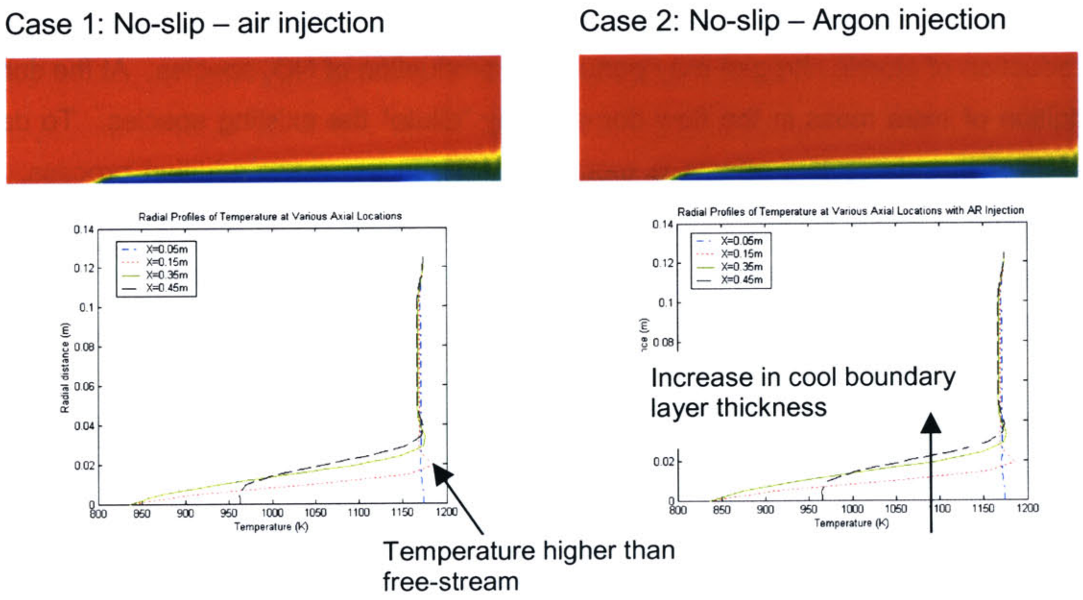
Case 1: No-slip – air injection

Case 2: No-slip – Argon injection

Increase in cool boundary layer thickness

Temperature higher than free-stream

Figure 5.2.2. Temperature distribution for Case 1 and Case 2

The two injection cases (Case 1 and Case 2) attain the same temperature profiles (*Figure 5.2.2*). As shown in the duct side view, the injection surface is the sole source of cooling flow. The injection mass forms a cool boundary layer and convects downstream. When looking at the radial profiles, the free-stream temperature remains identical over the four axial locations. At x = 0.15 m, the hotter free-stream flow was cooled by the cooling air from the injection surface such that a temperature of 825 K is attained on the wall. It is interesting to note that right at the boundary of the cooling air and the free-stream flow at x = 0.15 m, a temperature higher than free-stream is observed. The cause of the observation is unknown. It is suspected that the result is related to inadequate resolution of the shear layer flow between the injection mass and the free-stream. However, comparing with the no injection case below (Case 3, 4) shows that similar effect occurs when there is no mass injection, thus the cause is not injection related (*Figure 5.2.3*). Also shown in the radial profiles is the growth of the cool boundary layer when going from x = 0.15 m to 0.45 m. At x = 0.45 m, as it is outside the injection surface, the wall temperature increases back to ~ 960 K due to heat transfer from the free-stream.

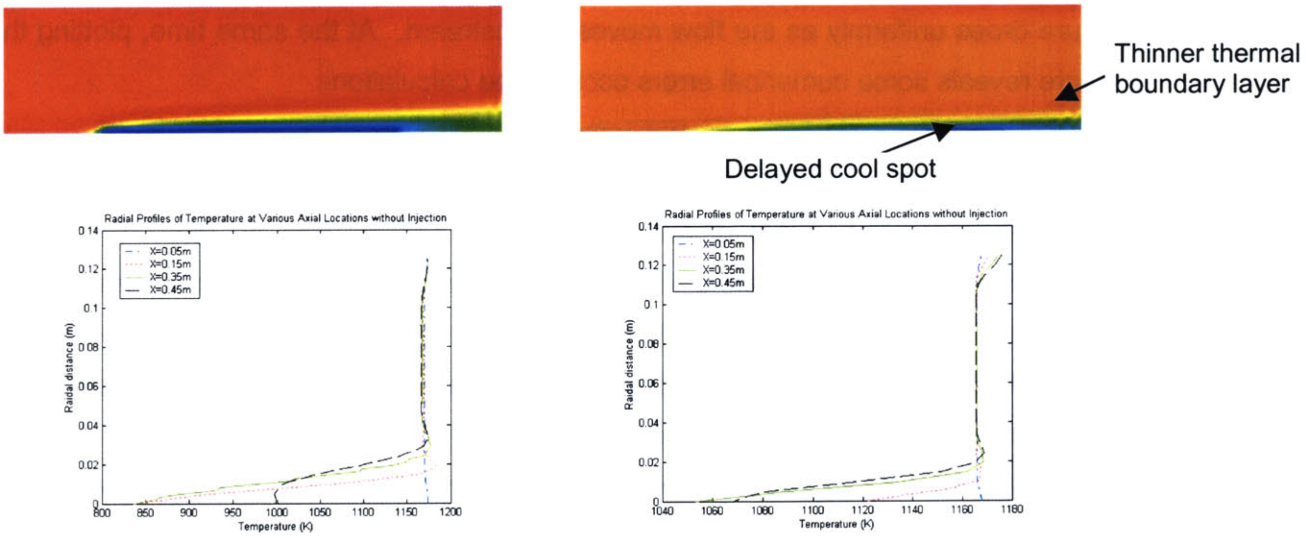
Case 3: No-slip – no injection

Case 4: Original code – no injection

Thinner thermal boundary layer

Delayed cool spot

Figure 5.2.3. Temperature distribution for Case 3 and Case 4

Comparing the injection cases (Case 1 and Case 2) with the no injection case (Case 3) does not reveal a large difference in terms of temperature. Similar radial temperature profiles with similar thermal boundary thickness are achieved. The only difference observed is a slightly higher wall temperature at x = 0.45 m (~ 1000 K vs. ~ 960 K). It seems that with mass addition, the cooling effect lasts longer.

The calculation done using the original code (Case 4) achieves a much higher and varying wall temperature on the cooling surface due to the presence of the wall function. Although 825 K is set to be the desired wall temperature, it achieves a temperature of ~ 1120 K at x = 0.15 m, ~ 1060 K at x = 0.35 m, and ~ 1070 K at x = 0.45 m. Note that the cooling effect is delayed and shifted downstream with the coolest wall temperature achieved at ~ x = 0.25 m – 0.45 m, contrary to the modified code where the coolest temperature is achieved on the cooling surface at the cooling temperature being set. Also, the original code calculations produce a slightly thinner thermal boundary layer, partly related to the higher wall temperature achieved.

5.2.2. Static Pressure

Pressure also plays an important role in species evolution. However, in the duct calculation, there will be minimal pressure changes, especially in the radial direction, regardless of presence of mass injection. In the square duct, because of losses through boundary layers, the static pressure drops uniformly as the flow moves downstream. At the same time, plotting the static pressure reveals some numerical errors occur in the calculations.

For the no-slip cases (Cases 1, 2, and 3), the same pressure drop and radial profiles are obtained (*Figure 5.2.4, 5.2.5*), showing that mass addition has no effect on the pressure changes as expected. Comparing to Case 4, however, the averaged pressure drop between the inlet and exit of the duct calculated using the modified code is larger. This is mainly because of the difference in the boundary layer. As mentioned before, in the modified code with the no-slip condition, axial velocity goes from zero on the wall to around 160 m/s in the free-stream (*Figure 5.2.6 left*). In the original code with the wall function, a slip velocity (of only 10 m/s deficit from free-stream velocity) occurs on the wall surface (*Figure 5.2.6 right*). It results in a thinner boundary layer thickness. And a much smaller velocity deficit on the wall results in a much smaller loss.

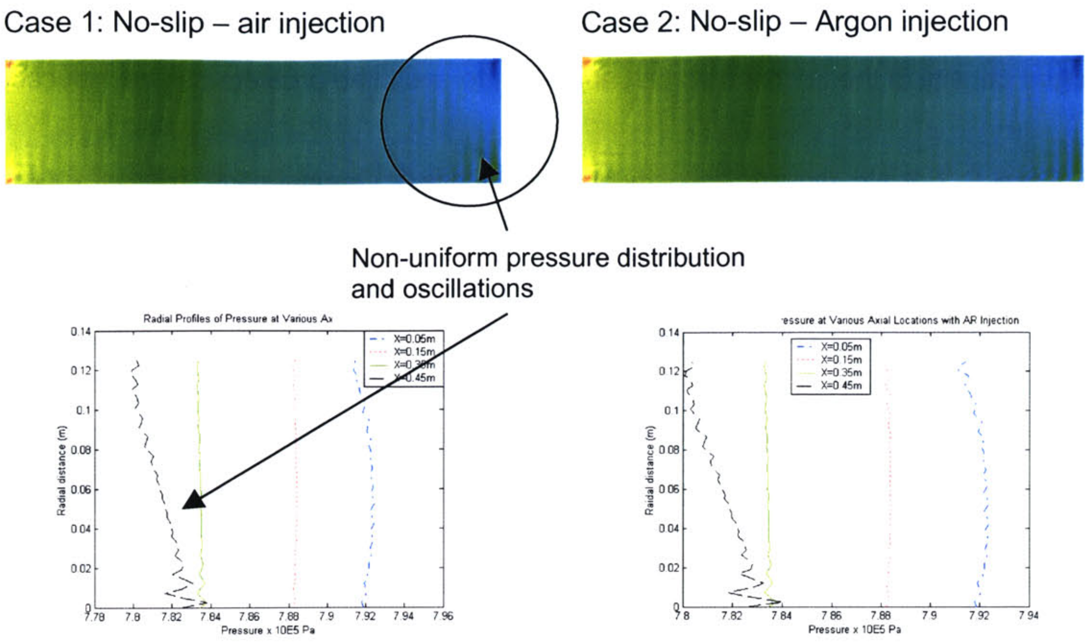

Figure 5.2.4. Pressure distribution for Case 1 and Case 2

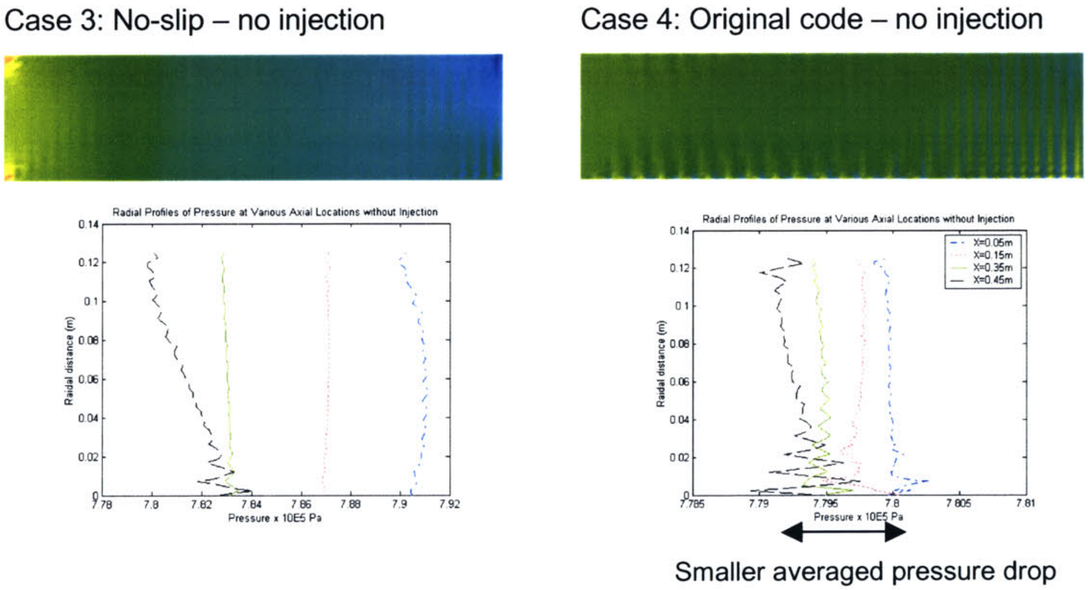

Smaller averaged pressure drop

Figure 5.2.5. Pressure distribution for Case 3 and Case 4

Oscillations from the numerical calculations are apparent especially near the exit of the duct. This is partly related to the grid-dependent swirl near the exit of the duct observed and described before. The swirl and non-uniform velocity distribution near the end of the duct causes the non-uniform radial pressure profile at x = 0.45 m. Further calculations with even higher grid density of the duct should be carried out to see if the problem can be reduced.

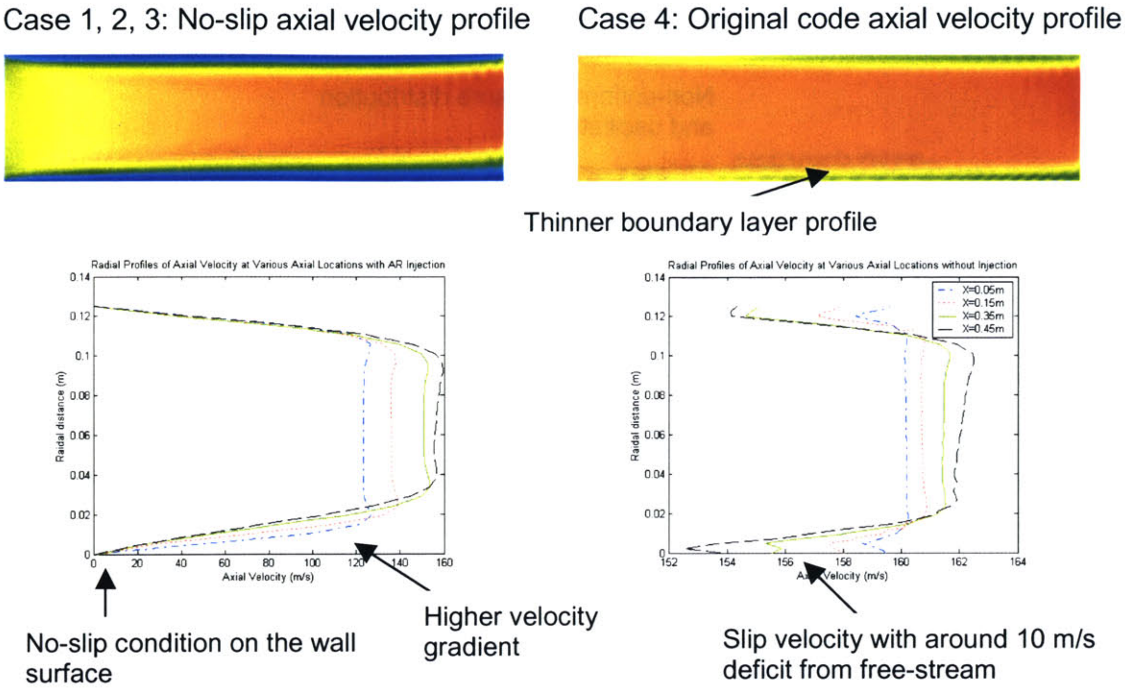

Case 1, 2, 3: No-slip axial velocity profile

Case 4: Original code axial velocity profile

Thinner boundary layer profile

No-slip condition on the wall surface

Higher velocity gradient

Slip velocity with around 10 m/s deficit from free-stream

Figure 5.2.6. Axial velocity profiles comparing no-slip case (left) and wall function case (right)

5.2.3. Oxygen (O_2)

The evolution of oxygen is being observed mainly to visualize the effect when air, composed of oxygen and nitrogen only, is being injected through the injection surface (*Figure 5.2.7, 5.2.8*). It is suspected that injection of air will increase the atomic oxygen levels in the flow domain and lead to increases in production of certain trace species. The actual simulation result will be discussed in the following sections when the species of interest are covered. When there is no injection, the mass fraction of oxygen would remain almost constant through out the duct as there is no combustion process to consume the oxygen and only a very small amount of atomic oxygen will be produced to react with other species. When there is injection, the injection mass has a higher mass fraction of oxygen compared to free-stream, thus leading to an increase in oxygen mass fraction at the exit of the duct.

In Case 1, the injected air has a mass fraction of 0.233 compared to the free-stream value of around 0.15. Thus it forms a boundary layer with higher mass fraction of oxygen and diffuses out into the free-stream. The mass fraction of oxygen in the free-stream remains constant though. Conversely, in Case 2, when Argon is being injected, the mass fraction of oxygen becomes zero on the injection surface. This situation is opposite to Case 1. When there is no injection, Case 3 and Case 4, the mass fraction of oxygen stays constant.

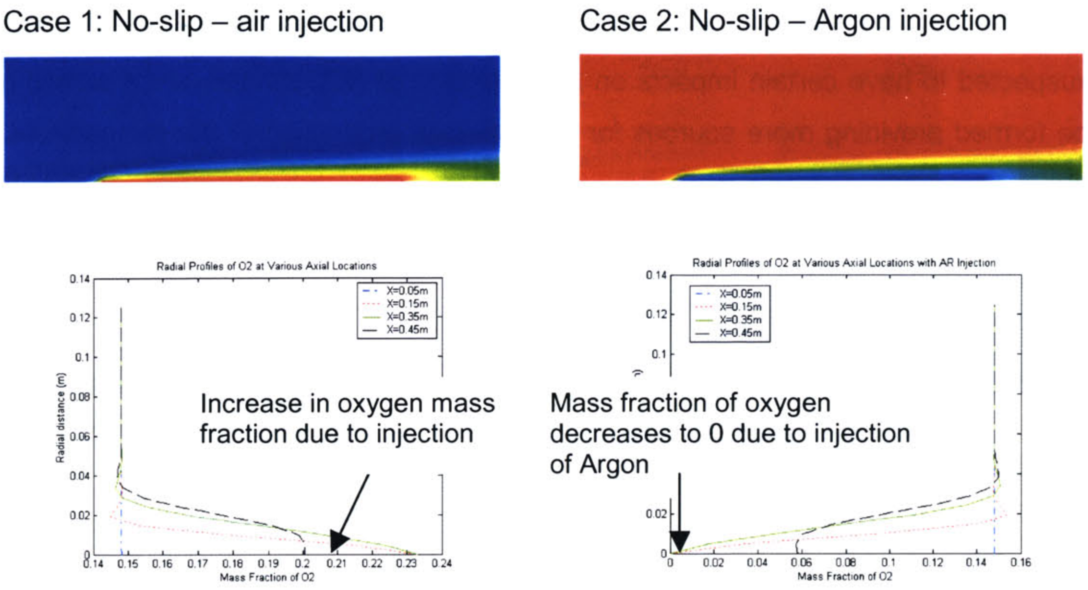
Case 1: No-slip – air injection

Case 2: No-slip – Argon injection

Increase in oxygen mass fraction due to injection

Mass fraction of oxygen decreases to 0 due to injection of Argon

Figure 5.2.7. O_2 distribution for Case 1 and Case 2

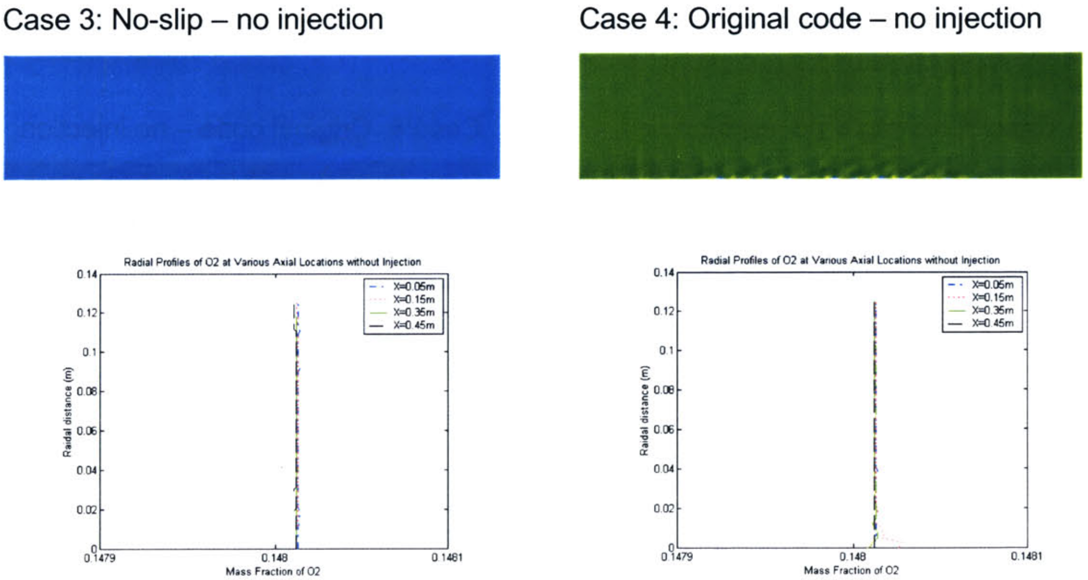
Case 3: No-slip – no injection

Case 4: Original code – no injection

Figure 5.2.8. O_2 distribution for Case 3 and Case 4

5.2.4. Nitrogen (N_2)

The observation for nitrogen is almost exactly the same as the observation for oxygen. When air is being injected, a higher mass fraction in the injection air comparing to the free-stream leads to an increase in nitrogen mass fraction at the exit of the duct (*Figure 5.2.9*). Nitrogen is also suspected to have certain impacts on the evolution of NO_x species since atomic nitrogen may be formed providing more sources for NO_x species production (if the temperature is high enough).

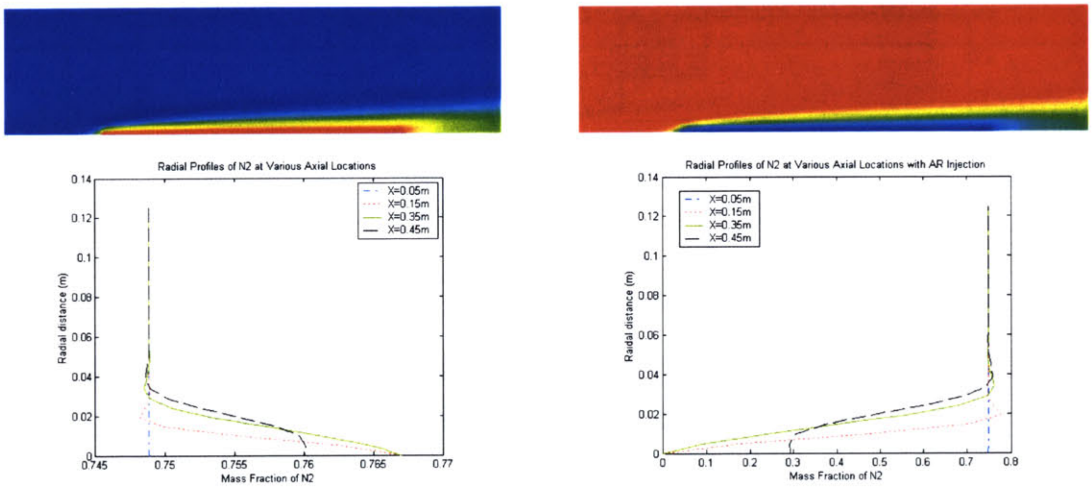
Case 1: No-slip – air injection

Case 2: No-slip – Argon injection

Figure 5.2.9. N_2 distribution for Case 1 and Case 2

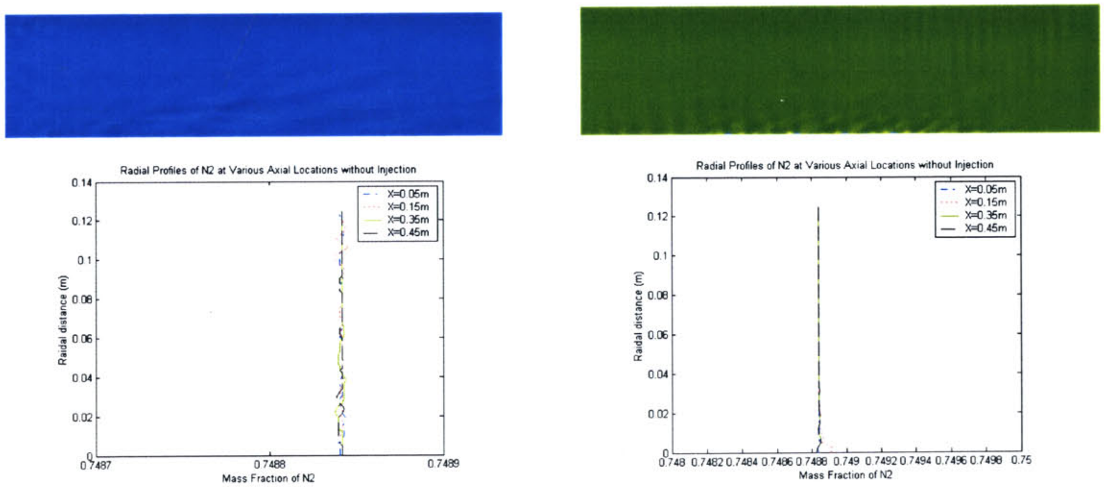
Case 3: No-slip – no injection

Case 4: Original code – no injection

Figure 5.2.10. N_2 distribution for Case 3 and Case 4

The results show that when air is being injected, higher mass fractions of nitrogen on the injection surface lead to higher mass fractions at the end of the duct. When Argon is being injected, zero mass fraction of nitrogen on the injection surface leads to a decrease in mass fraction of nitrogen. In the free-stream and in the no injection cases, the mass fraction remains constant (*Figure 5.2.10*). Minor oscillations arise from numerical error.

5.2.5. Nitrogen Dioxide (NO_2)

Nitrogen dioxide is one of the species of interest in terms of engine emissions because of its effect on the atmosphere. Also, by keeping track of NO_2, it allows estimation of how other NO_x species are evolving. When there is mass addition, the presence of more nitrogen (as mentioned above) may lead to more production of NO_x species. But at the same time, the presence of only nitrogen and oxygen from the injection air on the injection surface may change the conditions for production of NO_2. The results are shown in the plots below (*Figure 5.2.11, 5.2.12*).

In Case 4, when the calculation is carried out using the original code with the wall function, the effect of boundary layer, i.e. residence time effect, is almost non-existent for the NO_2 reactions. Comparing the top surface and bottom surface of the duct, shows slight effects due to the cooler temperature from the cooled wall at the mid-bottom surface. When looking at the radial profile plots at x = 0.15 m, 0.35 m, and 0.45 m, slightly higher production of NO_2 is observed right at the boundary between the cooler flow due to the cooling surface and the hotter free-stream. As the flow goes through the duct, the amount of NO_2 increases steadily and uniformly. NO_2 is produced mainly because of the non-equilibrium initial condition (resembling the condition at the combustor exit). From the inlet to the exit of the duct, the amount of NO_2 will keep increasing until the local equilibrium, which depends on local temperature, pressure, and presence of other species, is achieved. The lack of secondary effects on the evolution of NO_2 makes Case 4 a good case for background comparison before any effects related to the boundary layer or mass addition are described.

Moving from Case 4 to Case 3, the residence time effect due to the boundary layer becomes much more prominent since production of NO_2 at levels higher than free-stream is observed. Comparing between the top boundary layer and the bottom boundary layer shows some interesting results. Due to the presence of cooler air on the bottom surface, the layer of higher NO_2 production is slightly thicker than the one on the top while achieving a slightly lower value of maximum production.

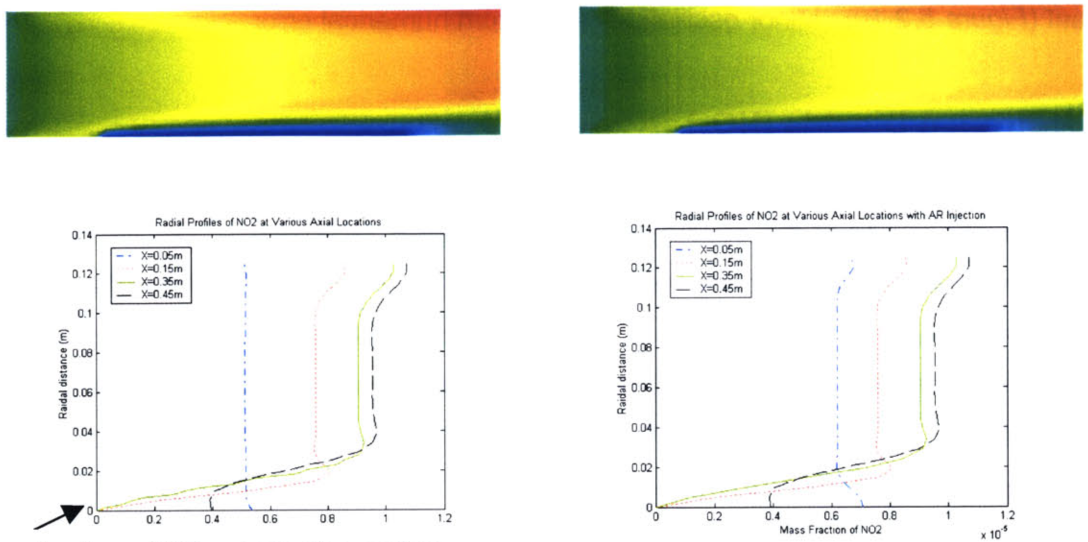

Case 1: No-slip – air injection

Case 2: No-slip – Argon injection

Zero mass fraction of NO_2 on injection surface

Figure 5.2.11. NO_2 distribution for Case 1 and Case 2

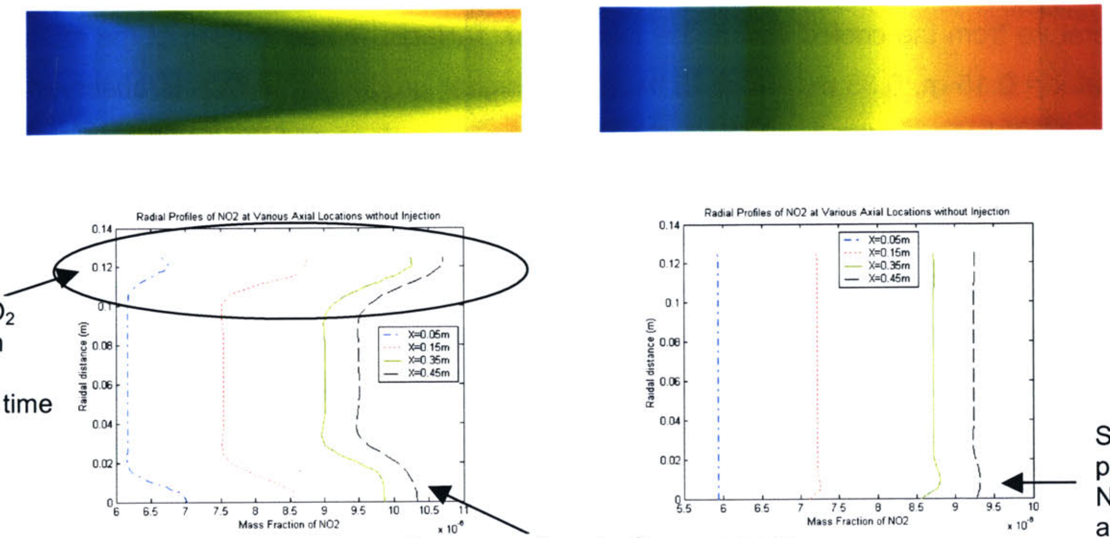

Case 3: No-slip – no injection

Case 4: Original code – no injection

Higher NO_2 production due to residence time effect

Presence of cooler flow seems to "mix out" the production a bit

Slightly higher production of NO_2 at hot/co air boundary

Figure 5.2.12. NO_2 distribution for Case 3 and Case 4

Mass injection (air or Argon) in Case 1 and Case 2 makes significant changes to the evolution of NO_2 on the bottom boundary layer. Since NO_2 is not present in the injection mass in either case, the mass fraction of NO_2 is zero on the mid-bottom surface. This has a large impact because the boundary layer without injection is expected to be a major site for NO_2 production. With injection, the amount of NO_2 is greatly reduced on the injection surface. The presence of extra N_2 seems to have minimal impact on higher NO_2 production when comparing between Case 1 and Case 2.

5.2.6. Nitrous Acid (HONO)

HONO is being investigated in the simulation because it is one of the aerosol precursors and because it is measurable in experiments. It has been observed before that a cool boundary layer (temperature effect) leads to significant production of HONO while the residence time effect is relatively less significant. Although production of HONO is mainly via OH, the possibly higher amount of O radical present due to air injection may perturb the radical pool and affect the HONO production.

Comparing the no injection cases between Case 3 and Case 4 (*Figure 5.2.14*), very high production of HONO is observed on the bottom cooled surface. Case 3 produces a slightly thicker production profile for HONO near the bottom surface relative to Case 4. This also leads to a relatively larger amount of HONO left downstream of the injection surface. Comparing to the effect from the top boundary layer, the effect due to residence time is minimal, though a longer residence time tends to further decrease in the amount of HONO. In the free-stream, continual decrease, instead of increase, in mass fraction of HONO is observed. This is because of the non-equilibrium inlet condition and the sustained high temperature through out the duct. When a higher than equilibrium amount of HONO is set at the inlet, it will tend to decrease as the flow goes downstream to achieve the local equilibrium value. In an actual turbine case, however, work is extracted from the turbine decreasing the temperature in the flow. Lower temperature in the flow favors more HONO. In this duct case, no work is being extracted and the flow remains unaltered. The temperature remains high and fairly constant (as observed above). Thus continual decrease of HONO in the free-stream is observed.

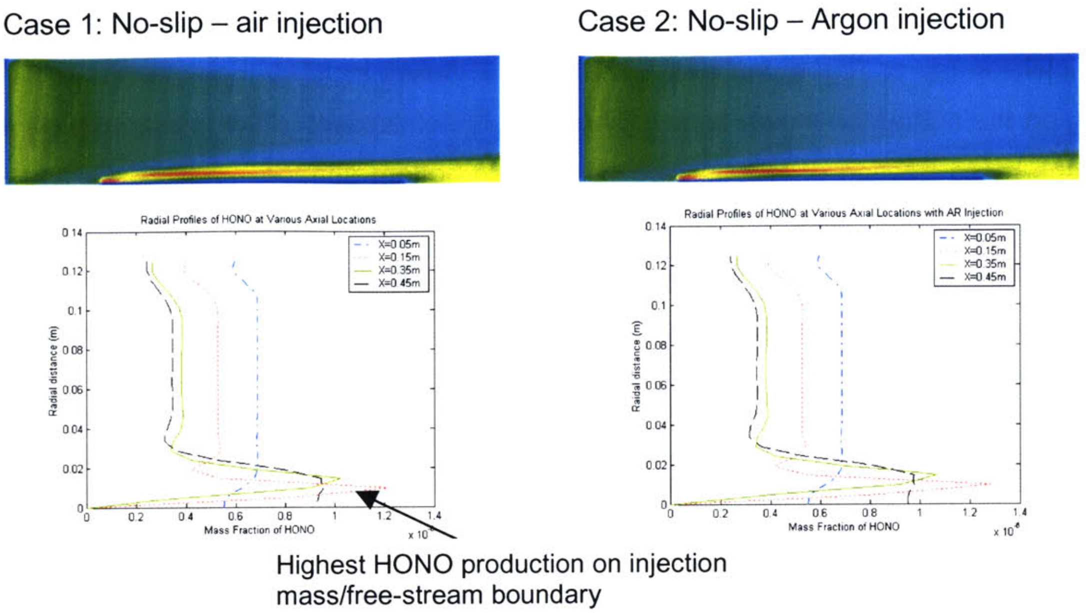
Case 1: No-slip – air injection

Case 2: No-slip – Argon injection

Highest HONO production on injection mass/free-stream boundary

Figure 5.2.13. HONO distribution for Case 1 and Case 2

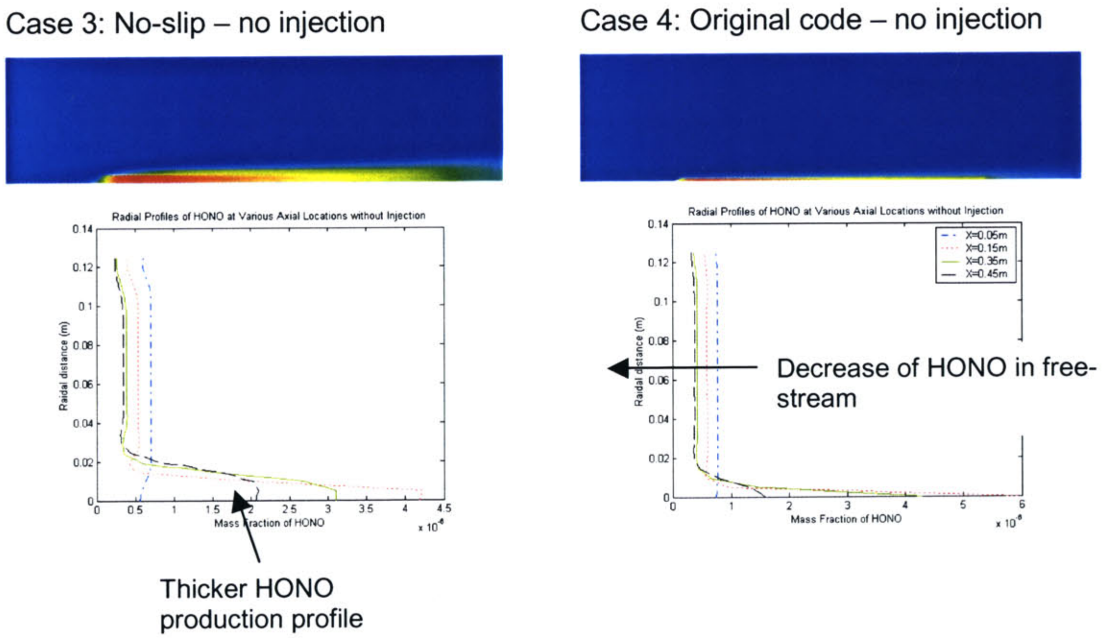
Case 3: No-slip – no injection

Case 4: Original code – no injection

Decrease of HONO in free-stream

Thicker HONO production profile

Figure 5.2.14. HONO distribution for Case 3 and Case 4

In Case 1 and Case 2, the highest production of HONO is observed at the boundary of the cooled injected mass and the free-stream (*Figure 5.2.13*). Unlike the no injection cases, maximum production is not achieved on the injection/cooled surface because zero mass fraction of HONO is set on the injection surface with mass addition. However, cool temperature regions still have the highest potential for HONO production. Therefore, the free-stream is competing with the injection mass to reach high HONO production because of the cool injection while mixing with the HONO-free injection mass. Minimal difference between Case 1 and Case 2 is observed. It seems that the injection of air does not lead to large chemical effects in the evolution of HONO.

5.2.7. Sulfur Trioxide (SO_3)

The behavior of SO_3 is similar to that of NO_2. One major difference is that the SO_3 chemistry is more sensitive to temperature than the chemistry for NO_2. This is most apparent in Case 4 (*Figure 5.2.16*). Comparing the top and bottom boundary layers shows a higher SO_3 production on the bottom boundary layer because of the cooled surface when both surfaces have approximately the same residence time behavior. For Case 3, because of the no-slip condition and higher velocity gradient, the impact of residence time on SO_3 production is more important. In Case 3, the residence time effect has a similar impact on SO_3 production as does the temperature effect.

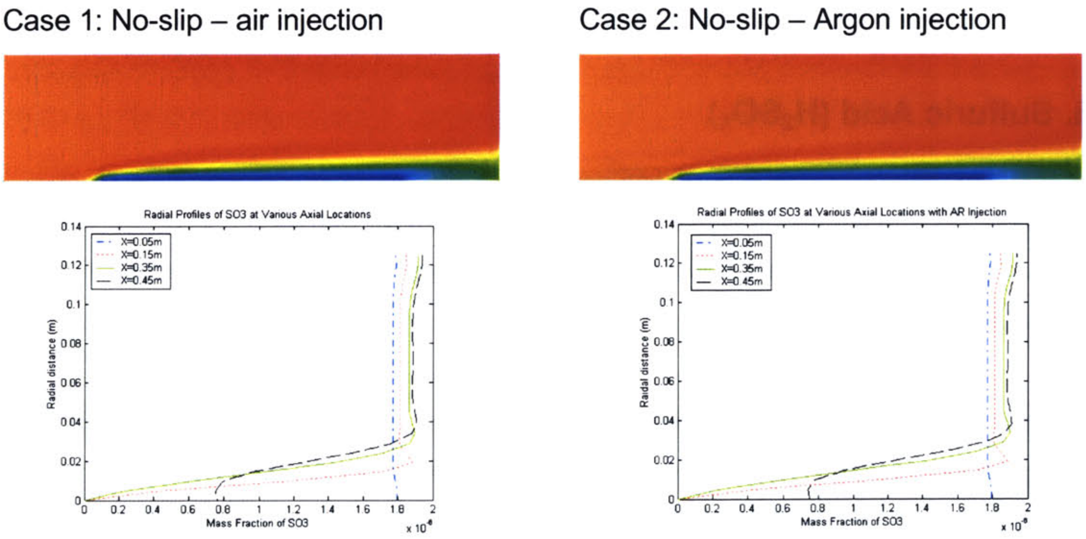

Case 1: No-slip – air injection

Case 2: No-slip – Argon injection

Figure 5.2.15. SO_3 distribution for Case 1 and Case 2

Mass injection leads to zero mass fraction of SO_3 on the injection surface (*Figure 5.2.15*). Unlike HONO, this almost completely eliminates any SO_3 production in the bottom boundary layer. Also, the changes in SO_3 mass fraction on the bottom surface are so large that mask the extent of changes related to the boundary layers. For all four cases, free-stream SO_3 increases steadily moving downstream. This agrees with previous observations for SO_3 production in the turbine stage. Again, Case 1 and Case 2 show minimal difference so the chemical effect related to mass addition beyond dilution seem to be insignificant.

Case 3: No-slip – no injection

Case 4: Original code – no injection

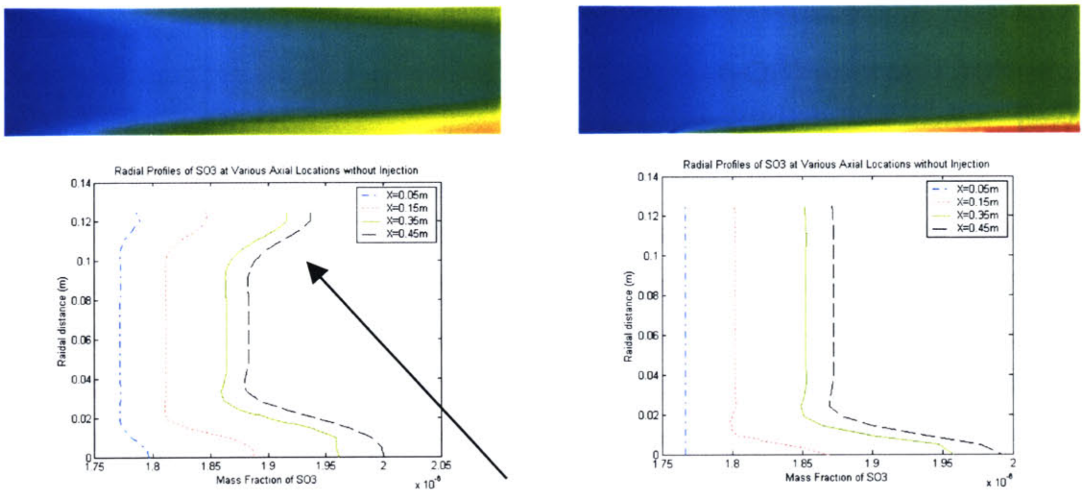

More significant residence time effect compared to Case 4

Figure 5.2.16. SO_3 distribution for Case 3 and Case 4

5.2.8. Sulfuric Acid (H_2SO_4)

The last species considered is H_2SO_4. It is of interest to us because it is an aerosol precursor. H_2SO_4 is like HONO; a major driving force for production is the temperature effect from the cooled surface.

Case 3 and Case 4 show higher production of H_2SO_4 on the cooled surface (*Figure 5.2.18*). However, the production drops significantly downstream (x = 0.45 m) of the cooled surface. For Case 4 in particular, the level of H_2SO_4 decreases almost back to the free-stream value by x = 0.45 m. Similar to previous observations, Case 3 generates a thicker high production profile while Case 4 achieves a higher maximum production.

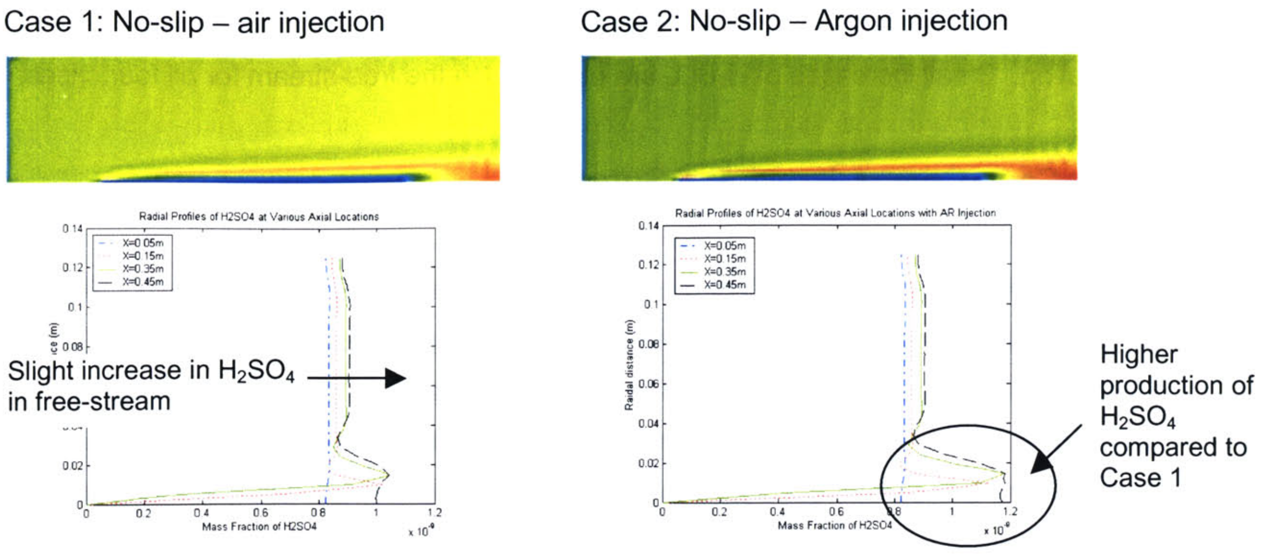
Case 1: No-slip – air injection

Case 2: No-slip – Argon injection

Slight increase in H_2SO_4 in free-stream

Higher production of H_2SO_4 compared to Case 1

Figure 5.2.17. H_2SO_4 distribution for Case 1 and Case 2

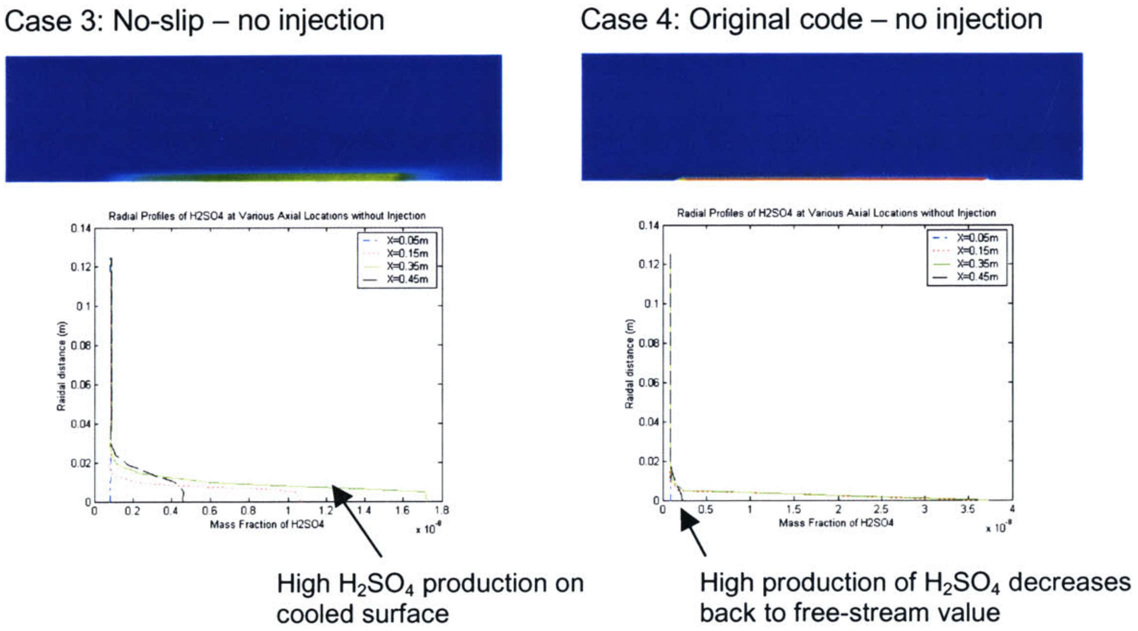
Case 3: No-slip – no injection

Case 4: Original code – no injection

High H_2SO_4 production on cooled surface

High production of H_2SO_4 decreases back to free-stream value

Figure 5.2.18. H_2SO_4 distribution for Case 3 and Case 4

Due to the zero H_2SO_4 boundary condition from the mass injection, Case 1 and Case 2 show highest H_2SO_4 production on the boundary between the injection mass and the free-stream flow (*Figure 5.2.17*). The reasoning is similar to that for HONO. Comparison between Case 1 and Case 2 shows some difference in H_2SO_4 production. Looking at the radial profiles, there is higher H_2SO_4 production when Argon is injected (*Figure 5.2.17*). This is counter to initial expectations that injection of air should enhance trace species production compared to Argon injection. The results show that chemical effects associated with injection of air reduces H_2SO_4 production. Small increases of H_2SO_4 are observed in the free-stream for all four cases.

5.2.9. Case Comparisons and Summary

In this section, comparisons of changes in species between the inlet and exit of the duct will be shown for the four different cases carried out. Although the input flow condition in *Table 5.2.1* is identical for all four cases, different boundary conditions, different codes, along with post-processing errors lead to slightly different flow conditions in the final result. Therefore, all the comparisons are carried out based on the changes between the inlet and exit. All the results are summarized in *Table 5.2.2.*

To facilitate the comparisons, bar charts are plotted below in terms of changes between the inlet and exit of the duct for each variable of concern.

Temperature is shown in *Figure 5.2.19*. For Case 1 and Case 2 when there is mass injection, the same changes in temperature are observed. For Case 3 when there is no injection, a slightly smaller change resulted even though the same cooling temperature was set. The difference between Case 1, 2, and Case 3 shows that with mass addition, the cooling effect is more effective. The change in temperature for Case 4 is smaller than that for Case 3 mainly because the desired cooling temperature is not achieved due to the presence of the wall function. Thus the cooling effectiveness is further reduced.

	Case 1: No-slip - air injection			Case 2: No-slip - Argon injection			Case 3: No-slip - no injection			Case 4: Original code - no injection		
	Inlet	Exit	Delta	Inlet	Exit	Delta	Inlet	Exit	Delta	Inlet	Exit	Delta
Static temperature	1172.368	1147.461	-24.907	1172.358	1147.457	-24.901	1172.01	1152.18	-19.83	1166.048	1158.474	-7.574
Static pressure	7.97E+05	7.79E+05	-17700	7.97E+05	7.79E+05	-17742.5	7.96E+05	7.79E+05	-16700	7.80E+05	7.79E+05	-1321.9
O2	0.14801	0.15308	0.00507	0.14801	0.139185	-0.00883	0.14801	0.14801	0	0.14801	0.14801	0
N2	0.7488	0.7499	0.0011	0.74884	0.704183	-0.04466	0.7488	0.7488	0	0.74884	0.74884	0
NO2	5.04E-06	9.45E-06	4.41E-06	5.04E-06	9.45E-06	4.42E-06	5.03E-06	1.01E-05	5.04E-06	5.02E-06	9.47E-06	4.45E-06
HONO	1.88E-07	3.63E-07	1.75E-07	1.94E-07	3.66E-07	1.72E-07	1.88E-07	4.11E-07	2.23E-07	1.92E-07	4.14E-07	2.22E-07
SO3	1.75E-06	1.80E-06	5.2E-08	1.75E-06	1.79E-06	4.95E-08	1.75E-06	1.92E-06	1.72E-07	1.74E-06	1.89E-06	1.48E-07
H2SO4	4.97E-10	9.15E-10	4.18E-10	5.01E-10	9.30E-10	4.3E-10	4.98E-10	1.10E-09	6.03E-10	4.98E-10	9.81E-10	4.83E-10
AR	N/A	N/A	N/A	5.51E-08	5.96E-02	0.059634	N/A	N/A	N/A	N/A	N/A	N/A

Table 5.2.2. Changes of the species between inlet and exit of the duct

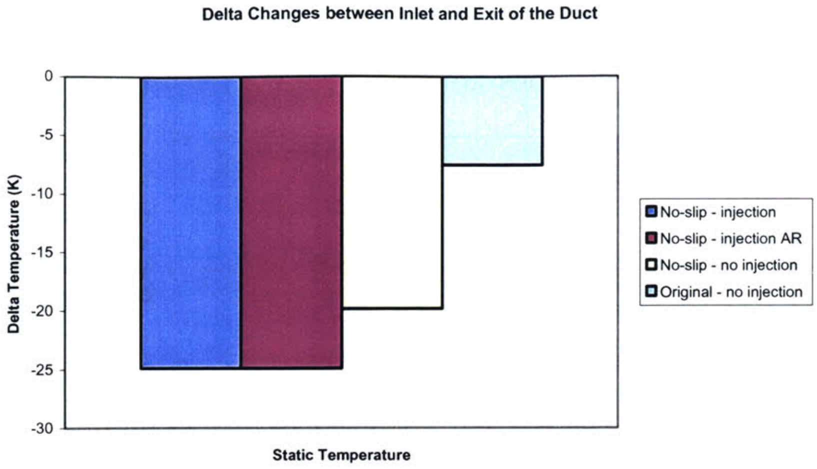

Figure 5.2.19. Temperature changes between inlet and exit of the duct

For pressure, similar trends are observed (*Figure 5.2.20*). The amount of pressure loss is directly related to the boundary layer on the duct surfaces. As seen previously, the boundary layer resolved from the modified code (i.e. Cases 1, 2, and 3) is thicker and has a larger velocity gradient because of the no-slip condition. Therefore, a difference in pressure losses between cases running with the modified code and with the original code is observed. Both injection cases (Cases 1, 2) have the same pressure loss and the loss is slightly more than that for the no injection case (Case 3). It is believed that the extra loss comes from mixing of the injection mass with the free-stream flow.

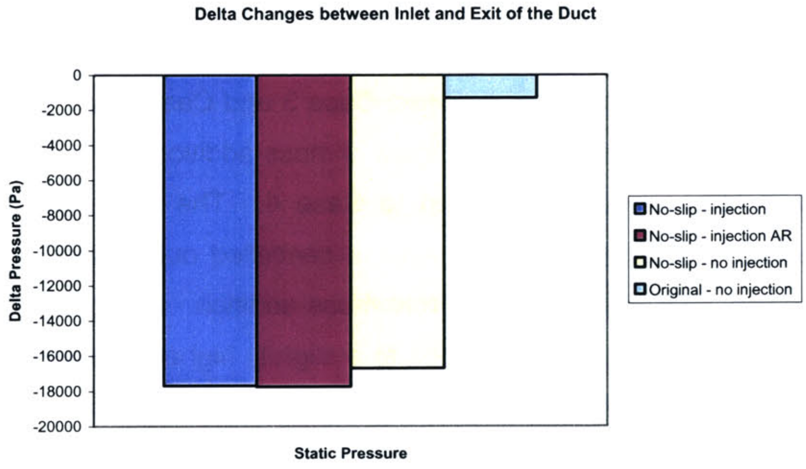

Figure 5.2.20. Pressure changes between inlet and exit of the duct

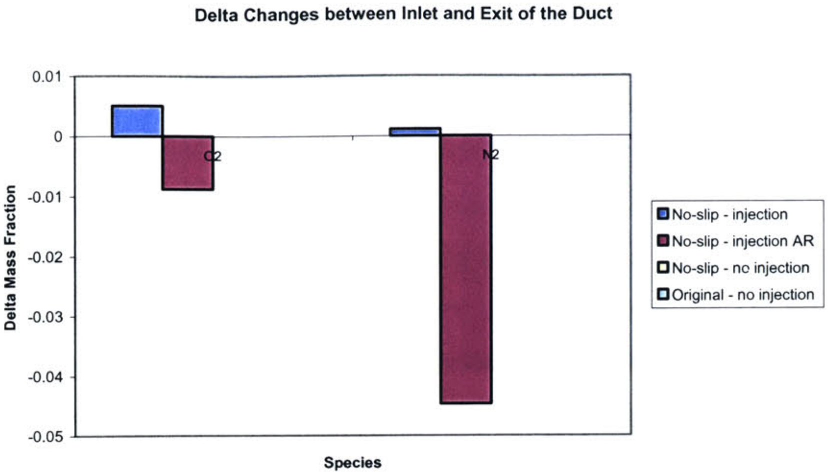

Figure 5.2.21. Oxygen and Nitrogen changes between inlet and exit of the duct

Figure 5.2.21 shows changes of oxygen and nitrogen between the inlet and exit of the duct. Note that no change is observed for both cases without injection (Cases 3, 4) thus no bar is shown in the plot. Changes are observed only in the injection cases. For Case 1, when air is injected, there are increases in both O_2 and N_2 because of the higher mass fraction of both species in the injection air compared to the free-stream flow. When Argon instead of air is being injected (Case 2), decreases of both species are observed. This is solely related to the dilution brought by the Argon injection. When Argon is injected, the mass fractions of every species will decrease unless reactions occur.

NO_2 production, as observed above, depends on both temperature and residence time (*Figure 5.2.22*). For Case 4, NO_2 is produced in the free-stream with minimal effects from the boundary layers. The difference in NO_2 changes between Case 3 and Case 4 comes from the residence time effect from the boundary layer. When there is mass addition, as in Case 1 and Case 2, a smaller increase in NO_2 is found compared to Case 4. The higher production due to the residence time effect in the top boundary layer is cancelled out by zero production from the bottom boundary layer plus dilution effects from mass addition. Comparing the injection cases (Case 1 and Case 2), injection of Argon leads to a slightly higher increase in NO_2. In general, however, the dilution effect due to mass addition is more significant than any additional chemical effects of added O_2 and N_2 on the evolution of NO_2.

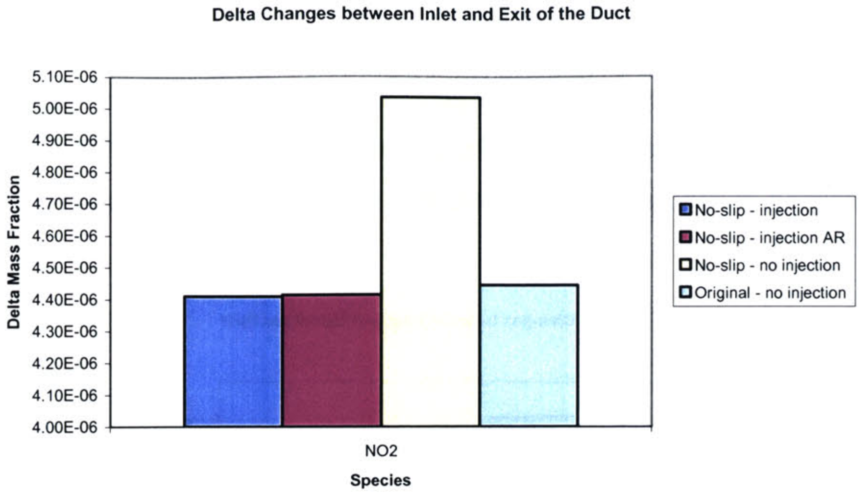

Figure 5.2.22. NO_2 changes between inlet and exit of the duct

The next species considered are HONO and SO_3 (*Figure 5.2.23)*. For HONO, slightly higher production is observed when air is injected for the mass addition cases. This agrees with our initial expectations that the addition of air leads to higher of N and O thus perturbing the radical pool and leading to higher production of trace species. However, the chemical effect is still much smaller than the dilution effect from mass addition. Both injection cases show lower HONO production than the no injection cases (Case 3, 4). As described above, temperature is the biggest driver for HONO production and the region of major production is a thin layer right above the cooled surface. Although Case 3 and Case 4 resolve that region slightly differently (thicker layer for Case 3, higher maximum production for Case 4), both of them end up with a similar amount of HONO production. The total production in the boundary layer is larger than the continual decrease of HONO in the free-stream.

For SO_3, maximum production is observed in Case 3 when there is no injection with the modified code. The difference in production between Case 3 and Case 4 is again due to Case 4's inability to capture the residence time effect in the upper boundary layer. For the injection cases, the levels are much lower than the no injection cases because only the upper boundary layer remains as a the major production zone for SO_3. The addition of mass greatly dilutes the existing level SO_3 such that the final production is smaller than the other two cases. Note that the behavior of SO_3 is similar to NO_2 but the production of NO_2 with mass addition remains close to the cases without mass addition. The major reason is that a relatively larger portion of NO_2 is produced in the free-stream. Although the residence time effects and temperature effects from the boundary layer further enhance the production, its dependence on those effects is not as big as for SO_3. Therefore, for SO_3, a large difference in production level is observed when one of the boundary layers is being disrupted by mass addition. When looking at the chemical effects due to mass addition, injection of air slightly enhances SO_3 production compared to injection of Argon. The dilution effect remains to be the major factor.

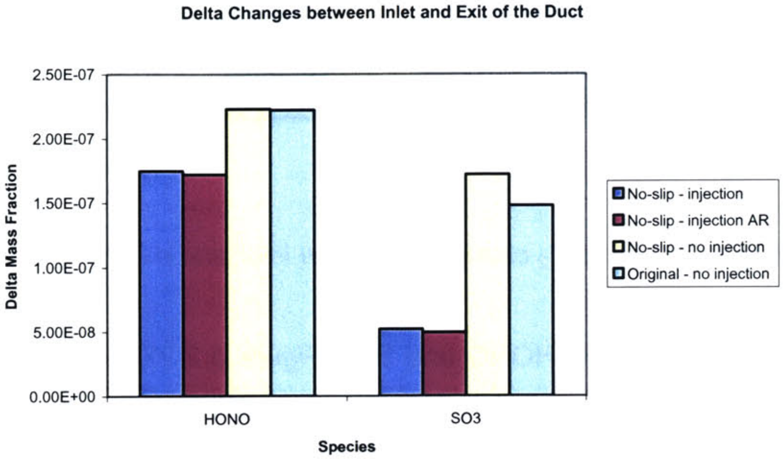

Figure 5.2.23. SO_3 and HONO changes between inlet and exit of the duct

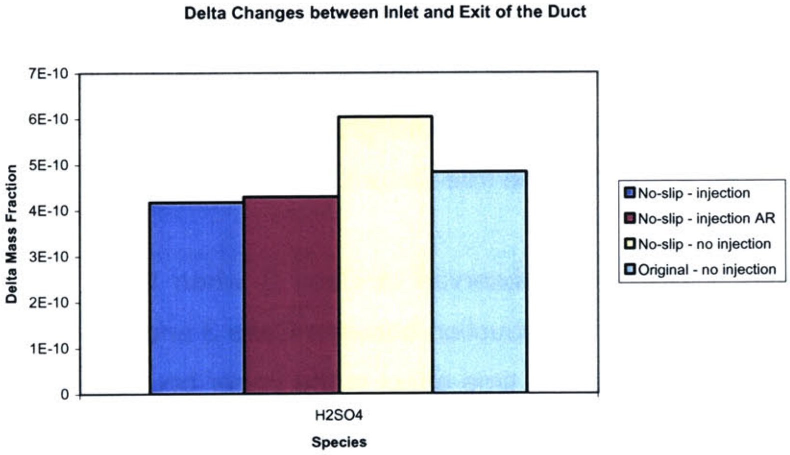

Figure 5.2.24. H_2SO_4 changes between inlet and exit of the duct

The last species considered is H_2SO_4 (*Figure 5.2.24*). As observed before, its behavior is similar to HONO with temperature being the biggest driver for H_2SO_4 production. Case 3 is the case with the largest amount of H_2SO_4 production. The level of Case 4 is slightly lower because of the thinner production layer resolved in the calculation. The levels of Case 1 and 2 are much less since a production zone remains at the boundary between the injection mass and the free-stream flow, though the production level in the region is lower than the case without any mass addition. The dilution effect further decreases the amount of H_2SO_4 being produced. As observed before, injection of air leads to a slightly lower production compared to Argon injection. Further investigations have to be carried out to determine the cause for the observation.

In general, having mass addition leads to changes in species evolution with the major impact being associated with mass dilution. Instead of having even higher production (comparing to no injection cases) for the trace species, mass addition leads to lower production. This is mainly because of the dilution of the higher production zones in the boundary layer. Note that if the investigation is run at a free-stream temperature above 1800 K, oxygen from air injection will start to dissociate to produce more reactive atomic oxygen. That may increase the productions of trace species significantly and overall chemical effects will become more important.

VI. Summary and Future Work

In this thesis, results of two tasks have been presented: 1. Assessment of the current modeling methodology for trace species evolution in the post-combustor flow path of gas turbine engines, and 2. Effects of mass addition on trace species evolution. The first task was carried out because the collaborative effort between NASA and QinetiQ to measure engine emissions provided a valuable opportunity to assess the accuracy of the model. The model utilizes 3-D CFD calculations for the first high pressure stage of the engine and 1-D kinetics calculations from first high pressure turbine exit to engine nozzle exit. Local non-uniformities and unsteadiness behavior in the turbine stage, where the trace species are more reactive, are captured with the high-fidelity CFD. Fast 1-D calculations applied to the relatively more mixed-out and less reactive flow keep the total computational time reasonable without trading off too much of accuracy.

Species evolution from the combustor exit to the nozzle exit of the QinetiQ TRACE engine was simulated using the operating conditions provided from the measurements. Special attention was given to temperature, pressure, SO_3, H_2SO_4, NO_2, and HONO. Temperature and pressure are important drivers for species evolution. SO_3, H_2SO_4, NO_2, and HONO have various impacts on the atmosphere leading to global warming. Modeling results showed agreement with engine measurements to within an order of magnitude. Discrepancies present are mainly because of insufficient data available to fully specify an accurate initial condition for the model calculations. Limited measurement points also limited the extent of comparisons.

The second task was carried out because the cooling effects were previously simulated by setting a desired wall temperature. However, in typical turbine blade cooling situations, mass is injected from the surface. Investigations were carried out to modify the CFD code. Wall functions in the code were removed and no-slip assumption was utilized to develop the mass addition capability. Mass addition was done in the fashion of transpiration cooling by setting blowing ratio, injection angles, and injection temperature. Studies on the impact of mass addition on trace species evolution were carried out on a simple square duct geometry. The effects of dilution were shown to dominate over any additional chemical effects associated with mass addition when the free-stream temperature is ~ 1150 K. Chemical effects may become more important when the free-stream temperature is higher than 1800 K as oxygen will start to dissociate to provide more highly reactive atomic oxygen. Dilution from mass addition led to smaller production of trace species compared to no injection cases with identical run conditions.

In order to integrate the mass addition capability into the existing engine emissions modeling methodology, mass addition will need to be simulated on surfaces of turbine blades. Preliminary tests have been carried out and problems were encountered. When the modified code without any injection was applied to a single blade NGV geometry with the same grid density as in the case for NASA/QinetiQ simulations (Chapter II), serious flow separation was observed on the suction side of the blade (*Figure 6.1.1*).

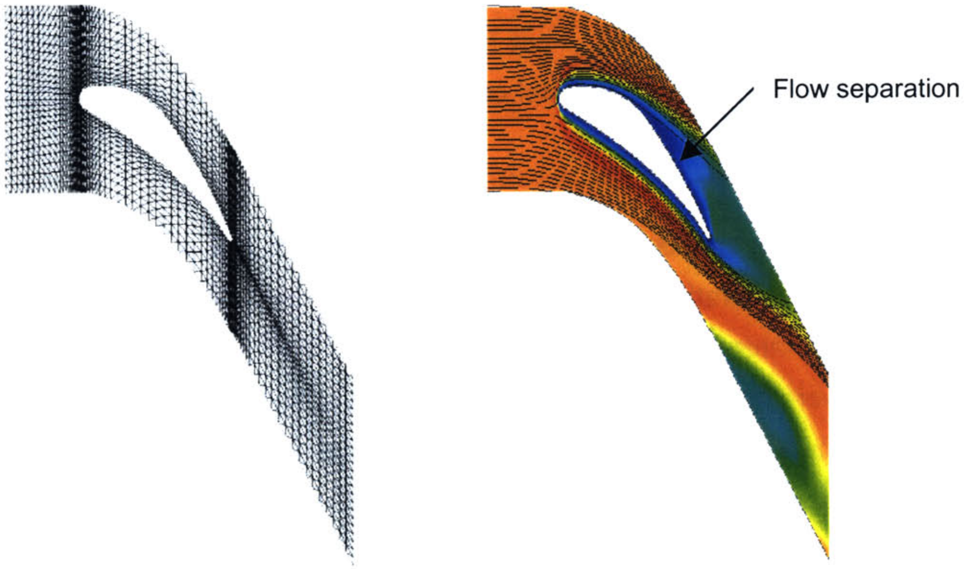

Figure 6.1.1. Calculation on NGV with original grid density using the modified code without injection, grid shown (left), static temperature with streamlines (right)

The grid shown in *Figure 6.1.1 contains* 21360 cells and required around 0.5 days for the flow-only calculation to converge. The cause of the separation is suspected to be related to the grid's inability to resolve the boundary layer on the blade surface since the no-slip condition instead of the more robust wall function was utilized. Previous investigations using the duct geometry also revealed that the modified code is much more sensitive to the grid and higher grid density is required to obtain accurate results. Thus, the grid was modified to increase the number of cells 4-fold to 95414 cells with cells clustered around the blade surface (*Figure*

6.1.2). The flow-only calculation took ~ 2-3 days to converge with much improved results. However, a small amount of separation still occurs on the suction surface (Figure 6.1.2).

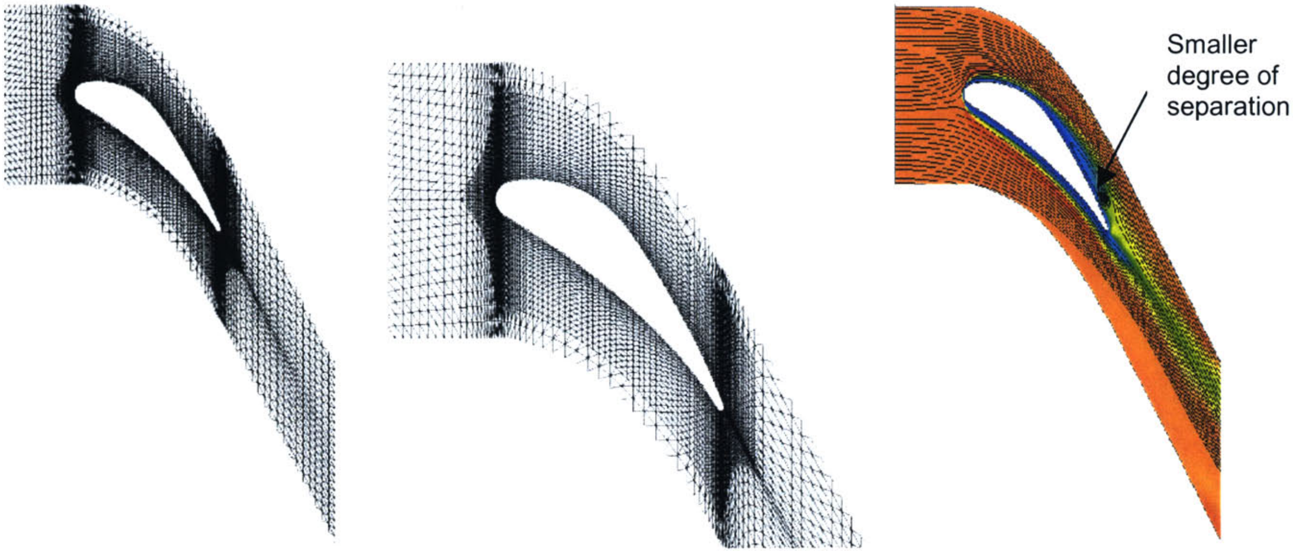

Figure 6.1.2. Calculation on NGV with increased grid density using the modified code without injection, grid shown (left), grid enlarged (center), static temperature with streamlines (right)

Increasing density of the grid seems to be the solution to the problem. The above grid was further refined in attempt to resolve the flow separation problem completely. The calculation using the further-refined grid took ~ 1 week for the flow-only calculation to complete (versus 0.5 day in the original density) and yielded unreasonable results. The cause of the problem is believed to be related to "over-clustering" of cells in certain locations when the grid is refined. Several different attempts at modifying the grid have been carried out but without success. One major obstacle is related to the grid refinement tool POST associated with CNEWT. The limited and inflexible options offered make grid refinements at specific locations difficult.

Further research and testing would be required to modify the grid until no separation occurs. Investigation must also be carried out to minimize the computational time while increasing the grid density. Note that in the model, a NGV grid with 3 blades is used to investigate the effect of inlet non-uniformity. That would increase the above computational time by a factor of three. Inclusion of chemistry into the calculation will further increase the computational time. A calculation using the 3-blade NGV grid with chemistry will take approximately 10 times the computational time mentioned above, i.e. 0.5 day for the original density grid would become ~5 days. This will significantly increase the turnaround time of the model.

With both the above problems resolved, mass addition should be enabled to test the capability on curved surfaces and to investigate the impact on trace species evolution in a turbine flow environment.

Appendix A – Additional Plots with NASA/QinetiQ Validation

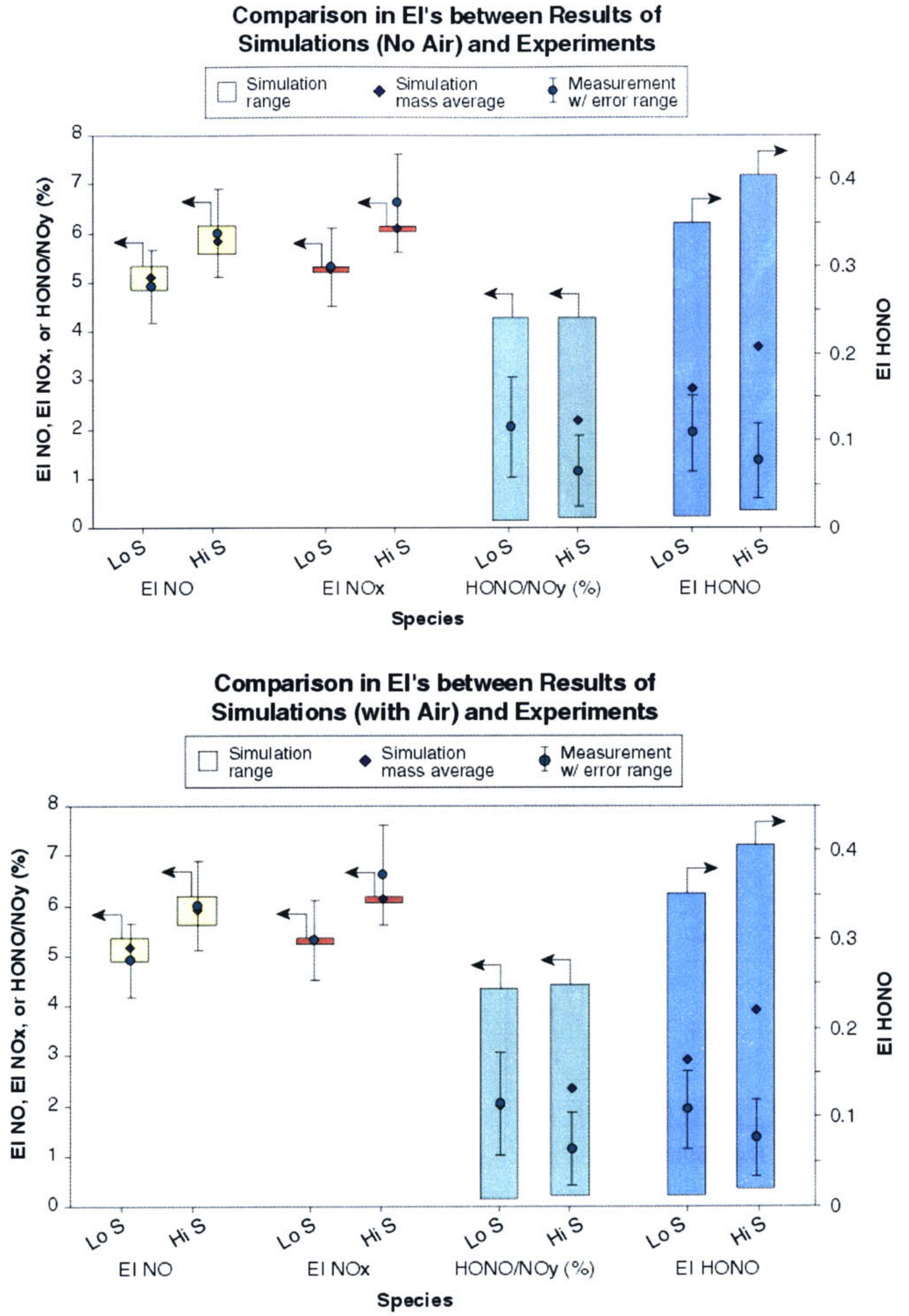

Figure A.1. Comparisons between results of simulations and experiments, no air dilution (top), with air dilution (bottom)

Note: Error bars with 2-sigma (standard deviation) are shown for HONO measurements

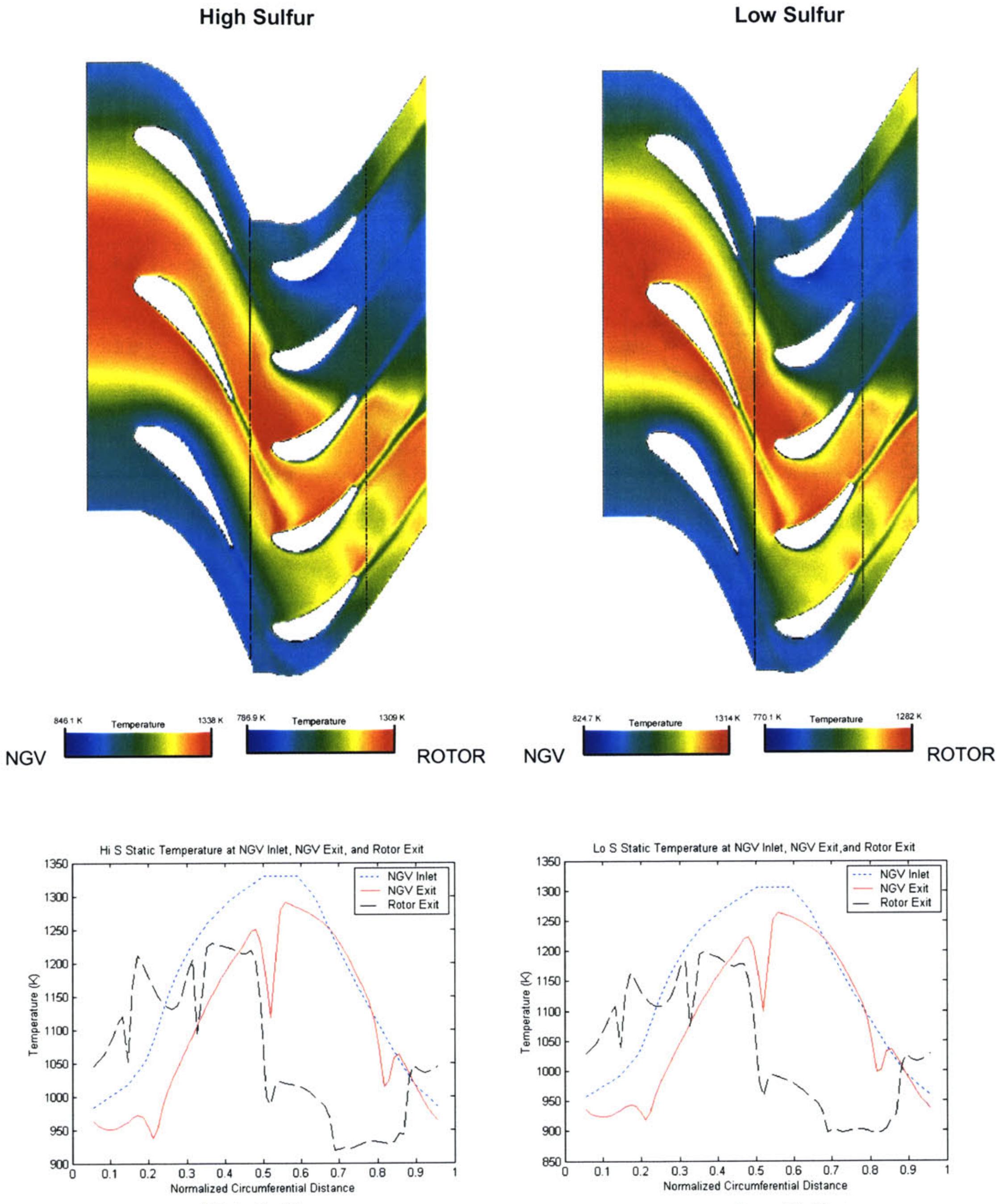

Figure A.2. Static temperature profiles for high sulfur (left) and low sulfur (right) runs

(Color range is different for NGV and rotor—refer to legends and plots for details.)

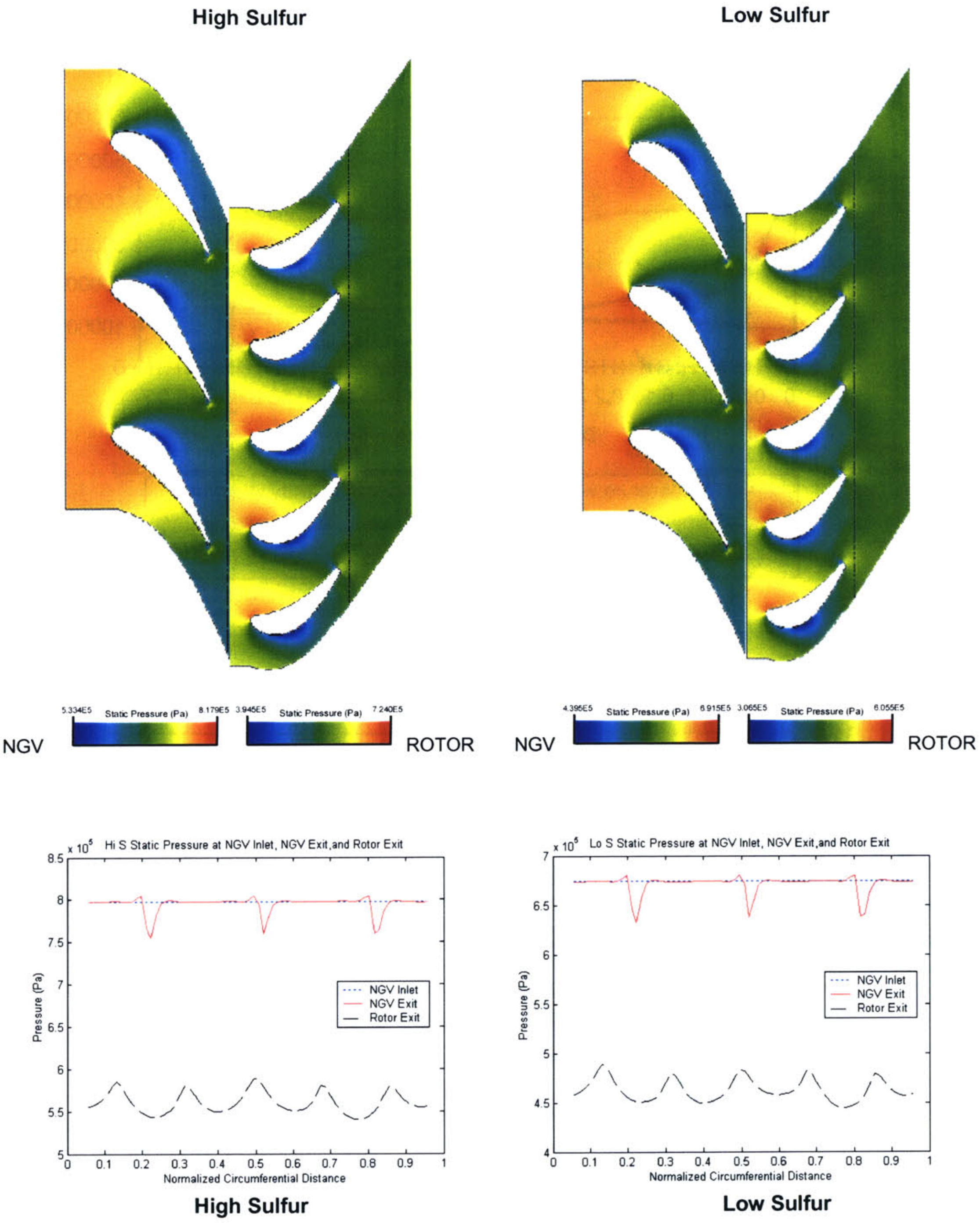

Figure A.3. Static pressure profiles for high sulfur (left) and low sulfur (right) runs

(Color range is different for NGV and rotor—refer to legends and plots for details.)

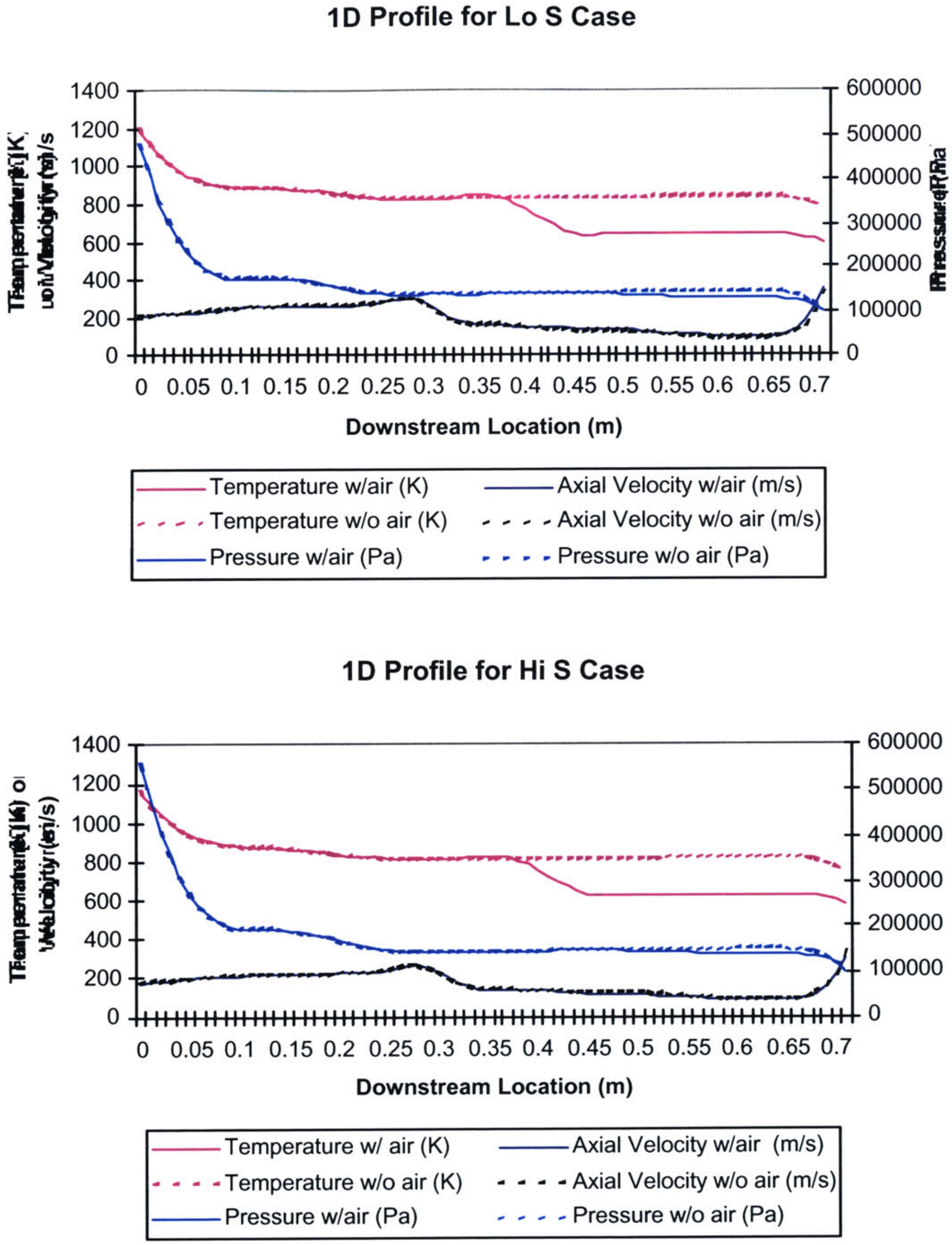

Figure A.4. Average 1-D temperature, pressure, and velocity profiles through second stage HPT, LPT, and exhaust nozzle, low Sulfur case (top), high sulfur case (bottom)

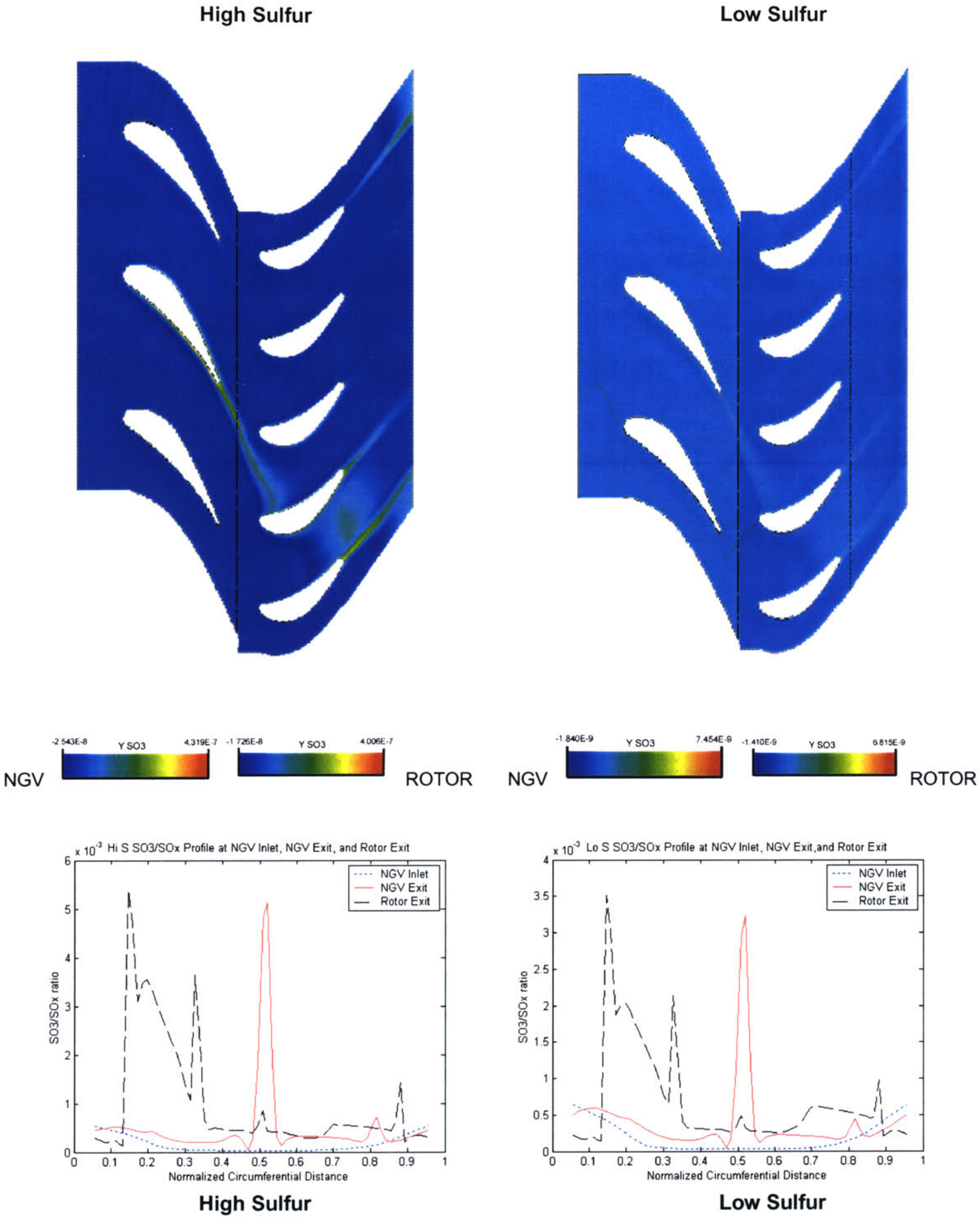

Figure A.5. SO_3 profiles for high sulfur (left) and low sulfur (right) runs

(Color range is different for NGV and rotor—refer to legends and plots for details.)

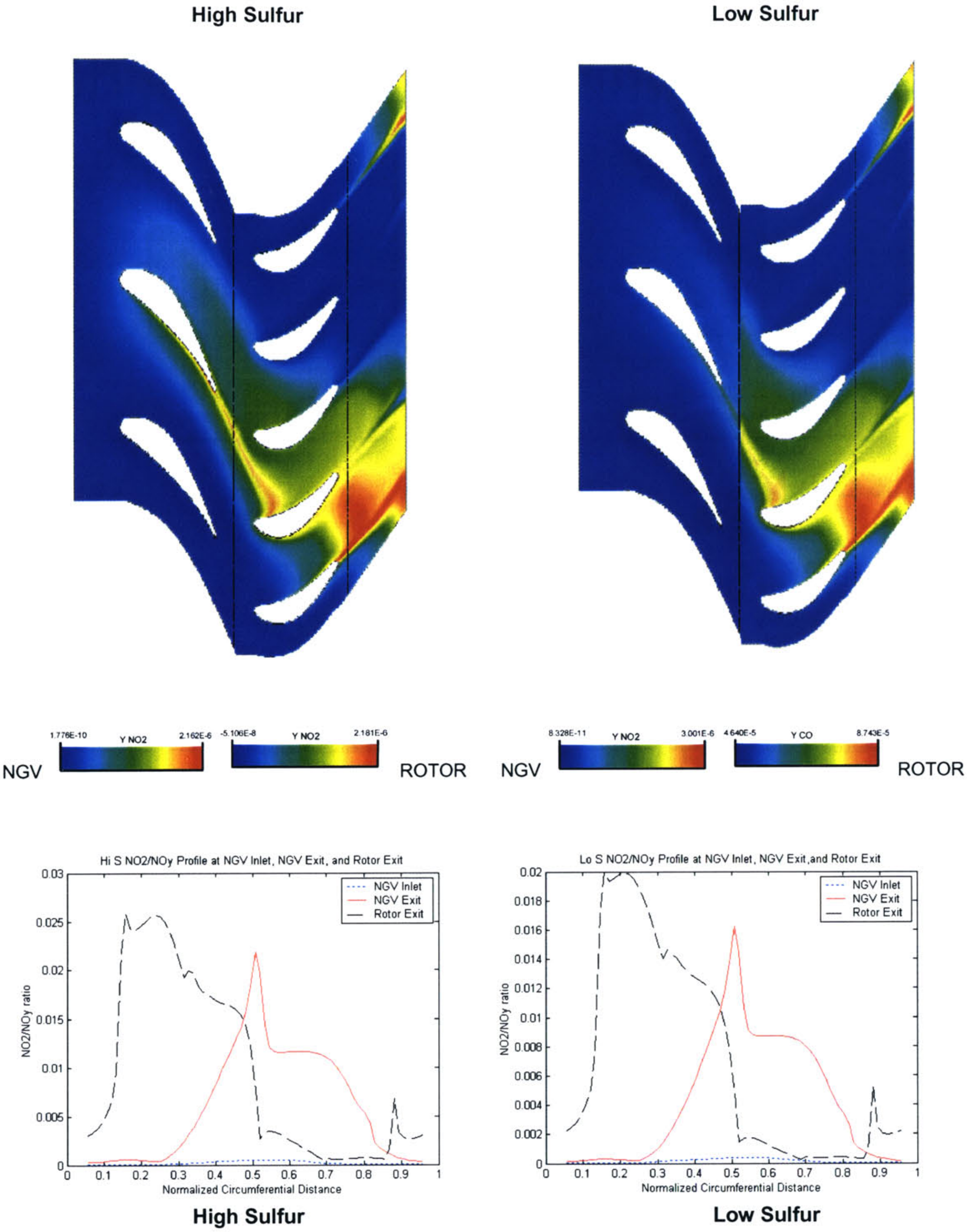

Figure A.6. NO_2 profiles for high sulfur (left) and low sulfur (right) runs

(Color range is different for NGV and rotor—refer to legends and plots for details.)

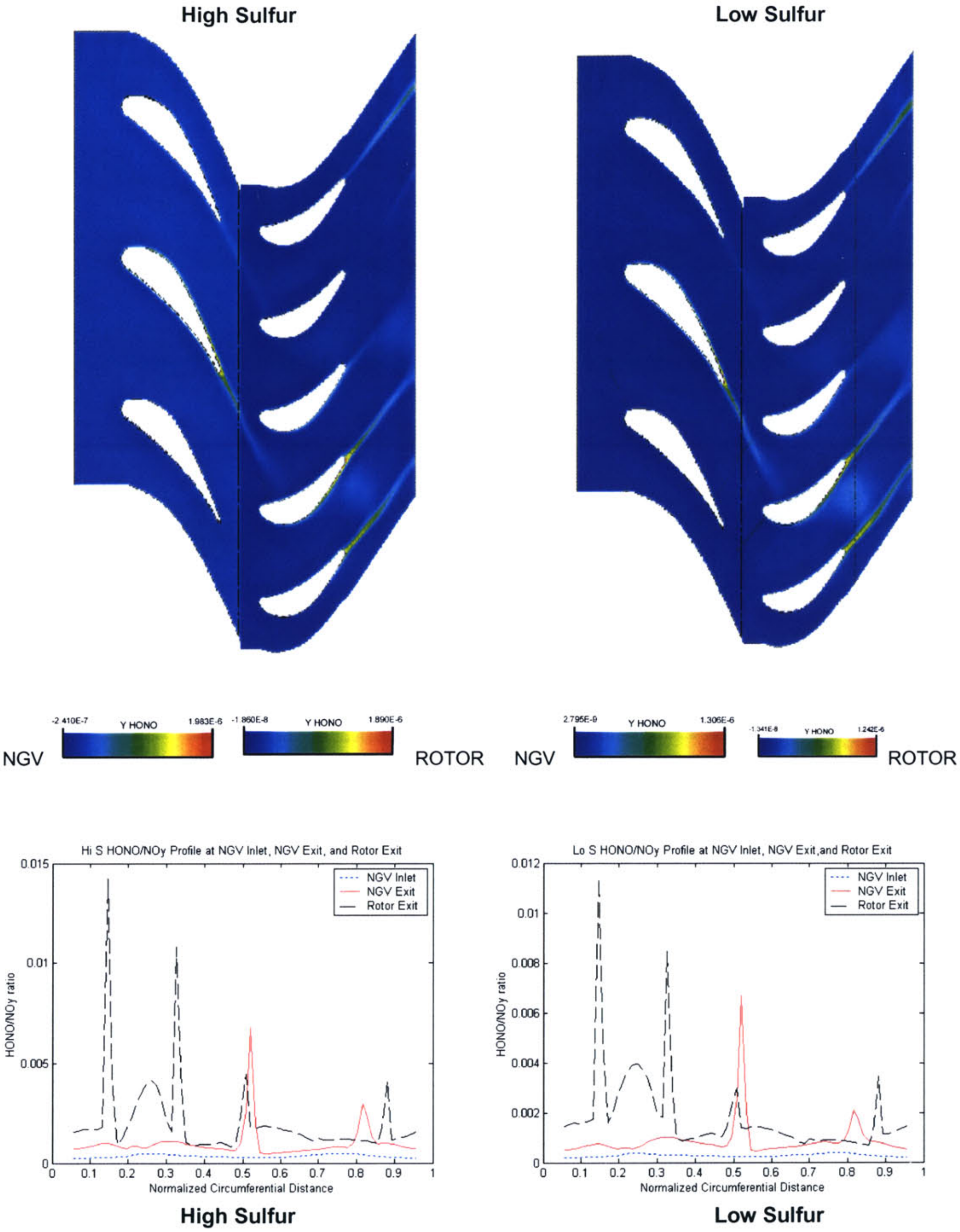

Figure A.7. HONO profiles for high sulfur (left) and low sulfur (right) runs

(Color range is different for NGV and rotor—refer to legends and plots for details.)

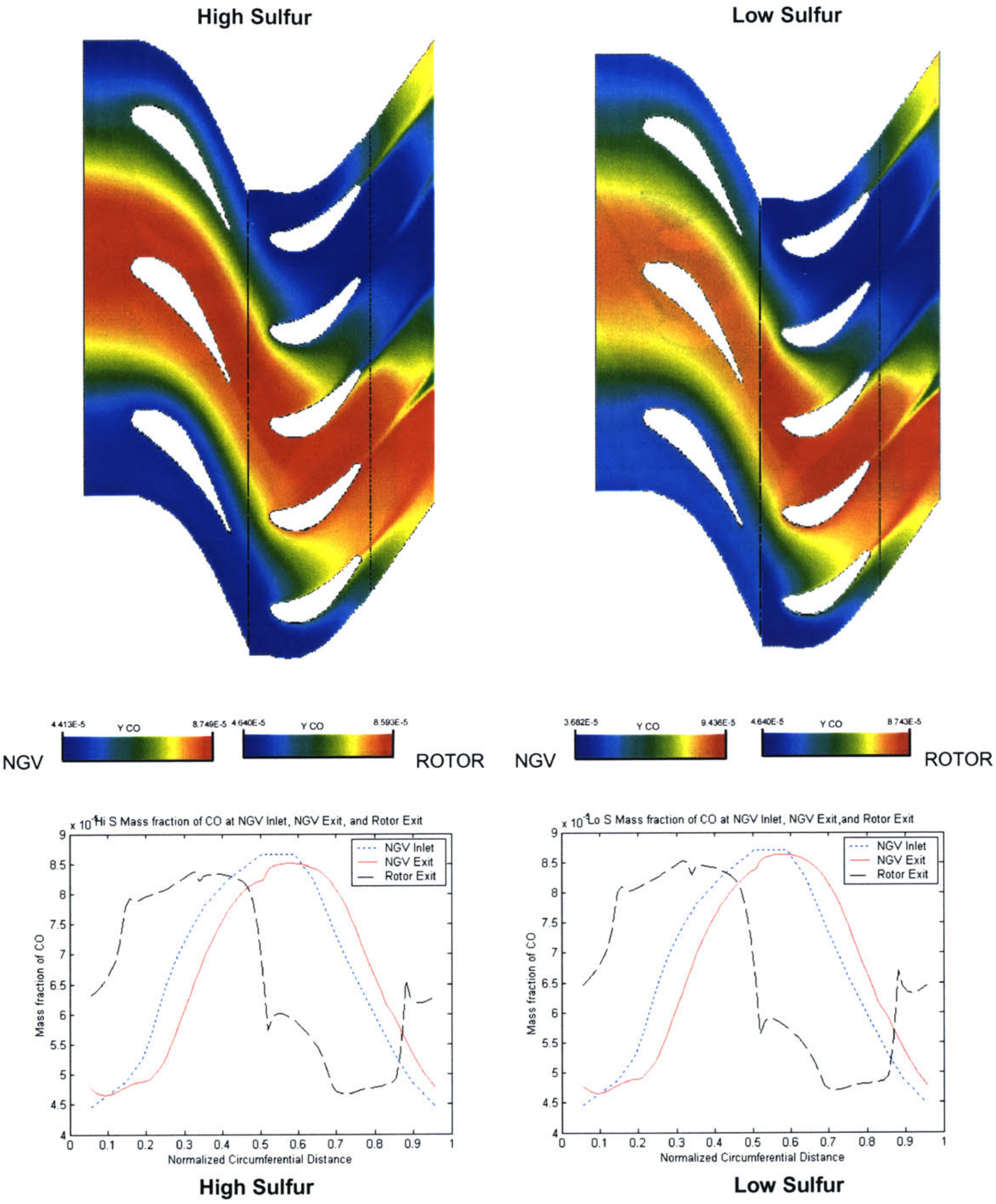

Figure A.8. CO profiles for high sulfur (left) and low sulfur (right) runs

(Color range is different for NGV and rotor—refer to legends and plots for details.)

Tabulated Simulation Results

		Combustor Exit		HPT1 NGV Exit		HPT1 Rotor Exit	
		Initial Condition		3-D CFD		3-D CFD	
		Low Sulfur	High Sulfur	Low Sulfur	High Sulfur	Low Sulfur	High Sulfur
SOx	SO3	0.00917ppbv	1.623ppbv	0.01972ppbv	5.381ppbv	0.03601ppbv	11.251ppbv
	H2SO4	0.000011ppbv	0.00193ppbv	0.000016ppbv	0.00350ppbv	0.000027ppbv	0.00676ppbv
	SO3/SOx	0.0155%	0.0134%	0.0319%	0.0423%	0.0578%	0.0880%
	H2SO4/SOx	1.90E-05%	1.58E-05%	2.65E-05%	2.75E-05%	4.40E-05%	5.28E-05%
NOy	NO2	4.921ppbv	7.212ppbv	170.37ppbv	273.88ppbv	279.49ppbv	432.68ppbv
	HONO	8.297ppbv	12.230ppbv	29.632ppbv	37.787ppbv	62.880ppbv	78.414ppbv
	NO2/NOy	0.0100%	0.0128%	0.3319%	0.4630%	0.5407%	0.7268%
	HONO/NOy	0.0169%	0.0216%	0.0577%	0.0639%	0.1216%	0.1317%
CO	CO	65.41ppmv	65.37ppmv	67.92ppmv	67.54ppmv	68.11ppmv	67.54ppmv
	CO/COx	0.332%	0.332%	0.330%	0.328%	0.329%	0.326%
HOx	H	0.832ppbv	1.069ppbv	1.216ppbv	1.383ppbv	1.280ppbv	1.451ppbv
	O	25.255ppbv	35.332ppbv	47.710ppbv	60.158ppbv	57.487ppbv	72.851ppbv
	OH	1.79ppmv	2.29ppmv	2.34ppmv	3.02ppmv	2.28ppmv	2.98ppmv
	HO2	35.416ppbv	43.879ppbv	109.050ppbv	124.406ppbv	115.499ppbv	128.056ppbv

		Nozzle Exit (no air addition)					
		1-D Kinetics					
		Low Sulfur	Min	Max	**High Sulfur**	Min	Max
SOx	SO3	0.340ppbv	0.045ppbv	1.210ppbv	68.137ppbv	10.577ppbv	229.008ppbv
	H2SO4	0.00549ppbv	0.00117ppbv	0.02077ppbv	0.72359ppbv	0.14527ppbv	2.77290ppbv
	SO3/SOx	0.5420%	0.1003%	1.5778%	0.5192%	0.1157%	1.4745%
	H2SO4/SOx	0.0088%	0.0016%	0.0352%	0.0055%	0.0009%	0.0240%
NOy	NO2	1081.28ppbv	25.17ppbv	2986.41ppbv	1621.92ppbv	51.63ppbv	3860.71ppbv
	HONO	987.08ppbv	52.99ppbv	2718.96ppbv	1309.70ppbv	85.51ppbv	3155.06ppbv
	NO2/NOy	2.0790%	0.0682%	4.5180%	2.6552%	0.1216%	5.0746%
	HONO/NOy	1.8979%	0.1435%	4.1802%	2.1441%	0.2014%	4.1846%
CO	CO	67.76ppmv	49.21ppmv	84.01ppmv	68.02ppmv	49.05ppmv	81.75ppmv
	CO/COx	0.325%	0.312%	0.333%	0.320%	0.306%	0.333%
HOx	H	0.188ppbv	0.001ppbv	0.729ppbv	0.270ppbv	0.001ppbv	1.039ppbv
	O	19.550ppbv	0.130ppbv	81.179ppbv	20.963ppbv	0.156ppbv	81.235ppbv
	OH	0.26ppmv	0.00ppmv	0.93ppmv	0.35ppmv	0.00ppmv	1.27ppmv
	HO2	21.486ppbv	0.280ppbv	74.500ppbv	27.003ppbv	0.509ppbv	90.247ppbv

		Nozzle Exit (w/air addition)					
		1-D Kinetics					
		Low Sulfur	Min	Max	**High Sulfur**	Min	Max
SOx	SO3	0.226ppbv	0.013ppbv	0.572ppbv	53.399ppbv	3.050ppbv	124.392ppbv
	H2SO4	0.05885ppbv	0.01340ppbv	0.29786ppbv	9.69225ppbv	3.02890ppbv	46.27696ppbv
	SO3/SOx	0.6716%	0.0538%	1.3847%	0.7510%	0.0613%	1.4755%
	H2SO4/SOx	0.1752%	0.0560%	0.7196%	0.1363%	0.0561%	0.5462%
NOy	NO2	533.64ppbv	12.94ppbv	1488.87ppbv	845.22ppbv	27.32ppbv	2029.47ppbv
	HONO	539.76ppbv	28.27ppbv	1497.03ppbv	749.79ppbv	46.65ppbv	1786.37ppbv
	NO2/NOy	1.9142%	0.0651%	4.1488%	2.5537%	0.1183%	4.8765%
	HONO/NOy	1.9361%	0.1423%	4.2078%	2.2654%	0.2020%	4.2924%
CO	CO	36.36ppmv	26.48ppmv	45.45ppmv	36.90ppmv	26.68ppmv	44.69ppmv
	CO/COx	0.325%	0.313%	0.333%	0.321%	0.307%	0.333%
HOx	H	0.026ppbv	0.000ppbv	0.107ppbv	0.031ppbv	0.000ppbv	0.127ppbv
	O	18.746ppbv	0.075ppbv	74.418ppbv	19.434ppbv	0.082ppbv	74.853ppbv
	OH	0.14ppmv	0.00ppmv	0.50ppmv	0.15ppmv	0.00ppmv	0.56ppmv
	HO2	9.276ppbv	0.136ppbv	33.362ppbv	15.509ppbv	0.277ppbv	52.958ppbv

Table A.1. Complete results obtained for NASA/QinetiQ simulations

Appendix B – Effects of Wall Function on Transpiration Surface

As mentioned in section 4.3, it is necessary to determine the effects of wall function on transpiration surface in order to modify the boundary condition implementations in the code. In the wall function, the velocity deficit on the wall is obtained by including a sink term, related to the approximated wall shear stress, in the momentum equation (Eq. 4.1.4). However, this method doesn't enforce the no-slip condition on the wall surface, i.e. some slip velocity exists. When there is mass addition, the amount of mass and the momentum being injected will be determined by the injection velocities and their corresponding angles. This can be implemented by setting the desired velocities on the boundary nodes of the injection surface. The following problem then arises: what will happen to the wall function, or the boundary layer being resolved, when the boundary nodes are forced to certain values?

Investigations have been carried out to keep the wall function in the code while enforcing a no-slip condition on injection surface to resemble the effect when the mass added is zero. Two problems arise in the calculations:

1. Discontinuity between the injection and non-injection surfaces: On the non-injection surface, a wall function is utilized and a finite slip velocity is obtained on the surface (Case 2 in *Figure B.1*). At the same time, on the injection surface, no-slip condition is enforced despite the presence of a wall function such that zero velocity is obtained on the surface (Case 1 in *Figure B.1*). At the junction where these two surfaces meet, discontinuities in velocities between the two surfaces arise.

2. Discontinuity on the injection surface and slightly above the injection surface: Right on the injection surface, a no-slip condition is enforced. However, due to the presence of the wall function, it tries to approximate the boundary layer at the same time. The above two methods do not match with each other. This results in discontinuities in velocities right on the injection surface and slightly above the injection surface (Case 3 in *Figure B.1*).

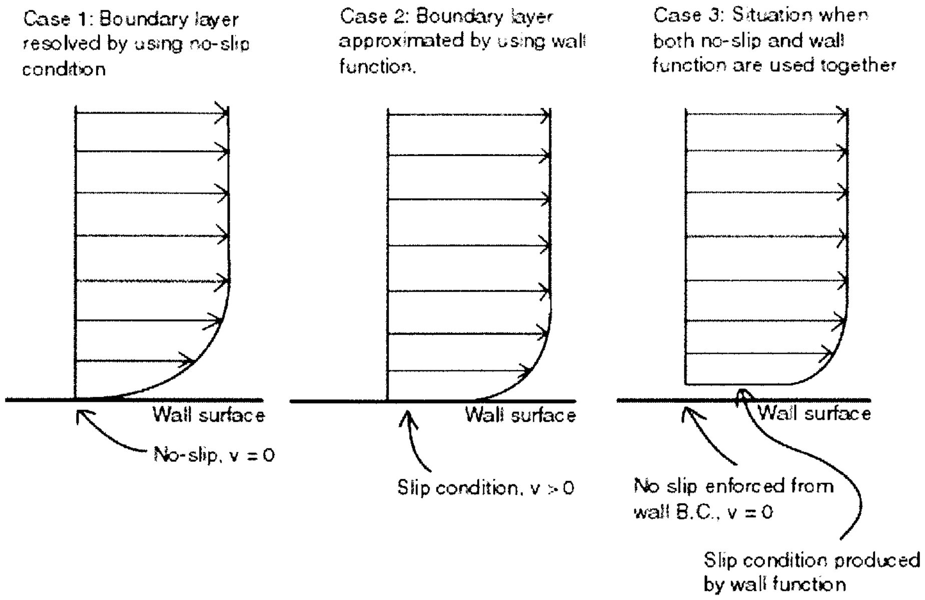
Case 1: Boundary layer resolved by using no-slip condition
Case 2: Boundary layer approximated by using wall function.
Case 3: Situation when both no-slip and wall function are used together
Wall surface
No-slip, v = 0
Wall surface
Slip condition, v > 0
Wall surface
No slip enforced from wall B.C., v = 0
Slip condition produced by wall function

Figure B.1. Various situations in resolving the boundary layer

The above two problems create problems and non-physical results in the calculations. Therefore, it can be concluded that both methods in resolving the boundary layer on the wall surface cannot be applied at the same time. To resolve this issue, one could either modify the wall function to accommodate the presence of mass injection, or remove the wall function completely. To modify the wall function, it is first necessary to fully understand how the existing wall function approximates the wall shear stress. Then, it is necessary to investigate how the presence of mass addition through transpiration will affect the wall function. Note that the boundary layer profile will be modified with the presence of extra mass, as will the momentum on the wall due to mass addition. Thus the typical way of approximating the shear stresses for the boundary layer may no longer be applicable. This is also true for the turbulence model since the associated wall function is also applied on the wall. As a result, modifying the wall function was determined to be a relatively difficult task due to limited documentation and explanations on the usage and limitations of the wall functions utilized in the code.

References

1. Penner, J.E., D.H. Lister, D.J. Griggs, D.J. Dokken, M. McFarland, *Aviation and the Global Atmosphere*, Cambridge University Press, 1999.

2. Lukachko, S.P., *Research on the Science and Politics of the Atmospheric Effects of Aviation Debate*, S.M. Thesis, Massachusetts Institute of Technology, 1997.

3. Chobot III, A.T., *Modeling the Evolution of Trace Species in the Post-combustor Flow Path of Gas Turbine Engines*, S.M. Thesis, Massachusetts Institute of Technology, 2000.

4. Han, S., *Reduced-order Modeling for Trace Species in the Post-combustion Flow Path and Effects of Technology Trends on Emissions*, S.M. Thesis, Massachusetts Institute of Technology, 2003.

5. Mueller, M.A., R.A. Yetter, F.L. Dryer, *Kinetic Modeling of the $CO/H_2O/O_2/NO/SO_2$ system: Implication for High-Pressure Fall-off in the $SO_2+O\ (+M) = SO_3\ (+M)$ Reaction*, International Journal of Chemical Kinetics, 32, January 2000: pp. 317 – 339.

6. Dawes, W.N., *A Computer Program for Analysis of Three Dimensional Viscous Compressible Flow in Turbomachinery Blade Rows*, Whittle Laboratory, Cambridge, U.K., 199x.

7. Dawes, W.N., *The Practical Application of Solution-Adaption to the Numerical Simulation of Complex Turbomachinery Problems*, Progress in Aerospace Sciences, 29, 1992: pp. 221 – 269.

8. Brundish, K., *QinetiQ/NASA Collaborative Programme – Final Report*, QinetiQ, U.K., 2002.

9. Clague, A., M. Whiteman, *Internal Project Memorandum*, DERA and MIT/ARI proprietary, 1998-2000.

10. Kerrebrock, J.L., *Aircraft Engines and Gas Turbines*, MIT Press, Cambridge, Massachusetts, 1996.

11. Hill, P.G., C.R. Peterson, *Mechanics and Thermodynamics of Propulsion*, Addison-Wesley, 1992.

12. Brundish, K., *DERA/NASA Interim Report – Combustor Testing Data Report*, QinetiQ, U.K., 2001.

13. Lienhard, J.H. IV, J.H. Lienhard V., *A Heat Transfer Textbook*, Phlogiston Press, Cambridge, Massahusetts, 2001.

14. Dawes, W.N., *Application of Full Navier-Stokes Solvers to Turbomachinery Flow Problems*, Von Karman Inst. for Fluid Dynamics Numerical Techniques for Viscous Flow Calculations in Turbomachinery Bladings, 1986.

15. Launder, B.E., D.B. Spalding, *The Numerical Computation of Turbulent Flows*, Computer Methods in Applied Mechanics and Engineering, 3, 1974: pp. 269 – 289.

16. Lam, C.K.G., K. Bremhorst, *A Modified Form of the* κ-ε *Model for Predicting Wall Turbulence*, Journal of Fluids Engineering, 103, 1981: pp. 456 – 460.

17. Rolls-Royce, *The Jet Engine*, Rolls-Royce plc, Derby, U.K., 1992.

18. Cebeci, T., J. Cousteix, *Modeling and Computation of Boundary-Layer Flows*, Horizons Publishing Inc., Long Beach, California, 1999.

19. Royal Commission on Environmental Pollution, *The Environmental Effects of Civil Aircraft in Flight*, U.K., 2002.

5000
39